The Influence Of Albedo And Cooling On The Yield of Floating PV Systems

by

Shahina Salim Patel

Thesis presented in partial fulfilment of the requirements for the degree of Master of Engineering (Electrical) in the Faculty of Engineering at Stellenbosch University

Supervisor: Dr. Arnold J. Rix

March 2021

Declaration

By submitting this thesis electronically, I declare that the entirety of the work contained therein is my own, original work, that I am the sole author thereof (save to the extent explicitly otherwise stated), that reproduction and publication thereof by Stellenbosch University will not infringe any third party rights and that I have not previously in its entirety or in part submitted it for obtaining any qualification.

Date: 2021/01/08 .....

Abstract

The Influence Of Albedo And Cooling On The Yield of Floating PV Systems

S.S. Patel

Department of Electrical and Electronic Engineering,
University of Stellenbosch,
Private Bag X1, Matieland 7602, South Africa.

Thesis: MEng (Elec)

March 2021

Floating PV (FPV) technology is an innovative technique of deploying PV modules on water bodies. Floating solar PV plants conserve the land areas and operate under lower temperatures, which lead to higher power outputs due to the cooling effect from the water. Due to the reflective and evaporative properties of the water surface, the performance of FPV systems is affected by the water surface reflectance and the heat transfer between the PV modules and the atmospheric environment.

In the absence of measured reflected radiation from water, a default albedo value of 0.2 is commonly used to simulate PV systems as varying water surface albedo is currently not integrated into the PV simulation software. Therefore, the research work provides the modelling of the time-varying water surface albedo with the change in solar elevation; as changes in weather patterns strongly affect the radiation received on the FPV modules and the reflection off the water surface. Results show that the water surface albedo is affected by the spectral and angular dependencies of the irradiance; and that the albedo is lower at higher solar elevations and higher at lower solar elevations.

Furthermore, this research studies Ocean Sun's FPV technology that uses the concept of using floating PV modules on a flexible polymer floating structure on the water surface. Performance analysis shows that the water-cooled string, which is in thermal contact with the floating canvas, performs between 3.17 % to 7.32 % better than the air-cooled string, which is lifted 32 mm above the floating canvas using 32 mm polypropylene pipes.

A thermal model is also being investigated to estimate the cooling effect of an air-cooled and a water-cooled FPV string in comparison to a ground-mounted PV string. Average U-values of 30 $W/m^2.K$ and 89 $W/m^2.K$ for the air-cooled and water-cooled string is observed, respectively. Higher U-values corresponds to a better cooling effect due to the direct thermal contact of the PV modules with the floating canvas on the water surface. An average U-value of 27 $W/m^2.K$ is observed from the ground-mounted PV system.

The research also tests the ability of solar PV simulation software, PVsyst, to successfully simulate FPV systems and to compare the energy yield of an FPV system with hypothetical tilted strings and increasing U-values in the same location. The influence of the tilted panels at different tilt angles on the energy yield of the FPV system using the default albedo versus the modelled albedo is analysed. PVsyst simulation shows that the energy production increases with an increase in U-values and the energy difference increases with an increase in the tilt angles due to the lower irradiance experienced at higher tilt angles.

Uittreksel

Die invloed van Albedo en verkoeling op die opbrengs van drywende PV-stelsels

("The Influence Of Albedo And Cooling On The Yield of Floating PV Systems")

S.S. Patel

Departement Elektries en Elektroniese Ingenieurswese,
Universiteit van Stellenbosch,
Privaatsak X1, Matieland 7602, Suid Afrika.

Tesis: MIng (Elek)

Maart 2021

Drywende PV (DPV) tegnologie is 'n innoverende tegniek om PV-modules op water in te span. Drywende sonkrag-PV-aanlegte bewaar die landgebiede en werk onder laer temperature, wat lei tot hoër kraglewering as gevolg van die verkoeling van die water. As gevolg van die reflekterende en verdampingseienskappe van die wateroppervlak, word die opbrengs van DPV-stelsels beïnvloed deur die wateroppervlakrefleksie en die hitte-oordrag tussen die PV-modules en die atmosferiese omgewing.

In die afwesigheid van gemete waardes vir die gereflekteerde straling van water word 'n standaard albedo-waarde van 0.2 gebruik om PV-stelsels te simuleer, aangesien wisselende wateroppervlak albedo tans nie in die PV-simulasiesagteware geïntegreer is nie. Die navorsing bied die modellering van die tydswisselende wateroppervlak albedo met die verandering in sonhoogte aan; aangesien veranderinge in weerpatrone die bestraling wat die DPV-modules ontvang grootliks beïnvloed, asook die weerkaatsing van die wateroppervlak af. Resultate toon dat die wateroppervlak albedo beïnvloed word deur die spektrale inhoud en hoek afhanklikheid van die bestraling; en dat die albedo laer is by hoër sonhoogtes, en hoër by laer sonhoogtes.

Verder bestudeer hierdie navorsing Ocean Sun se DPV-tegnologie wat die konsep gebruik om drywende PV-modules op 'n drywende buigsame polimeer struktuur te plaas om sodoende op die wateroppervlak te dryf. Opbrengsanalise toon dat die waterverkoelde string, wat termiese in kontak is met

die drywende doek, tussen 3.17% en 7.32% beter presteer as die lugverkoelde string, wat 32 mm bo die drywende doek gelig is met behulp van 32 mm polipropileenpype.

'n Termiese model word ook ondersoek om die verkoelingseffek van 'n lugverkoelde en 'n waterverkoelde DPV-string te skat in vergelyking met 'n grond gemonteerde PV string. Gemiddelde U-waardes van 30 $W/m^2.K$ en 89 $W/m^2.K$ vir die lugverkoelde en waterverkoelde stringe word onderskeidelik waargeneem. Hoër U-waardes stem ooreen met 'n beter verkoelingseffek as gevolg van die direkte termiese kontak van die PV-modules met die drywende doek op die wateroppervlak. 'n Gemiddelde U-waarde van 27 $W/m^2.K$ word waargeneem vir die grond gemonteerde PV-stelsel.

Die navorsing toets ook die vermoë van sonkrag-PV-simulasiesagteware, PVsyst, om DPV-stelsels suksesvol te simuleer en om die energie-opbrengs van 'n DPV-stelsel met hipotetiese gekantelde stringe en toenemende U-waardes op dieselfde plek te vergelyk. Die invloed van die gekantelde panele by verskillende kantelhoeke op die energie-opbrengs van die DPV-stelsel met die gebruik van die standaard albedo teenoor die gemodelleerde albedo word geanaliseer. Die PVsyst simulasie toon dat die energieopbrengs toeneem met 'n toename in U-waardes en dat die verskil in energie toeneem met 'n toename in die kantelhoeke as gevolg van die laer bestraling wat by hoër kantelhoeke ervaar word.

Acknowledgements

I would like to sincerely express my heartfelt appreciation to the following people and organisations:

- God Almighty for providing the strength and blessings to pursue this research with the best of my ability.
- Dr Arnold J. Rix, my supervisor at Stellenbosch University, for the academic feedback and guidance.
- Scatec Solar for funding my Master's studies.
- Grateful to my mom, my dad and my siblings for the constant motivation and emotional support.
- Ocean Sun and the Institute for Energy Technology (IFE) for providing me with the opportunity to embark on this project.
- Dr Josefine Helene Selj and Dr Torunn Kjeldstad, from IFE, for the great support and for giving me invaluable advice on the Ocean Sun's project.
- Sigmund Bragstad from Ocean Sun for the logistics of travelling to Skaftå, and for providing me with information about the system.

Dedications

This thesis is dedicated to my family.

Contents

List of Figures

List of Tables

Nomenclature

Abbreviations

PV	Photovoltaic
FPV	Floating Photovoltaic
RES	Renewable Energy Sources
UNFCCC	United Nations for Climate Change Conference
COP21	21st Conference of the Parties
IRENA	Renewable Energy Agency
DC	Direct Current
BOS	Balance of System
CAPEX	Capital Expenditure
LCOE	Levelized Cost of Electricity
T&C	Testing & Commissioning
SERIS	Solar Energy Research Institute of Singapore
UAE	United Arab Emirates
AM	Air Mass
DNI	Global Horizontal Irradiance
DNI	Direct Normal Irradiance
DHI	Diffuse Horizontal Irradiance
I-V	Current-Voltage
STC	Standard Test Condition
UV	Ultraviolet
IR	Infrared
SAURAN	Southern African Universities Radiometric Network
CRSES	Centre for Renewable and Sustainable Energy Studies
GSET	Group for Solar Energy Thermodynamics
CSV	Comma-separated values
MBE	Mean Bias Error
RMSE	Root MEan Square Error
AOD	Aerosel Optical Depth

STP	Standard Temperature and Pressure
MPPT	Maximum Power Point Tracker
RTD	Resistance Temperature Detector
LAN	Local Area Network
WLAN	Wireless Local Area Network
PR	Performance Ratio
NOCT	Nominal Operating Cell Temperature
IQR	Interquartile Range
SCADA	Supervisory Control And Data Acquisition
SSM	Sunny String-Monitor
AC	Alternating Current

Constants

h	Plank's constant ($6.62607004 \times 10^{-34}$ J.s)
k	Boltzmann's constant ($1.3806503 \times 10^{-23}$ J/K)
q	Electron charge ($1.60217646 \times 10^{-19}$ C)

Chapter 1

Introduction

1.1 Background

With the rapid growth of the world population and economic development, energy demands are rising constantly. In 2018, the global energy consumption has increased by 2.3 %, which is twice the average growth rate since 2010 [1]. To date, energy remains the most important concern of both the present and the future. Since the Industrial Revolution, fossil fuel energy from coal, natural gas and oil has and is continuing to dominate the global energy system to meet the worldwide energy consumption needs [2]. However, there is an increase in the depletion of fossil fuels which necessitates evolving to different techniques to fulfil the growing energy demands [3]. Coal-intensive energy generation continuously remains as the biggest driver of climate change issues, such as air pollution and the emission of CO_2 and other greenhouse gases which negatively impacts the environment [4]. Therefore, the need to maximize the penetration of Renewable Energy Sources (RES) is of importance.

In 2015, at COP21 in Paris, the Parties to the United Nations for Climate Change Conference (UNFCCC) agreed to unite all nations to combat climate change [5]. This agreement is commonly known as the "Paris Agreement" which is the new globally accepted climate change agreement. The Parties acknowledged the importance of accelerating investments and intensifying actions that provide a sustainable carbon future [5]. The aim of the Paris Agreement is to reinforce the global response towards climate change by constantly maintaining the global temperature rise below 2 C° in comparison to pre-industrial levels and to suppress climate change threats by pursuing the efforts to limit an increase in temperature with a further 1.5 C° [5]. Thus, to achieve the goals of the Paris Agreement, it is necessary to execute actions which balance the energy demands and minimize the usage of energy sources which accelerate the greenhouse effect globally, while continuously seeking alternative ways to decarbonize and reduce the reliance on fossil fuels. A hunt for establishing

improved technologies developed from the current renewable energy sources is important to meet the global climate objectives and to transition towards a lower-carbon economy [6], [7]. Therefore, the production of clean energy from renewable energy sources is rapidly increasing worldwide. Figure 1.1 shows the share of the different installed renewable energy sources at the end of 2019. Energy generation from hydropower is leading to other renewable energy sources, whilst solar energy contributing 22.04 % of the global installed capacity. The International Renewable Energy Agency (IRENA) reported a total installed renewable energy capacity of 2532.9 *GW* at the end of 2019 [8].

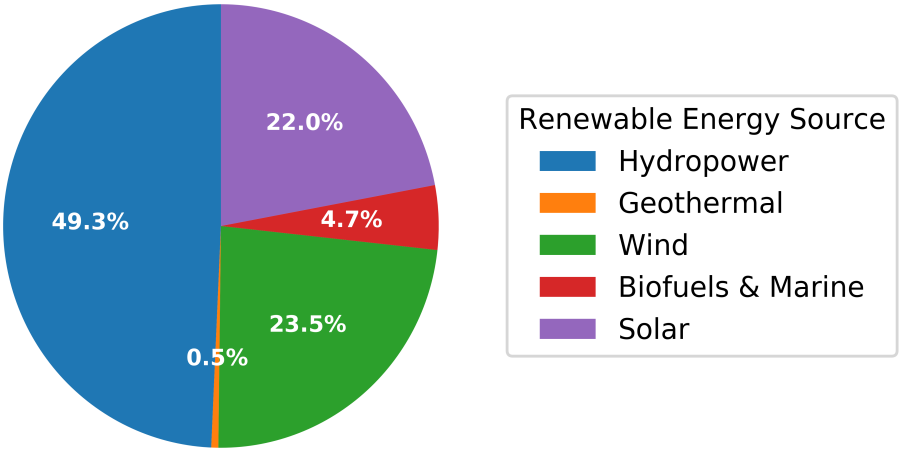

Figure 1.1: Percentage capacity distribution of the global renewable enrgy sources (data acquired from [8])

From all the different RESs, solar energy remains the most promising, cost-effective, eco-friendly and freely available energy alternative to conventional energy resources [9]. According to the International Renewable Energy Agency (IRENA), the global installed solar PV capacity has reached a whopping milestone of 578.6 *GW* at the end of 2019 as shown in Figure 1.2, growing 14 times it's capacity since 2010 [8].

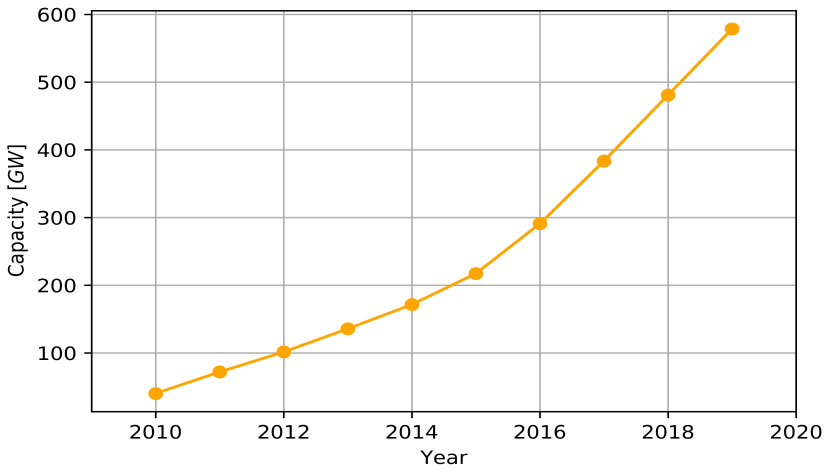

Figure 1.2: Global solar PV energy capacity (data acquired from [8])

Solar energy continues to be an integrated application used in everyday life with constant major breakthroughs in the development of photovoltaic technologies and providing various applications of freely accessible and green energy on earth. The development of solar PV technologies demonstrates an important global sustainable energy system. With technological advancement, alternative innovative techniques are easier to explore for promoting energy-efficient and clean energy production, particularly solar PV. Solar PV technology converts solar radiation into DC electricity [10]. Solar PV is the most widely accepted and rapidly growing 'green' power generation technology. However, the implementation of solar PV systems is hindered in many populated countries due to shortage of land space [11]. As land scarcity increases worldwide, it is difficult to deploy conventional ground-mounted and roof-top solar PV systems. Thus, limiting the widespread use of PV systems in land-scarce countries due to space constraints. Therefore, alternative forms of solar PV technologies are required.

1.2 Floating Solar PV System

The various components comprised in floating PV installations are discussed in this section. The benefits and challenges related to deploying the floating PV system are also addressed. A detailed study about the global capacity of FPV installations, review of the top FPV projects, and the latest trends in floating PV technology is provided as well.

1.2.1 Building Blocks of an FPV system

Approximately 71 % of the Earth's surface is covered by water [12]. Taking into account the ratio of the Earth's surface covered with water respect to the land, assessing the full potential of solar energy application and utilising the concept of solar PV systems on the water surface is a good start to address the electricity crisis. Floating (FPV) PV systems, which is often also known as "floatovoltaic" systems, are the new ecological and sustainable alternative solution allowing installation of solar PV over water bodies such as a lake, ocean, an artificial basin or in a hydropower reservoir [13], [14].

The floating PV system is installed in water bodies such as lakes, pond, canal, reservoirs, etc [14]. The FPV installation consists of floating structures often known as floats or pontoons, PV modules and its mounting structures, inverters, the mooring system, and balance of system (BOS) components [14]. Figure 1.3 shows the key components comprised of a typical large-scale FPV system. The floating PV modules are mounted on top of the buoyancy floats. The layout of the FPV system is similar to a conventional land-based PV system, except that the PV arrays are mounted on the floating platform and often the inverters and the combiner box as well [13], [14]. The FPV system is kept in a stable position with an anchoring and mooring system [13], [14]. The floating installation can either be anchored underwater or on-shore. There is also a lightning protection system to protect the FPV system from fires caused by lightning-induced currents, direct strikes or mechanical destruction [15]. Underwater grounding methods can be used, and electrodes typically mounted on the metal structure connecting the modules [16].

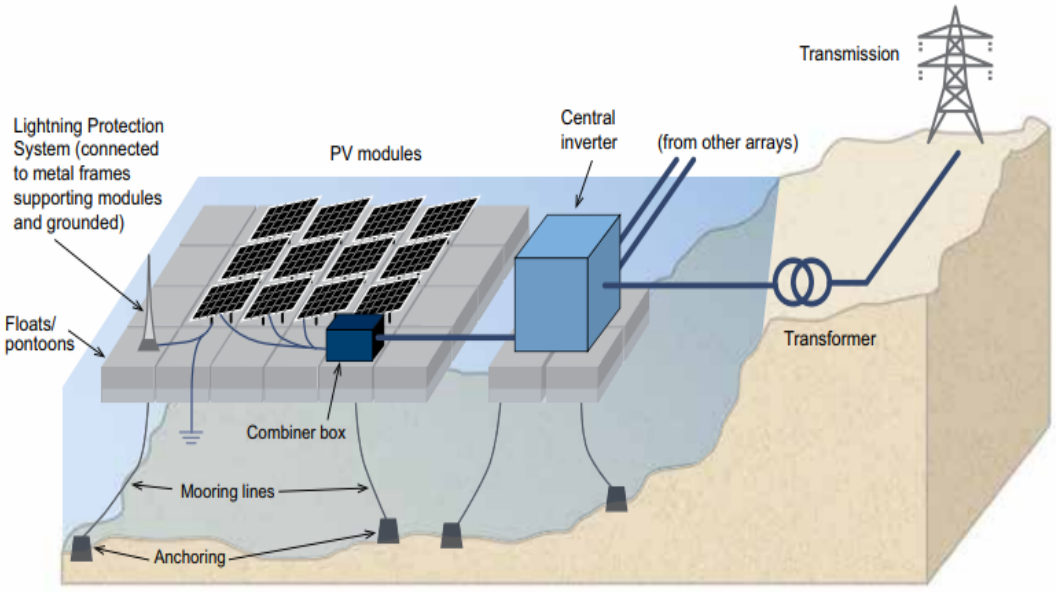

Figure 1.3: Key components of a FPV system [15]

1.2.2 Costs of Floating PV

In comparison to land-based PV systems, floating PV technology have a slightly higher capital cost [15]. The cost associated with deploying floating PV will have a higher degree of uncertainty as the cost is dependent on multiple factors, such as the components used, and the anchoring and mooring system. In 2018, on an average the total investment cost for an FPV system varied between $\$0.8/Wp$ and $1.2/Wp$ [15]. These estimations are based on the FPV system's size and location. The capital expenditure (CAPEX) of a hypothetical 50 MWp FPV installation in comparison to a gound-mounted system is presented in Table 1.1. Both systems are assumed to be fixed tilt at the same location, and the FPV system is considered an inland freshwater reservoir with a 10 meters depth [15]. The mounting system for FPV comprises of the floating structure, and the mooring and the anchoring system. The balance of system (BOS) includes the monitoring system. With an assumed performance ratio of the hypothetical 50 MW FPV system to be 10 % higher than the ground-mounted system, the Levelized cost of electricity (LCOE) of the FPV system is reported to be between 3 % to 4 % higher in comparison to the ground-mounted PV system [17].

Table 1.1: A comparison of CAPEX of a ground-mounted vs. FPV system [15].

CAPEX components	FPV [$/Wp]	Ground-mounted PV [$/Wp]
Modules	0.25	0.25
Inverters	0.06	0.06
Mounting system	0.15	0.10
BOS	0.13	0.08
Design, construction, T&C	0.14	0.13
Total CAPEX	0.73	0.62

1.2.3 Review of FPV projects

In 2007, the world's first FPV power plant with a 20 kW capacity was implemented for research purpose in Aichi Prefecture in central Honshu of Japan [18]. However, in 2008, the world's first commercially installed floating solar power plant was built with a capacity of 175 kWp at the Far Niente Winery in California [18]. The idea behind floating solar technology was to make better use of the water surfaces to produce renewable energy from the sun while saving valuable acreage in the vineyard and also better usage of polluted water bodies or underutilised wetlands [18].

Floating PV is a growing technological trend for up-scaling renewable energy generation capacity from solar energy and is attracting the interest of the investors, utilities and the research communities worldwide [15], [19]. FPV systems are currently identified as a key modifier to more sustainable energy generation. FPV has continued to gain global popularity as more and more countries are starting to implement FPV systems [15], [20]. Due to the proven reliability of FPV systems, the global cumulative installed FPV capacity, according to the Solar Energy Research Institute of Singapore (SERIS), has reached an incredible milestone of 1.6 GW in 2019 [20]. As of June 2019, floating solar market emerges with 200+ global floating solar plants [19]. Table 1.2 shows the total installed capacity of FPV projects around the world at the end of June 2019 [21]. With 97 % of the FPV projects being implemented in Asia. As the rest of the countries in the world continues to implement and recognizes the benefit of implementing FPV systems, Africa also takes a step towards becoming actively involved in sustainable energy generation. In March 2019, the first commercially-operated floating solar system on the African continent of 59 kW was unveiled on an agricultural reservoir in Marlenique, South Africa [22].

Table 1.2: The global capacity of FPV installed plants (data acquired from [19]) [21].

Location	Installed Capacity [kW]
Asia	813 788
Europe	19 915.31
America	1784
Middle East	1319.10
Oceania	130
Africa	59

Table 1.3 presents the top 10 FPV installations globally as of June 2019. Overall, China dominates the floating solar market worldwide, with the most installed floating PV systems as well as owners of the top FPV projects.

Table 1.3: The top 10 FPV plants installed globally, as of June 2020 [20], [23].

Rank	Size [kWp]	Name of Plant/ region and/or Country	Year
1	150 000	Guqiao Huainan / China coal subsidence	2017
2	150 000	Anhui province, China	2018
3	102 000	Xinji Huanian / China coal subsidence	2017
4	100 000	Weishan Jining / China large-scale waters	2018
5	70 005	Anhui CECEP, China	2019
6	70 000	Coal mining subsidence, Huainan City, China	2019
7	50 000	Huancheng Jining / China coal subsidence	2018
8	47 500	Da Mi Hydropower Reservoir, Vietnam	2019
9	40 000	Coal mining subsidence, Huainan City, China	2016
10	40 000	Renlou coal mine, Huaibei City, China	2017

Floating PV systems and bi-facial modules are both technologies which are accelerating rapidly in the PV sector [24]. Bi-facial modules have a double-sided energy factor as it produces from both sides of the PV modules, which effectively increases the energy production [25]. However, bi-facial modules are only beneficial for installation when the surface reflectivity, i.e. albedo, is high. A higher albedo results in reflecting more radiation on to the rear side of the module. With the aim of integrating bi-facial module on water, the worlds first bi-facial floating PV, and the first operational FPV project on seawater in the Middle East is deployed in the United Arab Emirates (UAE) [26]. It's a small offshore pilot project with an installed capacity of 80 kWp [26].

Lately, installations of floating solar tracking system technology are trending. In September 2020, installation of a floating and sun-tracking PV system in

Oostvoornse Lake, Holland was deployed [27], [28]. The single-axis tracking FPV system holds 130 floating PV modules with an installed capacity of 50.7 kWp [28]. The function of the tracking system is to gradually adjust the rotation of the floating PV panels towards the sun during the day. Trackers make floating PV technology more efficient and competitive.

The hybridization of hydroelectric dams with floating solar power plants will facilitate the appropriate and cost-effective management of electricity and water [29]. This can reduce dependence on conventional power plants and oil/coal-fired plants and thus reduce carbon emissions.

1.2.4 Advantages of FPV

Floating solar PV systems attributes a viable solution in vastly overpopulated cities and smaller communities which are located closer to the shores. Thus, the need for long transmission lines is reduced. FPVs are a primary solution for islands. Especially, for the aqua cultural industry FPVs can be an alternative to diesel generators, and effectively reducing the noise, fuel costs, greenhouse gas emissions and producing clean, renewable energy [11], [15]. According to a research team from Norway and Switzerland, clusters of marine-based floating PV islands have the potential to convert CO_2 to methanol fuel which may help reduce the greenhouse gasses in the environment [30].

Floating solar PV panels on water does not require valuable land space, therefore providing flexible land management [23]. Floating PV installations can be deployed on any unused water bodies, such as wastewater treatment ponds, hydroelectric dam reservoirs, or drinking water reservoirs [15]. Floating PV systems contributes to various environmental benefits. Floating structures or pontoons on which the solar panels are mounted shades the water body which helps in reduction of evaporation and the presence of algae blooms [31], [32]. Algae blooms are harmful to human health if present in the drinking water source. It can cause depletion of oxygen in the water body and block incoming sunlight from reaching plants and aquatic animals. Water loss through evaporation can accelerate over time and contribute to water shortage, therefore, implementing floating solar can be beneficial in areas that are susceptible to drought [23].

Floating solar panels on the water body can help in the reduction of temperature losses [18]. In comparison to traditional land-based PV systems, floating PV is 11 % more efficient [33]. Lower operating module temperature from evaporative cooling effect increases the floating PV energy yield [34], [35]. Research work from Liu et al. found a 1.58-2.00 % increase in efficiency of the FPV systems in comparison with the traditional terrestrial PV systems [36]. Azmi et al. found the FPV efficiency to be 2.82 % and 14.58 % higher than

a conventional PV module at the solar radiation intensity of 667 W/m^2 and 834 W/m^2, respectively [37]. Trapani et al. reported a 5 % higher electrical improvement of the floating PV through a 3-day comparison test with the terrestrial PV [38]. While another research work reported a total energy gain by the floating PV module to be 15.5 % higher than a normal PV panel for a two-hour exposure to solar irradiation [39]. The difference in the energy yield of the floating PV system is due to multiple factors, such as mounting of PV modules on the water surface, the PV system used, and the environment. In comparison to traditional PV systems, the floating PV system is less prone to shading effect due to open and flat water bodies [13], [15]. FPV systems are also less prone to soiling due to dust in comparison to solar farms in the desert area [15]. The floating PV modules can possibly be also washed by the waves which effectively reduces cleaning of the PV modules.

1.2.5 Challenges with FPV

In spite of the numerous advantages of floating PV installations, there are still various challenges in using this innovative technology which needs to be identified and assessed [15], [23] . Deploying floating PV on calm water bodies such as ponds, lakes, or reservoirs, the floating installation is not exposed to harsh climatic weather. In comparison to installation on the oceanic water surface, the floating PV system becomes more vulnerable to waves, currents and possibly storms as well which may adversely affect the lifespan of the floating PV system [15], [23]. Significant increase of the dynamic loads during adverse weather events may severely impact the rigidity of the floating structure and increasing rough motion of the water surface may induce stresses on the floating installation [15], [23]. Victim of a severe disaster was Japan's largest floating PV installation which caught fire by the Typhoon Faxai impact in September 2019 [40]. The 13.7 MW floating plant at the Yamakura Dam was damaged by 120 mph wind speed [40]. The strong winds dismantled and stacked up floating solar panels which created conditions for overheating the modules [40]. FPV installations may also interrupt recreational usage of the water bodies.

Floating PV systems are also susceptible to an increased risk of corrosion which may possibly reduce the designs lifespan [15], [23]. Uncertainty still remains with respect to the degradation effect and accumulation of salt on the PV modules if installed on seawater [15], [23]. If the inverter is placed near or offshore (which is mostly the case for many floating PVs) the inverters and the balance of system (BOS) components experiences a higher humidity environment. Some negative environmental impacts may have an effect on the aquatic ecosystem of the flora and fauna development [15], [23]. Bird droppings, nesting and biofouling may also occur which can possibly affect the production yield of the floating PV system in the long run [15], [23]. Correspondingly, a

concrete stipulation of the Health and Safety standards related to the floating PV installation, the mooring system, and the O&M procedures require much attention [15], [23].

Degradation effect of the FPV system, as well as corrosion from water and soiling from salt also needs much investigation [17]. In order to ensure successful implementation and to make the FPV technology more attractive to investors, financial models should be developed to ensure that end-users receive the full benefits of an FPV investment. Most importantly, a comprehensive feasibility study should be conducted to identify project cost in detail, including the total cost of ownership, and not only the initial capital cost. Currently, there are no clear and specific regulations on licensing and permitting of FPV plants [17]. Currently, processes for deployment of FPV plants are assumed to be the same as for the traditional ground-mounted PV plants [17]. Therefore, policy and regulatory considerations on licensing and permitting of FPV plants should be clearly documented and addressed.

1.3 Problem Statement

As the interest of the floating solar PV market grows worldwide, there are still many challenges which remain to be addressed in well-documented research work for providing quantified solutions. However, due to the large investments needed for the installation of an FPV plant, investors are eager to understand the benefits of a potential installation of a large-scale floating solar PV plant to the solar energy sector [41]. Various research has demonstrated the capability of floating PV to produce an increased electrical power output when compared to the conventional solar PV installations for the same installed nominal power [37]. The increase in production from FPV is mainly due to the lower operating temperature of the modules [31]. Lower module temperature is caused by the cooling effect from the water [31], [38], [42].

Due to financial constraints, very few FPV solar plants have been instrumented for research purposes. Thus, generating a lack of accessible and reliable FPV data to understand the various impact on the power generation capability of an FPV system. With the growing interest of FPV and bi-facial modules, the impact of the water surface reflectance possesses an intriguing investigation and is of interest. The main research question is formulated as follows: what is the impact of the albedo and the heat transfer on the floating PV system?

Currently, most floating PV technology concepts consists of modules installed on floating pontoons [23], [43], [44], while only a unique floating PV concept consist of a module installation on a flexible floating structure that is in thermal contact with the water surface [45]. This unique floating PV solution

provides a concept whereby modules are installed flat onto a thin polymer canvas [45].

Currently, varying water surface albedo is not integrated into PV simulation software. In the absence of measured reflected radiation from water, a default albedo value of 0.2 is commonly used to simulate FPV systems [46]. Thus, investigating the time-varying water surface albedo for FPV system is important to understand the impact of the water albedo on the annual energy yield. In the past years, researchers have also investigated the reflectance properties of the water surface and indicated the extent to which FPV modules have a better cooling effect when been installed on floating pontoons, with the modules being at a specific tilt angle [31], [38]. However, due to confidentiality agreements by various research institutes and companies, very little information is accessible to the public to understand the potential of installing flat-mounted FPV modules in direct thermal contact with the water surface. Thus, investigating the cooling effect of a flat-mounted FPV system, in thermal contact with the water surface, is of great interest.

1.4 Aim and Objectives

The research presents the modelling of the time-varying water surface albedo with the change in solar elevation; as any changes in weather patterns will strongly influence the radiation received on the FPV modules and reflection off the water surface. The research aims to investigate the cooling effect and the albedo effect on the yield of a floating PV system. The main objective is to conduct a study on the performance of a very specific floating PV technology which utilises the concept of deploying floating modules on a very thin flexible polymer floating structure on the water surface. Mainly, identifying the difference in the performance analysis of an elevated air-cooled string and a water-cooled string which is in thermal contact with water. Furthermore, closely inspecting the difference in the module temperature of both the floating PV strings and performance of the thermal model on the FPV strings in comparison to a ground-mounted string. A floating PV system is also simulated using PV simulation software to analyse the difference in estimated production at different thermal loss factors.

The proposed objectives in this thesis aim to address the following:

- Develop a water surface albedo model for FPV solar plants.
- Investigate the impact of the water surface albedo on the floating PV solar collector.

- Conduct a performance analysis of an air-cooled and a water-cooled floating PV string.
- Analyse and compare the difference in the production and the module temperature of an air-cooled vs. a water-cooled floating PV string.
- Investigate a thermal model to estimate the cooling effect on an air-cooled vs. a water-cooled floating PV string in comparison to a ground-mounted PV string.
- Evaluate and compare the heat loss coefficient for floating PV system vs. ground-mounted PV system.
- To simulate an FPV system using a PV simulation software, PVsyst, to analyse the difference in the estimated production at different thermal loss factors, and to understand the influence of the tilted panels at various tilt angles on the energy yield of the FPV system using the default albedo value of 0.2 (as commonly used and proposed by PVsyst) vs. the modelled water surface albedo.

1.5 Thesis Layout

To address the research objectives and aims as posed in Section 1.5, the thesis outline is structured as follows:

- Chapter 2 presents the reader with a brief introduction to the theoretical background of solar PV and the wave theory of light. The single diode model is discussed in detail and how the solar irradiation and temperature affects the I-V characteristics. Thereof, a brief overview of the SERIS testbed is provided together with the measured albedo and the investigated heat loss coefficients, U-values, for the different floating PV structures. Furthermore, a brief introduction to optics at an air-water interface is discussed together with the albedo effect of water and Fresnel's effect. The mathematical evaluation of the refractive index of air and water is formulated. Finally, appropriate models of the direct beam radiation, sky diffuse radiation and reflected radiation is described.
- Chapter 3 presents the research work related to albedo modelling and the modelling approximations. A detailed description of the weather station and its instrumentation set-up from which the solar radiometric data is retrieved is also provided. The procedure for data acquisition and filtering the datasets is also described. The clear sky models used to predict the clear sky irradiance are provided with a detailed explanation. The result of the albedo model is given. Subsequently, the albedo effect on the solstices and equinoxes is illustrated together with the effect of the

water surface albedo on the collector insolation, and the annual energy yield.

- Chapter 4 provides detailed information about the floating solar system and the ground-mounted PV system. Site assessment and system analysis is conducted for the two different systems. The instrumentation set-up is described as well as the procedure for acquiring the data and filtering the datasets. Finally, the measured data are analysed.

- Chapter 5 provides detailed information about the approximations used to evaluate the heat transfer coefficient for a floating solar PV system and a ground-mounted PV system. The temperature data logging and retrieval from the floating PV site are explained. The application of the clear-sky filter and data cleaning process is explained. The module temperature is analysed and the cell temperature estimation is presented. Finally, the heat loss coefficient is determined for the two different solar PV systems, and a comparison is made to evaluate the differences in the heat loss for an FPV system vs. a ground-mounted PV system. PVsyst simulation software is also used to investigate the effect of the heat loss coefficient, U-value, on the annual energy yield. PVsyst simulation is also conducted to understand the influence of the tilted panels at various tilt angles on the energy yield of the FPV system using the default albedo value of 0.2 vs. the modelled albedo value of 0.02.

- Chapter 6 presents the concluding remarks of all the previous chapters relating to the research work, together with the recommendation of the possible future improvements to the research.

Chapter 2

Theoretical Background

This chapter aims to provide the reader with a brief introduction to the theoretical background of solar PV and the wave theory of light. The single diode model is discussed in detail and how the solar irradiation and temperature affect the I-V characteristics. Thereof, a brief overview of the SERIS testbed is provided together with the measured albedo and the investigated U-values for the different floating PV structures. The electromagnetic theory of light is also discussed together with the different polarisation of light. Furthermore, a brief introduction to optics at an air-water interface is discussed together with the albedo effect of water and Fresnel's effect. The mathematical evaluation of the refractive index of air and water is formulated. Finally, appropriate models of the direct beam radiation, sky diffuse radiation and reflected radiation is described. The background study in this chapter plays an important role in building the foundation knowledge in addressing the reasearch objectives.

2.1 The Sun

The Sun is a star situated at the center of our solar system. The hot plasma makes the Sun an extremely powerful source of energy that converts hydrogen nuclei into helium through a nuclear fusion reaction in its core [47]. The nuclear fusion reaction enables the Sun to emit tons of energy in the form of solar radiation. The total power emitted per second by the Sun is 3.8×10^{20} MW [48]. However, only a portion of that reaches the Earth's atmosphere due to the distance between the Earth and the Sun. The energy received from the Sun outside the Earth's atmosphere is an average value of 1367 W/m^2 which is called the solar constant [48]. It measures the rate at which the energy reaches the Earth's surface perpendicular to the rays of the Sun.

Sunlight can behave simultaneously as a particle or a wave [49]. This type of behaviour of light is commonly known as the wave-particle duality [49], [50]. The Sun emits 'packets' of energy called photons [48]. These photon's energy

is expressed according to Planck's law as [48], [49], [50]:

$$E_{ph} = h \times v, \tag{2.1.1}$$

where E_{ph} is the energy of the photon, v is the frequency of light and h is Planck's constant.

To demonstrate the effect of the solar irradiation travelling through the atmosphere, the air mass (AM) ratio is used [48]. The air mass ratio indicates the amount of atmosphere that the irradiance must penetrate through to reach the earth's surface and is expressed as [48], [49]:

$$AM = \frac{h_2}{h_1} = \frac{1}{\sin(\beta)}. \tag{2.1.2}$$

Whereby, h_1 is the length from the Earth's surface through the atmosphere with the Sun directly overhead, h_2 is the length from the Sun through the atmosphere to reach a specific point on the Earth's surface, and β is the altitude angle of the Sun [48]. A detailed explanation of the calculation of the altitude angle is discussed in Section 2.7.

Figure 2.1 illustrates the relevant parameters corresponding to the air mass ratio. The air mass ratio of 1 (designated 'AM = 1') indicates that the Sun is directly overhead.

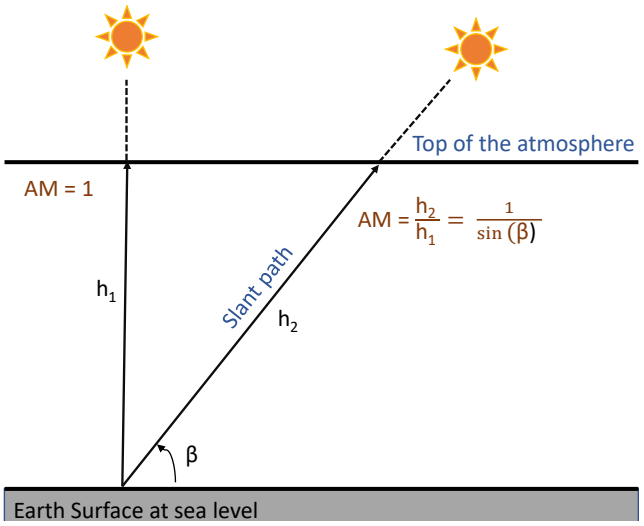

Figure 2.1: The air mass ratio.

2.1.1 Solar Irradiance and Solar Insolation

Solar irradiance is a measurement of the solar power received from the Sun to the Earth's surface in the form of electromagnetic radiation [47]. It is defined

as the instantaneous power density measured in units of W/m^2. The intensity of the incoming solar irradiance at the surface of the Earth is strongly dependent on a variety of factors such as the location, climate, altitude, season, cloud coverage and time of the day. There are three types of solar irradiance received at the Earth's surface namely direct irradiance, diffuse sky irradiance and reflected irradiance. Diffuse sky irradiance is caused by direct and scattered sunlight [48]. Reflected irradiance is due to the direct and diffuse irradiance [48].

The solar insolation or irradiation is a measurement of the cumulative electromagnetic energy received at the Earth's surface [47]. It is measured at a specific location for a defined time period such as daily, monthly, and annual. The common measurement units of the insolation is kWh/m^2, $kWh/m^2/day$, $kWh/m^2/month$, or $kWh/m^2/year$.

Global Horizontal Irradiance (GHI) is the total amount of solar irradiance in the form of shortwave radiation received on a surface horizontal to the Earth's surface. The most common instruments used to measure GHI is a reference cell or the pyranometer with a hemispherical (180 $^{\circ}C$) view angle [47]. In the absence of measured GHI, GHI may be calculated as the sum of the Direct Normal Irradiance (DNI), corrected for the angle of incidence, and the Diffuse Horizontal Irradiance (DHI).

2.2 Solar Photovoltaic

2.2.1 Single Diode Model

When a solar PV cell is exposed to incoming light, a photoelectric current is generated which is proportional to the solar irradiance. Under specific operating conditions equivalent circuit models are used to define the current-voltage (I-V) curve of a cell as a continuous function. One of the basic equivalent solar cell model commonly used is the single diode model which is also known as the five-parameter model [51], [52]. The single diode model is derived from the physical principles that are represented by [53]. Figure 2.2 represents the one-diode equivalent circuit for a single solar cell. An ideal PV cell does not have the shunt resistance, R_{sh}, and the series resistance, R_s [54].

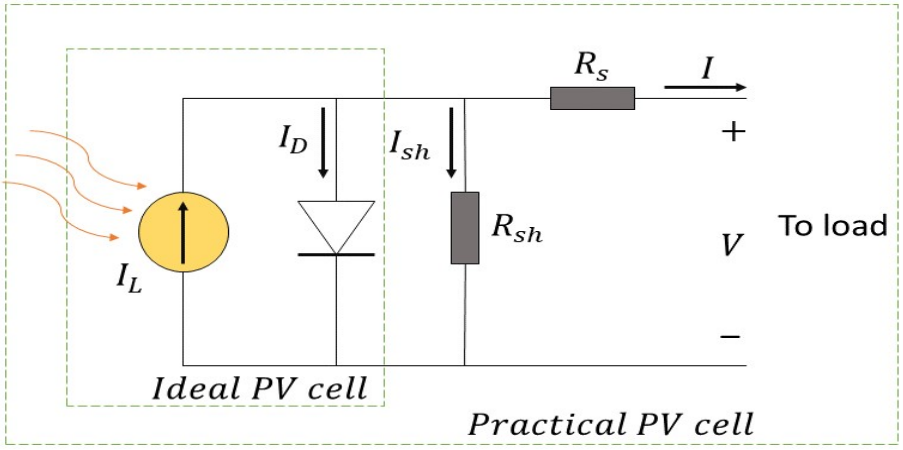

Figure 2.2: Single diode equivalent circuit of a PV cell.

A practical PV cell is modelled by adding the effect of the parasitic resistances, shunt and the series resistances [54]. The series resistance accounts for the physical distances in contacts and the semiconductor layers and the shunt resistance represents the leakage currents.

Using Kirchhoff's current law, the output current, I, of a practical PV cell is calculated as [51], [52]:

$$I = I_L - I_D - I_{sh}. \tag{2.2.1}$$

Whereby, I_L is the light-generated current in the PV cell, I_D is the diode current, and I_{sh} is the shunt resistance current. When light is exposed on the PV cell the output of the current source is directly proportional to the incoming light. For an ideal diode the diode current, I_D, can be calculated using the Shockley equation as [51]:

$$I_D = I_o[exp(\frac{V + IR_s}{nV_T}) - 1]. \tag{2.2.2}$$

Where, I_o is the diode reverse saturation current or the 'dark' saturation current, V is the load voltage, V_T is the thermal voltage, and n is the diode ideality factor. The diode ideality factor, n, is unitless. For a single junction cell the diode ideality factor usually ranges between 1 and 2. The diode ideality factor near to 1 is represented at high currents, and rising towards 2 at low currents [55]. The thermal voltage is given by [51]:

$$V_T = \frac{kT_c}{q}, \tag{2.2.3}$$

with k representing the Boltzmann's constant ($1.381{\times}10_{-23}\ J/K$) and q the electron charge ($1.602{\times}\ 10_{-19}\ C$). The leakage current through the shunt resistance, I_{sh}, is calculated as [51]:

$$I_{sh} = \frac{V + IR_s}{R_{sh}}. \tag{2.2.4}$$

Recombining the diode current equation and the shunt current equation, the complete governing equation of the total output current for a single diode model is given by [51]:

$$I = I_L - I_o[exp(\frac{V + IR_s}{nV_T}) - 1] - \frac{V + IR_s}{R_{sh}}. \tag{2.2.5}$$

The output power from a PV cell can be calculated as $P = I \times V$. The five unknown parameters that are primary to all single diode models are [51], [52]:

- R_s: Series resistance in unit of Ω.
- R_{sh}: Shunt resistance in unit of Ω.
- I_L: Light-generated current in unit of A.
- I_o: Diode reverse saturation current in unit of A.
- n: Diode ideality factor (dimensionless).

For a PV module, multiple PV cells are connected in series that are represented by N_s. Assuming that all the PV cells are identical and operating under uniform and equal irradiance and temperature, such that the PV cells generate equal current and voltage, the module voltage, V_{mod}, is calculated as [51]:

$$V_{mod} = N_s \times V_{cell}. \tag{2.2.6}$$

Whereby, V_{cell} is the voltage of the PV cell. The module current with multiple PV cells, I_{mod}, calculated as [56]:

$$I_{mod} = I_L - I_o[exp(\frac{V_{mod} + I_{mod}N_sR_s}{nN_sV_T}) - 1] - \frac{V_{mod} + I_{mod}N_sR_s}{N_sR_{sh}}. \tag{2.2.7}$$

In some implementations, such as De Soto et al., a modified ideality factor, a, is given by [52]:

$$a = \frac{N_s n k T_{cell}}{q}. \tag{2.2.8}$$

The modified ideality factor parameter, a, depends on the cell temperature, T_{cell}, and not on the irradiance level [52]. The output power from a PV module can be calculated as [51]:

$$P_{mod} = I_{mod} \times V_{mod}. \tag{2.2.9}$$

2.2.2 I-V characteristics of a PV cell

The I-V characteristics are the plot of the total output current, I, and the total output voltage, V. To plot the I-V characteristics of a PV cell, the load voltage, V, is swept from zero to a maximum value, and at each voltage point a corresponding external output current, I, is obtained. The characteristic of the I-V curve changes as the operating conditions changes. These operating conditions are the cell temperature and the effective irradiance [52]. The I-V characteristics of a solar PV cell in the dark is an exponential curve which is similar to that of a diode [57]. The I-V characteristic of a PV cell is dominated by the characteristics curve of a diode [53]. The I-V characteristics curve of a typical silicon PV cell is shown in Figure 2.3. To obtain the maximum power output of a PV cell, the PV cell needs to operational at its maximum power point, P_{MP} [58]. The maximum power occurs at the maximum voltage, V_{mp}, and the maximum current, I_{mp}.

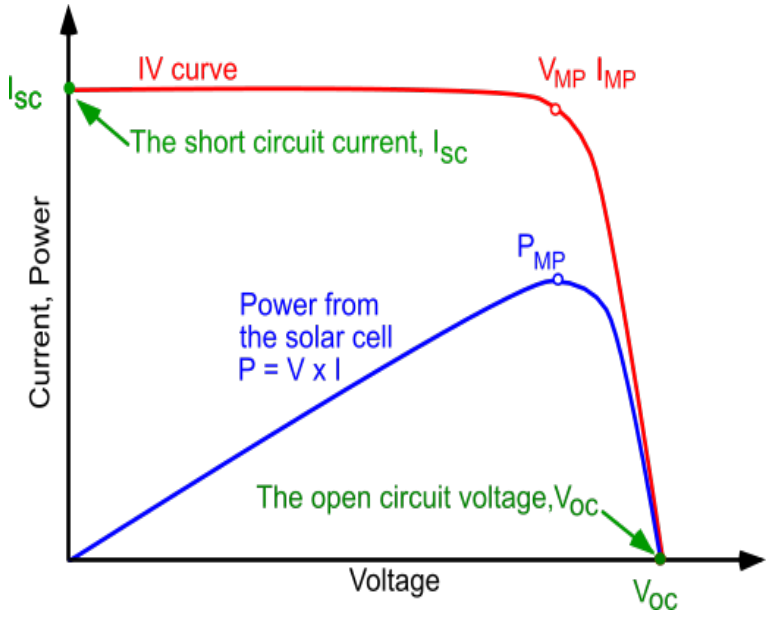

Figure 2.3: I-V characteristics of a single PV cell [58].

When the equivalent circuit of the PV cell is short-circuited, the output voltage to the load is zero. Short-circuit current, I_{SC}, is the maximum current obtained from the PV cell when the voltage is zero. With smaller values of R_s and voltage close to zero, the current through the diode, the forward bias current, is very small. Therefore, the maximum current is attainable from the PV cell, i.e. $I_{SC} = I_L$. I_{SC} greatly depends on the solar irradiance level, the solar spectrum of the light, the area of the solar cell and the characteristics of the material used in the PV cell [53]. The open-circuit voltage, V_{OC}, is the maximum voltage obtained from the PV cell when the external current is

zero. V_{OC} depends on the quality of the material, specifically the value of the dark saturation current, I_o. The lower the value of I_o, the higher the quality of the material and thus higher the V_{OC}. Manufacturers specify short-circuit current and the open-circuit voltage on the data sheet of a given PV module under STC conditions. STC condition is specified at a irradiance level of 1000 W/m^2, air mass AM of 1.5, and the ambient temperature of 25 $°C$ [48], [53].

2.2.3 Effects of Irradiance and Temperature

The effect of the environmental conditions such as the solar irradiance and temperature on the I-V characteristics is important to understand the operation of a PV cell. For illustration purposes, the I-V curves for a BP 3 Series 235 W solar panel from BP Solar is presented in this section to understand the effect of the variation of solar irradiation and temperature on the I-V characteristics. Figure 2.4 presents the I-V curves for a single PV cell of a BP 3 Series 235 W panel at an air mass ratio of 1.5, operating cell temperature of 25 $°C$, and solar irradiation at five levels: 1000 W/m^2, 800 W/m^2, 600 W/m^2, 400 W/m^2 and 200 W/m^2 [56].

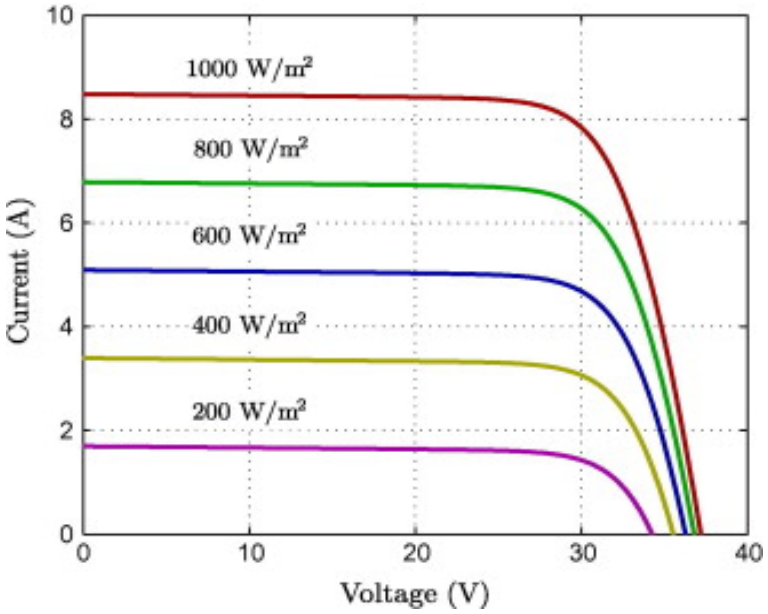

Figure 2.4: I-V characteristics of a single PV cell at different irradiance level [56].

The effect of the irradiance mainly affects the light-generated current or the photon current, I_L. Photon current is equal to short-circuit current under the assumption that the R_s is very small, as previously shown in Subsection 2.2.2. Therefore, the variation of irradiance mainly affects short-circuit current as shown in Figure 2.4. I_{SC} varies linearly with the solar irradiance level. V_{OC}

increases as the irradiance levels increases. However, since the V_{OC} does not change much at different solar irradiation, the dependence of V_{OC} on the solar irradiance is not very significant.

The temperature also affects the I-V characteristics of a PV cell. Figure 2.5 presents the I-V curves for a single PV cell of a BP 3 Series 235 W panel at the same irradiation level of 1000 W/m^2, air mass AM of 1.5, but with varying cell temperatures: 0 $°C$, 25 $°C$, 50 $°C$ and 75 $°C$ [56]. The most dominant effect of cell temperature is on the open-circuit voltage, V_{OC}, with a temperature coefficient that is specific to the module type as shown in Table 2.1. The open-circuit voltage decreases drastically with an increase in cell temperature as shown in Figure 2.5. The drop in the open-circuit voltage with temperature is mainly due to the increase in the dark saturation current, I_o, with temperature [52]. The open-circuit voltage decreases as the band gap decrease [59]. The maximum power point decreases with an increase in cell temperature. Therefore, at higher cell temperatures, for the same solar irradiance level, significantly lower power output is attainable. Therefore, V_{OC} has a strong temperature dependency and a very high negative temperature coefficient.

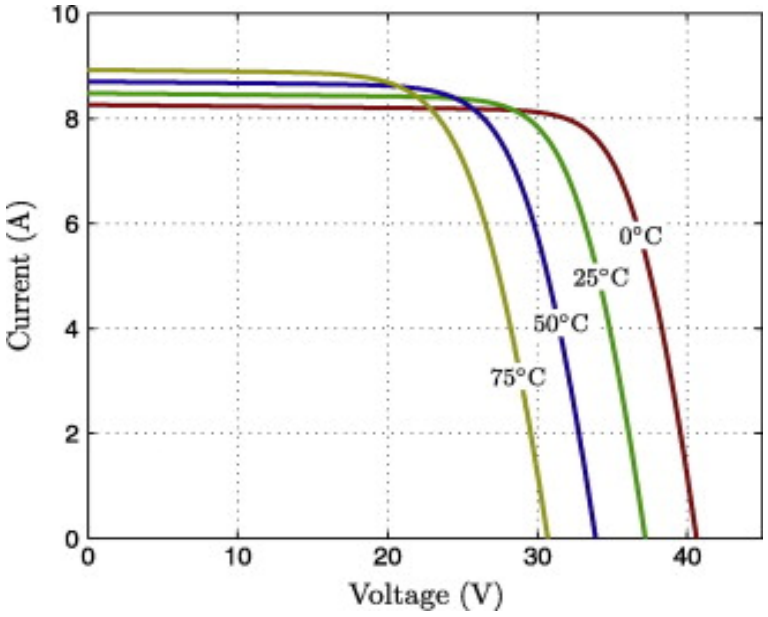

Figure 2.5: I-V characteristics of a single PV cell at different temperatures [56].

The temperature effect on I_{SC} increases slightly. Higher temperatures increase short-circuit current, but the increase is very small as shown in Figure 2.5. The small increase in I_{SC} at higher temperatures occurs because of the material's bandgap which decreases with the temperature [59]. Therefore, for a given

irradiance there are more electron-hole pairs created at the higher temperatures, thus resulting in slightly higher short-circuit current. I_{SC} variation with temperature increases 0.05 % for every $°C$, and therefore is usually neglected.

The PV temperature coefficient of power affects the power output of the solar PV module [60]. Manufacturers of the PV modules specify the temperature ratings on the data sheet. The temperature coefficient of maximum power indicates how strongly the power output of a PV module depends on the cell temperature [60]. It is given as a negative number because the power output decreases with an increasing cell temperature [60]. Table 2.1 presents the average values of the temperature coefficient of power for the various PV module types.

Table 2.1: Temperature coefficient of power for various PV module types [60].

PV Module Type	**Temperature Coefficient** [$\%/°C$]
Polycrystalline silicon	-0.48
Monocrystalline silicon	-0.46
Monocrystalline/amorphous silicon hybrid	-0.30
Thin film amorphous silicon	-0.20
Thin film CIS	-0.60

2.3 SERIS FPV testbed

In 2016, Solar Energy Research Institute of Singapore (SERIS) deployed the world's largest FPV testbed consisting of 8 different system configurations in terms of PV modules, floating structures and inverters [13]. The testbed has a total installed capacity close to 1 MWp [13]. SERIS aims to study the performance benefits and issues encountered by the high-quality FPV measurement data. The floating structures at the FPV testbeds are categorized based on the water surface coverage (water footprint) and ventilation. The floating structures at the testbed are categorized as follows:

- 'Free-standing' - with PV modules mounted higher above the water surface covering a smaller water-surface area [13],
- 'Small footprint' - with PV modules mounted closer to the water surface covering a smaller water-surface area [13],
- 'Large footprint' - similar to 'free-standing' but covering a larger water-surface area [13], and
- 'Insulated' - similar to 'large footprint' but with PV modules mounted in a compact and dual-pitch design [13].

The FPV testbeds are instrumented to measure various parameters for a critical analysis. To effectively quantify the cooling effect amongst the different floating structures, the heat loss coefficient (U-value) is investigated. The distribution of the calculated U-values for the different types of floating structures from the FPV testbed is shown in Figure 2.6. The cooling effect which is indicated by the heat loss coefficient is dependent on the floating structures. The 'free-standing' floating structure type has higher U-values compared to other floating structure types. The higher U-values correspond to a better cooling effect, and thus a lower module temperature which effectively contributes to better electrical performance and vice versa. The 'insulated' system has very little heat exchange with its environment, which effectively corresponds to the lower U-value. Figure 2.6 also indicates the U-values that are commonly assumed as dashed lines for a well-ventilated (29 W/m^2K) and an insulated (15 W/m^2K) ground-based or rooftop systems in PV simulation software, such as PVsyst [13], [46].

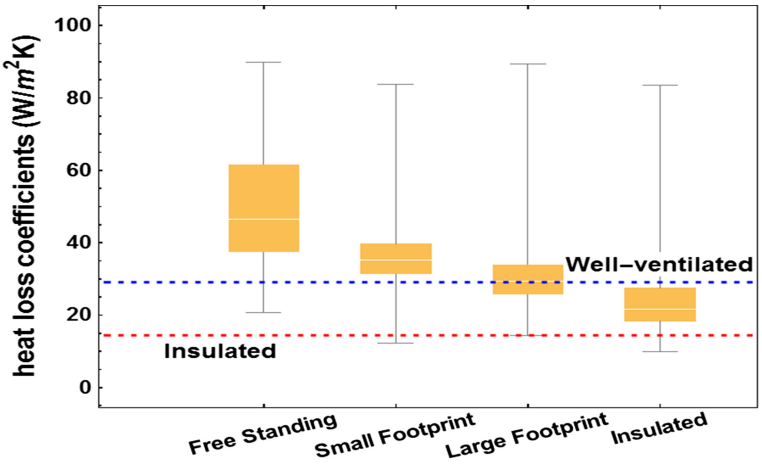

Figure 2.6: U-values for different types of FPV systems [13].

2.4 The Wave Theory of Light

2.4.1 Background

The history of the research on light dates back to the Era of the Ancient Greece [61]. Many renowned philosophers, scientists and mathematicians made pioneering contributions to various scientific disciplines. Amongst these was the establishment of the optical theory of light. The geometry of vision has since then begun evolving. A French physicist, Augustin-Jean Fresnel (1788-1827), improved the wave theory of light which was previously introduced by physicists, Christiaan Huygens and Thomas Young [62]. In this theory, light is introduced as an electromagnetic wave at the various spectrum of frequencies,

some of which includes visible light, UV and IR light [62]. The theory formulated ways of visualizing the electromagnetic wave propagation [62]. Fresnel's law was recognized in the field of science and physics after Augustin-Jean Fresnel accomplished his knowledge of the advanced wave theory of light [62]. Another renowned astronomer and mathematician whose discovery has become an integral part of the wave theory of light is Dutchman Willebrord Snell [63]. In 1621, Snell established that when shining a beam of light from one media to the other, the beam of light would bend upon entering the second media [63]. The angle at which the beam of light refracted was dependent on the incident angle at which the light beam enters the media [63].

2.4.1.1 Behaviour of Light

When the light from the Sun strikes any surface of a given object, there are three possible consequences which may arise. The light behaves such that it may either be absorbed by the surface, or refracted through the surface, or it may be reflected from the surface. The type of behaviour of light is stimulated depending on the material properties of the surface, the wavelength of the light and the angle of incidence on the surface [47].

Reflection of light can be subdivided into two types namely diffuse reflection and specular reflection [47]. The behaviour of the specular reflection of light exhibits a perfectly smooth surface on which the incoming radiation is scattered in a single outgoing direction [47]. Diffuse reflection is defined as the reflection of light from a given surface such that the incoming ray of light incident on the surface is scattered irregularly at various angles [47]. Diffuse reflection of light waves is typically exhibited on surfaces which are not smooth, i.e. rough surfaces. Rough surfaces demonstrate irregular and multiple orientations of the surface texture. Figure 2.7 illustrates the specular and diffuse reflection.

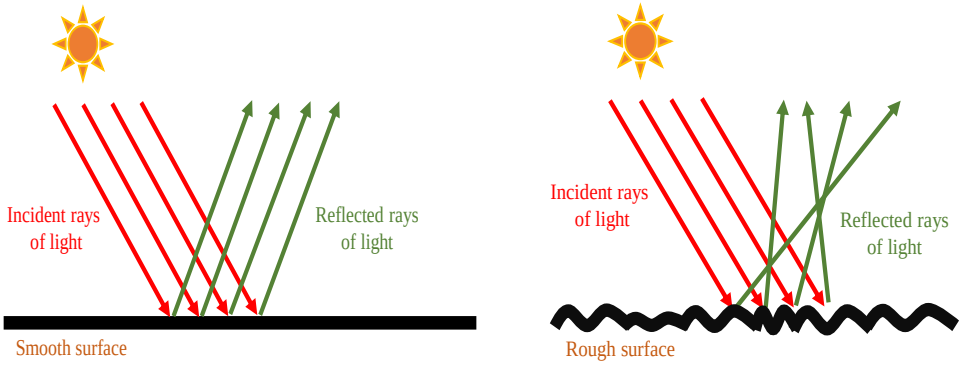

(a) Specular reflection. (b) Diffuse reflection.

Figure 2.7: Different type of reflections.

2.4.2 Electromagnetic Theory of Light

The radiation from the Sun is in the form of electromagnetic waves. There are two types of electromagnetic waves namely longitudinal wave and transverse wave [64]. The type of waves is categorized by their propagation direction [65], [64]. Particles in the wave that are displaced parallel to the direction of propagation of the wave produce longitudinal waves [66]. While transverse waves are waves which vibrates its particles perpendicular to the direction of propagation [66]. Longitudinal waves can pass through all states of matter, such as solid, liquid or gas. Transverse waves can only travel through solids and not liquids or gasses as there are no mechanisms present in liquids or gasses which can drive the motion perpendicular to its propagation of the wave. Transverse waves can travel only through solids due to solids containing enough shear strength. Typical examples of waves which attributes the characteristics of the longitudinal waves and the transverse waves are sound waves and electromagnetic radiation, respectively [65], [67]. Therefore, the radiation received from the Sun is a transverse wave.

2.4.3 Polarisation of Light

Light waves which vibrate its magnetic and electric field vectors in a single plane and propagating through a specific direction is referred to as polarised light [68]. While unpolarised lights attribute no preferred direction and its magnetic and electric field vectors propagate in random directions [68]. The light emitted by the Sun is unpolarised light. Therefore, the incident ray of light striking the water surfaces is assumed to be unpolarised such that the magnetic and electric fields particles oscillate in a randomly distributed direction.

2.4.3.1 Classification of Polarisation

The light that is transmitted or reflected through a given medium will experience vibrations either in one or more than one plane [69]. This type of behaviour of light introduces the polarisation of the electromagnetic wave. There are three types of polarisation namely, linear, circular and elliptical polarisation, which are dependent on the motion of the transverse and the longitudinal wave [64], [66]. Linear polarisation occurs when the electric field is attenuated on a single plane (either horizontal or vertical) along the direction of propagation [66]. Circular polarisation occurs when the electric field attenuates with a constant magnitude but the direction of propagation of the electric field rotates at a constant rate which consists of two linear components in a plane perpendicular to the direction of the wave with a phase difference of $\pi/2$ [66]. Elliptical polarisation occurs when the electric field vector attenuates in such a manner that an ellipse is generated consisting of two perpendicular waves of unequal amplitude with a phase difference of $\pi/2$ in a plane perpendicular to the propagation direction [66].

2.4.3.2 Unpolarised Light

The manner in which the magnetic and electric field orientates determines the type of polarisation [70]. Unpolarised direction consists of two orthogonal linear polarisations namely parallel and perpendicular polarisation with a phase difference of 90 deg and equal magnitudes [70], [71]. Parallel polarisation is when the electric field is oriented parallel to the plane of incidence, but the magnetic field is oriented perpendicular to the plane of incidence [70]. This is also known as p polarised light [71]. When the electric field is oriented perpendicular to the plane of incidence, but the magnetic field is oriented parallel to the plane of incidence, this is referred to as perpendicular polarisation which is also known as s polarised light [70], [71].

Depending on the atmosphere and the underwater environment the unpolarized light wave will become partially polarised or fully polarised [21]. The distribution of the unpolarized light wave travelling through the underwater surface is predominantly affected by the following factors [68], [69]:

- The position of the Sun in the sky.
- The amount of overcast in the sky.
- The intensity of the electromagnetic wave.
- The optical properties of the water.
- Internal scattering of light waves.
- The depth of the transmitted ray and reflection from the water surface.

- The atmospheric dust as the air molecules will influence the polarisation behaviour of light

2.5 Optics at an Air-Water Interface

2.5.1 Albedo

To specify the reflecting power of a body, or a surface area, the term Albedo is used to describe the amount of energy that is reflected. Albedo is defined as the ratio between the incoming solar irradiance on a given surface area and the reflected radiation [72]. Albedo is represented by a dimensionless ratio that is measured between a scale of 0 and 1 [73]. Whereby, an albedo value of 0 and 1 indicates that the surface area acts as a perfect absorber and a perfect reflector, respectively [74]. A perfect absorber also ultimately illustrates a perfect blackbody which internally absorbs all incident radiation that is received of all wavelengths, thus no energy is reflected through the body [75]. A perfect reflector, which is represented as a highly reflected surface will tend to bounce back all the incoming radiation [74].

There are multiple factors which determine the changes in the albedo of a given surface [74]. Different surfaces will experience a different albedo [74], [76], [77]. The albedo value varies with time and changes in albedo typically occur due to changes in the amount of cloud coverage [78], [79]. Variation in albedo is triggered by seasonal changes throughout the year [80], [81]. Table 2.2 presents the albedo values for different surfaces as given in the PVsyst software.

Table 2.2: Albedo for different surfaces [82].

Surface	**Albedo**
Urban environment	0.14-0.22
Grass	0.15-0.25
Fresh grass	0.26
Fresh snow	0.82
Wet snow	0.55-0.75
Dry asphalt	0.09-0.15
Wet asphalt	0.18
Concrete	0.25-0.35
Red tiles	0.33
Aluminium	0.85
Copper	0.74
New galvanized steel	0.35
Very dirty galvanized	0.08

2.5.2 Albedo effect of water

The albedo value of the water indicates the fraction of the incident ray which the water surface reflects back in the atmospheric environment [83]. The remaining fraction of the incident ray which is not reflected off the water surface is absorbed by the water surface [84]. The absorbed sunlight is then refracted (bent) in such a way causing multiple scattering under the water surface depending on the viscosity, the salinity of the water layers, the motion of the water particles, sediments, presence of the diverse aqua cultural ecosystem and the typical topography at the bottom of the water surface [85]. The albedo effect plays a critical role in the heat exchange process between the surface and the atmospheric environment [86]. Depending on the intensity of the refracted ray the water temperature increases which effectively energizes the heat exchange process between the air and water surface; and also stimulating the process of evaporation.

Figure 2.8 illustrates the albedo effect of the water surface with respect to the higher and lower solar elevation, respectively. The vectors of the rays are merely a representative measure illustrating the concept of the albedo effect and are not drawn to scale to present the length of the irradiance.

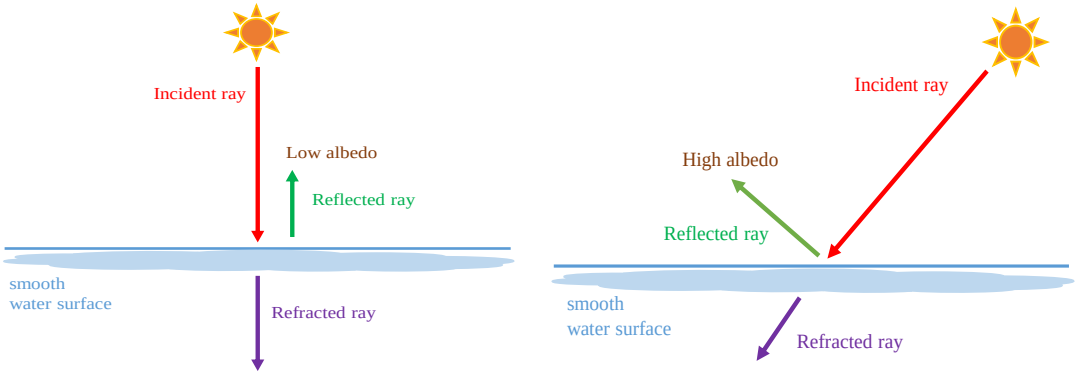

(a) Higher solar elevation. (b) Lower solar elevation.

Figure 2.8: Albedo effect [21].

When the Sun is directly normal to the water surface, by definition, all the incoming irradiance will be absorbed and the water will typically act as a perfect absorber. However, the natural phenomenon does not allow the water to behave as a perfect absorber. Typically, multiple internal refraction may occur which will cause a small portion of sunlight to reflect. Thus, the presence of albedo is indicated in Figure 2.8a. As the Sun's motion becomes closer to the horizon, during sunrise and sunset, the solar elevation decreases which cause most of the sunlight to be reflected rather than being absorbed.

The FPV testbed in Singapore recorded the albedo of the water. Figure 2.9a shows the daily weighted average albedo of the water and rooftop surfaces for a 4 months period. The albedo of the water is found to be between 5 % and 7 % only, while the albedo on the rooftop surface is recorded to be around 13 % [13]. Figure 2.9b shows the albedo for a typical day. Throughout the day, the albedo of the water surface is measured to be around 5 %. During early morning and late afternoon, the solar elevation angle is lower, which results in the water surface albedo to be higher [13]. The effect of higher specular reflection is however insignificant for PV modules which are mounted at a larger tilt angle. The fact that the albedo on the water surface is substantially lower, the water surface albedo will have a greater performance implications on bi-facial modules deployment on water [13], [87].

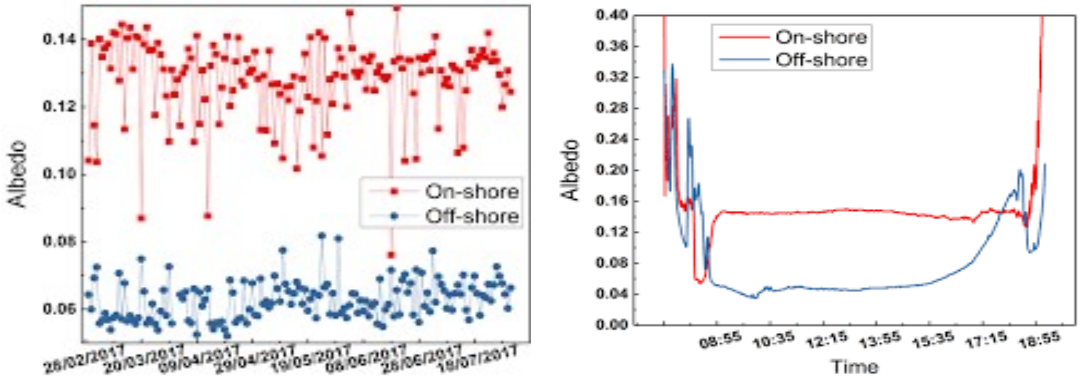

(a) Daily weighted average albedo for water and rooftop surfaces.

(b) A typical day's albedo for water and rooftop surfaces.

Figure 2.9: Albedo measurements at Singapore's FPV testbed [13].

The albedo effect of water has a significant impact on the aquatic climate [88], [89]. With lower water albedo values, the temperature of the water bodies increases due to a large amount of sunlight that gets absorbed by the water [88]. With higher water albedo values, a greater amount of radiation is returned to space due to the water surface being more reflective [88]. The term albedo means 'whiteness' which is derived from Latin, therefore white surfaces such as ice and snow have higher albedo values, whereby dark surfaces will have lower albedo values [73]. The concept of the albedo effect is important in terms of climate change. With ice resulting in reflecting more radiation into the atmosphere, the albedo is higher which means that ice remains cold [90]. Whilst, lower water surface albedo increases the water surface temperatures which causes the ice in areas such as the Arctic to melt [89]. Warmer water temperatures increase the water vapour which is one of the most important greenhouse gas [89]. This continuous positive feedback mechanism results in

accelerated climate change [89], [90].

2.5.3 Fresnel's Effect

To understand the behaviour of the reflectance and transmission coefficient at a different angle of incidence, Figure 2.10 shows the s and p polarisation coefficients of Fresnel's effective smooth water surface at various angles of incidence. The coefficients are determined at a wavelength of 500 nm, a water temperature of 20°C and a standard state air temperature of 25°C. The transmission coefficients of the s and p polarisation are shown with a green (T_s) and red (T_p) curve, respectively. While the reflection coefficient of the s and p polarisation is shown with a blue (R_s) and orange (R_p) curve, respectively. It is evident that for incidence angle less than 70°, the largest amount of the incoming radiation is transmitted into the water surface than reflected off the water surface. However, the radiation experiences maximum reflection as the angle of incident reaches 90°. Such a condition in optics defines the grazing incidence. Grazing incidence is reached when the Sun's position is above the horizon, i.e. at sunrise and sunset.

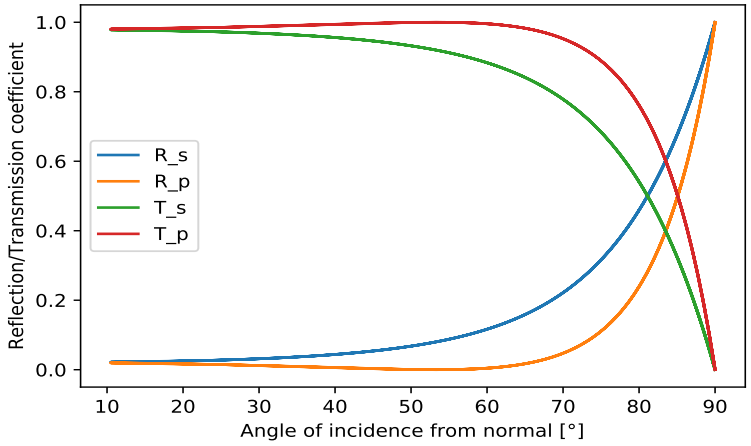

Figure 2.10: Transmission and reflection coefficients of still water surface [21].

2.6 Refractive Index

The propagation of light is described as the manner in which the electromagnetic waves transfer its energy from one point to another [61]. The behaviour of light propagation from one medium to another medium greatly depends on the different wavelengths that light travels with [91]. In 1807, through Thomas Young's continuous efforts of expertizing his knowledge on the wave theory, he established a very important optical property and later coined the term "index

of refraction" [92]. He illustrated that mediums in which light can propagate through will have an index of refraction, and the value of indices is unique for any given medium. This fundamental physical property is a useful tool to identify a particular type of medium, measure its concentration, or verify its purity. The index of refraction or the refractive index is a dimensionless quantity and is denoted by n [91]. The refractive index is defined as the ratio of the velocity of light, c, in a vacuum to its phase velocity, v, of light in the specific medium [91].

The refractive index formula is expressed as follows [91]:

$$n = \frac{c}{v}. \tag{2.6.1}$$

The refractive index is dependent on the wavelength and the frequency of the given medium [91]. However, the frequency of light does not ever change as light propagates from one medium to another [64]. Light is measured by its wavelength and frequency and is denoted by λ and f. The unit of measurements of wavelength is m and for frequency is Hz. The wavelength of light is defined as the distance between the successive crests or troughs of an electromagnetic waveform [48]. The wavelength of light is inversely proportional to the frequency of light, whereby the frequency is described as the number of wave cycles per second [48]. The higher the wavelength, the shorter the frequency of the given electromagnetic wave [48].

The formula for the wavelength is given as [48]:

$$\lambda = \frac{c}{f}. \tag{2.6.2}$$

Therefore, the refractive index can now be expressed as:

$$n = \frac{\lambda_0}{\lambda} = \frac{c/f}{v/f}. \tag{2.6.3}$$

Whereby, λ_0 and λ refers to the wavelength in a vacuum and the specific medium, respectively. The frequency, f, remains unchanged as light travels from the vacuum and the specific medium [64]. Obtaining the values of the refractive indices of the air and the water is critical to incorporate in Snell's law while determining the refraction of the propagated incident ray on the water surface.

2.6.1 Measurement method for Refractive Index

Typically, the most suitable technique used to measure the index of refraction of a given medium is by using a measuring instrument known as a refractometer [47], [93]. Refractometers measure the angle of refraction, and the recorded

refraction angles are then correlated by the refractometers to obtain the value for the refractive indices for the specified medium [47], [93]. The index of refraction can be acquired for solids, liquids or gasses.

There are two methods, a direct and an indirect method, which can be used to obtain the measured values of the refractive index of air. Firstly, the direct method consists of a computational process in which the refractive index of air can be determined by a direct comparison between the optical difference of the air cavity and the vacuum cavity of same-length with the measured value of the refractive indices obtained by the refractometer or through laser interference technology [94], [95], [96]. This direct method reports a measurement accuracy of 10^{-8}. However, this particular strategy requires an interferometric device and a pre-evacuated airtight sealed chamber which is used as a vacuum [94]. This experimental process of measuring the refractive index of air is very complex requiring a very high vacuum chamber which may deform at the atmospheric pressure [97]. Deformation of the vacuum introduces errors, therefore this direct method is seldom used in the engineering process to determine the measured refractive index of air [97].

The indirect method basically consists of conducting direct measurements of various air composition parameters such as atmospheric pressure, humidity and the ambient temperature which are measured using specific sensors [97]. By manipulating such parameters, a formula is derived for calculating the values for the refractive index of air [97]. However, sensors often contribute to delays in measurements which are in fact prone to maximize errors producing a lower measurement accuracy [97]. And also the computed refractive index value from the measured parameters are not the real-time values. Therefore, minimizing the measurement accuracy to up to 10^{-7} or even 10^{-6} if measurement systems are susceptible to errors [97]. The indirect methodology so far remains the most convenient and easier approach of measuring the refractive index of air in comparison to the direct method which involves a complex design approach.

There are various methods which can be used to determine the refractive index of water. A fibre optic technique which uses a fibre optic Fresnel ratio meter can be used for measurements of the refractive indices of various liquids [98]. A pulsed laser diode can also be used to measure the refractive index of water [99]. Initially, an estimate of the light speed in air is obtained and then by measuring the time of flight of a pulsed laser beam, the light speed in water is measured to obtain an estimate of the water refractive index [99]. In the absence of measured refractive index of air and water, the indices are theoretically estimated using the Edlén's and Lorentz-Lorens equation, respectively.

2.6.2 Index of Refraction of Air

Standard air, that is, dry air is defined to be having an absolute pressure of exactly 1 atm which is 101.325 kPa and at a temperature of of 15 $^{\circ}C$ and with 450 ppm of CO_2 content [100]. The index of refraction of air n_{air} is described as the ratio of the wavelength in vacuum λ_{vac} relative to the wavelength of the electromagnetic radiation in air λ_{air} [101].

The index of refraction of air is defined as [101]:

$$n_{air} = \frac{\lambda_{vac}}{\lambda_{air}}. \tag{2.6.4}$$

The refractive index of air is calculated using the modified Edlén's equation which is expressed as [100]:

$$(n_{air} - 1) \times 10^8 = 8342.54 + 2406147(130 - \sigma^2)^{-1} + 15998(38.9 - \sigma^2)^{-1}. \tag{2.6.5}$$

The modified Edlén's equation is expressed as a function of the wavelength in vacuum λ_{vac}. Whereby, σ is specified in the units of μm and given as a fraction of the reciprocal of the wavelength ranging between 200 nm and 1100 nm as follows [100]:

$$\sigma = \frac{1}{\lambda_{vac}}. \tag{2.6.6}$$

In order to introduce a variation of temperature and pressure in the refractive index of air, the modified Edlén's equation is manipulated such that the acquired value of $(n_{air} - 1)$ is multiplied by the following expression [101]:

$$n_{air}(T, p) = (n_{air} - 1)\left(\frac{p[1 + p(60.1 - 0.972T) \times 10^{-10}]}{96095.43(1 + 0.003661T)}\right) + 1. \tag{2.6.7}$$

Whereby, the temperature T ranges from 0 $^{\circ}C$ to 100 $^{\circ}C$ and given in unit of $^{\circ}C$, and the pressure p at standard pressure of 1 atm given in unit of Pa.

2.6.3 Index of Refraction of Water

The Lorentz-Lorenz relation defines the term 'molar refraction' or molecular refractivity [102]. The Lorentz-Lorenz formula relates the index of refraction of a given substance which is in the state of a gaseous or a liquid phase to its polarizability [102]. The index of refraction of liquid water n_{water} is calculated at atmospheric conditions and relative to a vacuum. Therefore, the Lorentz-Lorenz relation is used as a foundation to precisely approximate the index of refraction of liquid water. The relation of the refractive index of water is derived at atmospheric pressure and at various temperatures, wavelengths

and densities.

The Lorentz-Lorenz function is denoted by LL and is defined as [102]:

$$LL = \frac{n_{water}^2 - 1}{(n_{water}^2 + 2)\rho_m}. \tag{2.6.8}$$

Whereby, rho_m is the density of the liquid water in moles per unit volume. Furthermore, to relate the refractive index of water to the molecular polarizability α at various optical frequencies, the Lorentz-Lorenz equation is simplified as [102]:

$$\frac{n_{water}^2 - 1}{(n_{water}^2 + 2)\rho_m} = \frac{N_A \alpha}{3\epsilon_0}. \tag{2.6.9}$$

Where N_A is Avogadro's number and ϵ_0 the vacuum permittivity.

The Lorentz-Lorenz function is dependent on the wavelength by the dispersion relation [102]. Therefore, the dispersion relation is incorporated to relate the wavelength dependency on the molar refraction as [102]:

$$\frac{n_{water}^2 - 1}{(n_{water}^2 + 2)\rho_m} = a_0 + \sum_i \frac{a_i}{\lambda^2 - \lambda_i^2}. \tag{2.6.10}$$

Whereby, a_i are constants relating to the resonance strength and λ_i the wavelength contributing to the i^{th} resonance. The Lorentz-Lorenz equation is effective in the application for all resonances, however, the IR and UV of the electromagnetic radiation spectrum have a significant effect on the refractive index [102]. IR and UV light are two of the nearest electromagnetic radiation in the visible light spectrum which is of interest. Therefore, only the two-wavelength resonances, λ_{IR} and λ_{UV}, are included in the formulation and is given as [102]:

$$\frac{n_{water}^2 - 1}{(n_{water}^2 + 2)\rho_m} = a_0 + \frac{a_{IR}}{\lambda^2 - \lambda_{IR}^2} + \frac{a_{UV}}{\lambda^2 - \lambda_{UV}^2}. \tag{2.6.11}$$

With least-square adjustments, the value of the resonance strength constants a_0, a_{IR} and a_{UV} are obtained [102]. The wavelength of the resonances λ_{IR} and λ_{UV} are selectively chosen to provide a more accurate refractive index in the visible light spectrum [102].

Incorporating the dependency of the relevant wavelength, temperature, density and pressure, the Lorentz-Lorenz function of liquid water is expanded as [102]:

$$\frac{n_{water}^2 - 1}{(n_{water}^2 + 2)\rho^*} = a_0 + a_1\rho^* + a_2 T^* + a_3 T^* \lambda^{*2} + \frac{a_4}{\lambda^{*2}} + \frac{a_5}{\lambda^{*2} - \lambda_{UV}^{*2}} + \frac{a_6}{\lambda^{*2} - \lambda_{IR}^{*2}} + a_7 \rho^{*2}. \tag{2.6.12}$$

With ρ the density, T the absolute temperature and λ the wavelength. The subscript * denotes the variation in parameters which are defined as the ratio of the actual value divided by the initial value. The relation is expressed as [102]:

$$\rho^* = \frac{\rho}{\rho_0},$$

$$\lambda^* = \frac{\lambda}{\lambda_0},$$

$$T^* = \frac{T}{T_0}.$$

With the initial values given as [102]:

$$\rho_0 = 1000 kg.m^{-3},$$

$$\lambda_0 = 0.589 \mu m,$$

$$T_0 = 273.15 K.$$

The three independent variables, density, wavelength and temperature ranges as follows:

$$200 \leq \lambda \leq 1100 nm,$$

$$958.4 \leq \rho \leq 999.84 kg.m^{-3},$$

$$0 < T \leq 100^{\circ} C.$$

The coefficients a_0 to a_7 are the resonance strength constants, and λ_{IR} and λ_{UV} are the effective resonances [102]. Table 2.3 presents these coefficients and resonance values are selectively optimized to fit the full range over which the data exist.

Table 2.3: Coefficients of the Lorentz-Lorenz function [21], [102].

Coefficients	Value
a_0	0.243905091
a_1	$9.53518094 \times 10^{-3}$
a_2	$-3.64358110 \times 10^{-3}$
a_3	$2.65666426 \times 10^{-4}$
a_4	$1.59189325 \times 10^{-3}$
a_5	$2.45733798 \times 10^{-3}$
a_6	0.897478251
a_7	$-1.63066183 \times 10^{-2}$
λ^{*IR}	0.2292020
λ^{*UV}	5.432937

2.7 Total Clear-sky Insolation on an Inclined Surface

PV plants are often not instrumented due to various factors of which one of them is mainly because of the financial burden. To circumvent the lack of measurements from a PV plant, models can be applied to estimate the total solar collector insolation. Therefore, in the absence of the total measured insolation on a collector surface, appropriate models are used to reasonably estimate the direct beam, sky diffuse and reflected components.

2.7.1 Direct Beam Radiation

When the solar radiation received from the Sun does not experience scattering in the atmosphere, this is defined as the beam radiation [48]. The incident direct beam radiation I_B, i.e. DNI component, refers to the solar radiation which propagates on a straight line directly perpendicular to the collector surface [48]. The beam radiation on the Plane of Array (POA) of a collector surface, I_{BC}, is approximated as a function of the solar incidence angle θ as [48]:

$$I_{BC} = I_B \times \cos\theta. \tag{2.7.1}$$

Whereby, θ is the angle between a line perpendicular to the collecting surface and the incident beam. The incidence angle is expressed as a function of the solar azimuth angle ϕ_S, the solar altitude angle β, i.e. the elevation angle of the Sun at any given time in a day, and the collector orientation which is defined by $\sum$ the tilt angle of the solar collector and the collector azimuth angle ϕ_C [48]. The convention of the collector azimuth angle is denoted positive in the

southeast and negative in the southwest direction. The angle of incidence is expressed as [48]:

$$\cos\theta = (cos\beta \times \cos(\phi_S - \phi_C) \times \sin\sum) + (\sin\beta \times \cos\sum). \tag{2.7.2}$$

However, to ensure that the solar panels capture the greatest possible amount of solar radiation possible during the day, the PV modules are faced towards the terrestrial equator, i.e. North and South in the Southern and the Northern Hemisphere, respectively. In this study, the solar panels are faced directly true North. Therefore, the collector azimuth angle is equated to zero, i.e. neglected. The solar azimuth angle is approximated with δ the solar declination angle and H the hour angle as [48]:

$$\sin\phi_S = \frac{\cos\delta \times \sin H}{\cos\beta}. \tag{2.7.3}$$

Since the inverse trigonometric function, arcsine is only defined for the domain $[-1, 1]$ and the range $[-90°, 90°]$, it introduces ambiguity for any other ranges. Therefore, a test check is applied to determine whether the solar azimuth angle is less than or greater than 90°. The test check is: if $\cos H \geq \frac{\tan\delta}{\tan L}$, then $\mid \phi_S \mid \leq 90°$; otherwise $\mid \phi_S \mid \geq 90°$ [48].

The convention of the hour angle is denoted positive before solar noon and negative after solar noon. In the 24 hours of solar time, the Earth rotates 360° which equates to 15° per hour, thus approximating the hour angle as [48]:

$$H = \frac{15°}{hour} \times \text{hours before solar noon.} \tag{2.7.4}$$

The solar declination angle ranges between $-23.45°$ and 23.45° and is approximated as [48]:

$$\delta = 23.45 \times \sin[\frac{360}{365} \times (n - 81)]. \tag{2.7.5}$$

To maximize the average production throughout a full year, a fixed-tilt system is used in this study. Minutely values of the tilt angle, $\sum$, relevant to the horizon for the year 2018 are calculated and averaged to find the optimal tilt angle $\sum_{optimal}$. For year-round loads, the tilt angle of a fixed-tilt system should be equal to the latitude of the relevant location. The optimal tilt angle is found to be close to the latitude angle L of the location of interest. The parameters of the location used in this study are [103]:

$$\sum_{optimal} = 33.508510°,$$

$$Locallatitude = -33.927905°,$$

$$Locallongitude = 18.865266°,$$

$$Localtimemeridian = 30.0°.$$

The solar altitude angle is approximated as a function of the latitude angle of the relevant location, the solar declination angle, and the hour angle as follows [48]:

$$\sin\beta = (\cos L \times cos\delta \times \cos H) + (\sin \times \sin\delta). \tag{2.7.6}$$

Figure 2.11 illustrates the collector surface facing true North at an optimal tilt angle. The type of solar collector used in this study is undefined. The solar panel is assumed to be placed on a floating platform of a smooth water surface, i.e. still water surface.

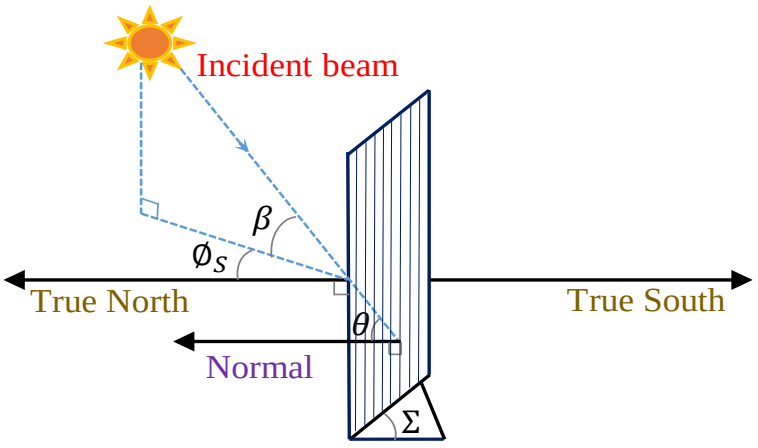

Figure 2.11: The fixed tilt collector surface and its direct beam [103].

2.7.2 Diffuse Radiation

When there are atmospheric particles and moisture present in the air, a portion of the radiation from the Sun experiences single or multiple dispersion [48]. This dispersed ray of light is defined as the sky diffuse radiation. Due to the multiple dispersion, the diffuse radiation is very complex for accurate estimations. The models that can be applied to estimate the diffuse radiation striking the collector surface can be classified as anisotropic and isotropic sky models [48]. The anisotropic models assume that the sky diffuse radiation is direction-dependent and non-uniform [48]. Whereby, the isotropic model presumes that the diffuse sky radiation is uniformly distributed over the entire sky dome [48]. Therefore, the isotropic radiation is direction independent and has an equal intensity distribution over the sky dome irrespective of the different angular direction of propagation.

To accurately estimate the diffuse radiation received on the collector surface, an initial assumption is made such that the sky is isotropic. On a horizontal surface, all the diffuse sky radiation is equivalently received on the horizontally oriented collector surface regardless of the Sun's position in the sky [48]. However, on a tilted module, only a fraction of the diffuse sky radiation which is proportional to the hemispherical sky strikes the collector surface [48]. The horizontal diffuse sky radiation I_{DH} is approximated using the Ineichen and Perez clear-sky model available in PVLIB-Python.

The diffuse sky radiation I_{DC} on the collector surface is approximated at an optimal tilt angle as [48]:

$$I_{DC} = I_{DH} \times [\frac{1 + \cos \sum}{2}]. \tag{2.7.7}$$

Figure 2.12 illustrates the isotropic distribution of the sky diffuse radiation on a tilted collector surface.

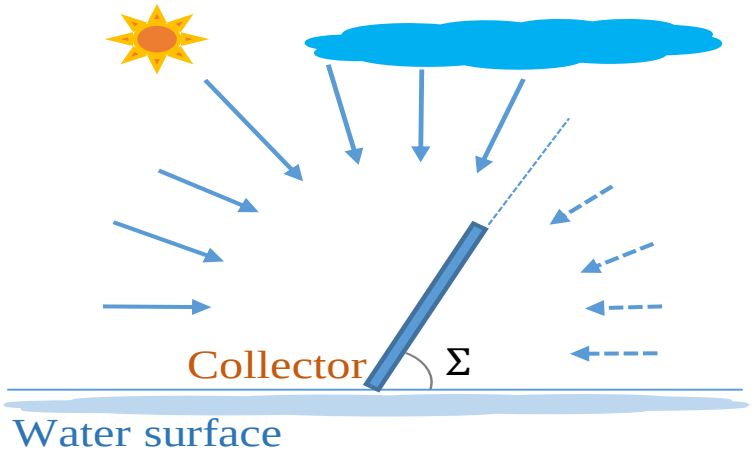

Figure 2.12: The isotropic sky diffuse radiation [103].

2.7.3 Reflected Radiation

The reflected radiation is the radiation which is reflected from the specific surface, which in this study is the water surface or the floating platform in front of the solar panel. In order to accurately approximate the clear-sky reflected radiation, an initial assumption is made such that a large, horizontal surface area is available in front of the solar collector. The reflected radiation is also assumed to be isotropic such that it bounces off the water surface or the floating platform uniformly with equal intensities in all direction. These assumptions only remain valid for water surfaces that are still.

The total horizontal radiation I_{GH} is estimated using the Ineichen and Perez clear-sky model available in PVLIB-Python. The reflected radiation I_{RC} striking the collector surface is approximated as a function of the water surface albedo ρ_{water}, the tilt angle of the panel, and the product of the total horizontal radiation as [48]:

$$I_{RC} = \rho_{water} \times I_{GH} \times [\frac{1 - \cos \sum}{2}]. \tag{2.7.8}$$

Whereby, $I_{GH} = I_{BH} + I_{DH}$.

Figure 2.13 illustrates the isotropic distribution of the reflected water surface radiation together with the horizontal beam I_{BH} and the horizontal sky diffuse I_{DH} components.

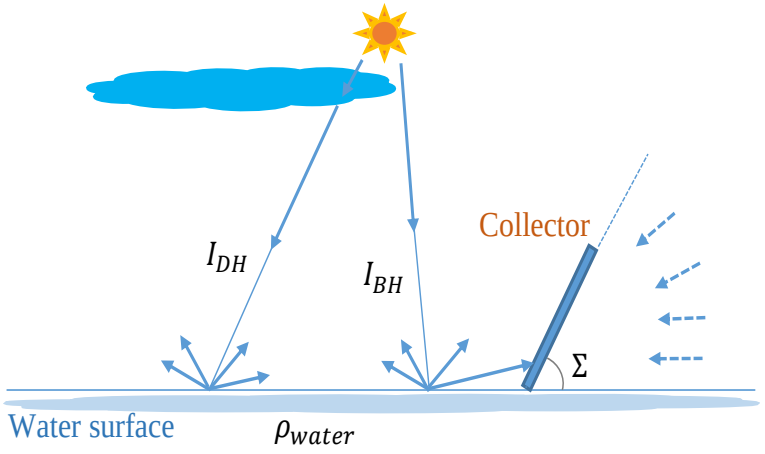

Figure 2.13: The reflected water surface radiation [103].

2.8 Summary

In this chapter, a brief introduction to the theoretical background of solar PV and the wave theory of light is provided. The single diode equivalent circuit of a PV device is provided and how the solar irradiation and temperature affects the I-V characteristics. Variation of solar irradiance mainly affects short-circuit current and the variation of the cell temperature affects the open-circuit voltage. A brief overview of the SERIS FPV testbed is provided together with the measured albedo and the investigated U-values for the different floating PV structures. The measured albedo of water at the SERIS FPV testbeds is found to be between 5 % and 7 %. The investigated heat transfer coefficient, U-value, at the SERIS FPV testbed show that a 'free-standing' floating structure type has higher U-values compared to other floating structure types. The higher U-values correspond to a better cooling effect, and thus a lower module

temperature which effectively contributes to better electrical performance and vice versa. Furthermore, a brief introduction to optics at an air-water interface is discussed together with the albedo effect of water and Fresnel's effect. The theoretical background of the wave theory of light is implemented in the following chapter to investigate the water surface albedo. The mathematical evaluation of the refractive index of air and water is formulated and is implemented in the following chapter. Finally, appropriate models of the direct beam radiation, sky diffuse radiation and reflected radiation is described. The estimated total clear-sky insolation models are further used in the following chapter to investigate the water surface albedo on the collector insolation and the annual energy yield.

Chapter 3

Albedo Modelling

This chapter provides detailed information about the albedo model and the modelling approximations. A full description of the weather station and its instrumentation set-up from which the solar radiometric data is retrieved is also provided. The procedure for data acquisition and filtering the datasets is also described.

The clear sky models which are used to predict the clear sky irradiance are provided with a detailed explanation. The result of the refractive index of air and water is also provided. The result of the albedo model is as well given. Subsequently, the albedo effect on the solstices and equinoxes is illustrated together with the effect of the water surface albedo on the collector insolation, and the annual energy yield.

All mathematical calculations and measured data are analysed using Python with Pandas and matplotlib libraries through an open-source Jupyter Notebook for interactive computing and data visualization. All mathematical calculations of the measured solar radiometric data are performed using the open-access simulating tool, PVLIB Python [104], specifically the 0.7.1 version [105].

3.1 Albedo model

An appropriate selection of the foundation for the water surface albedo model is critical. An initial assumption is made such that the water surface is assumed to be smooth. The reflected radiation from the smooth water surface is estimated with a combination of the Fresnel's law and the Snell's law. Fresnel's law, which is also known as the law of reflection and transmission, describes the reflection and transmission of beams of light at the interface between two media [62], [106]. In 1820, Augustin-Jean Fresnel formulated the law of reflection as the angle at which the wave of light ray that is incident on the surface

is equal to the angle at which it is reflected [62].

Fresnel's equation is expressed as [62]:

$$\theta_1 = \theta_2. \tag{3.1.1}$$

Whereby, θ_1 is the angle of incidence and θ_2 is the angle of reflection. The angle of incidence is the angle between the incoming ray of light striking a surface and a line drawn perpendicular at the point of incidence to that surface. The angle of reflection is the angle between the reflected ray and the normal line drawn perpendicular to the reflecting surface at the point of reflection [106].

Fresnel's law only remains valid to use for geometric optics which describes the mechanism of specular reflection [106]. Surfaces that exhibit perfect specular reflection reproduce mirror-like reflection of the light ray [106].

The reflectance off the smooth water surface is calculated using the Fresnel's formula. While, the angle of refraction, ϕ_2, is calculated using the Snell's formula [63]. The Snell's law, which is also known as the law of refraction, defines the relationship between the two angles, angle of incidence and the angle of refraction when light propagates through the interface between two different optical media [63]. Snell's law shows that the ratio of the sine of the angle of incidence and the angle of refraction is equal to the ratio of the refractive index of the media at its interface [63].

Manipulating the law of refraction, the angle of refraction is calculated as [47], [63], [106]:

$$\phi_2 = \arcsin \frac{n_1 \times \sin \theta_1}{n_2}. \tag{3.1.2}$$

With n_1 the refractive index of air and n_2 the refractive index of the water medium.

Figure 3.1 shows the interface between the water surface and air, together with the different corresponding angles and rays. The refractive index of air, n_1, and the refractive index of water, n_2, is calculated as previously explained in Chapter 2, Subsections 2.6.2 and 2.6.3, respectively.

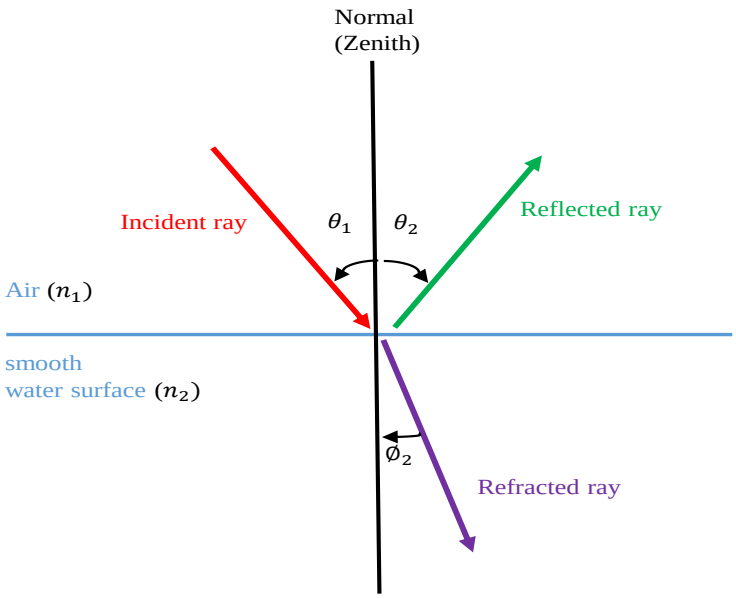

Figure 3.1: Air and water interface [21].

3.1.1 Modelling approximation

The water surface albedo model is formulated based on the assumption that the incoming radiation striking the water surface is the DNI component [21]. This assumption is relevant as the DNI component is most prominent for clear sky days, therefore, providing more accurate forecasting of the albedo variation. When the DNI component encounters the interface between the air and the water surface, a portion of the incident ray will transmit through the water surface. The transmitted or the refracted ray is then absorbed in the different water layers causing multiple internal refraction. However, the remaining portion of the refracted ray which is not completely absorbed in the water layers will eventually bounce off the water surface and into the atmospheric environment in the form of reflected rays. In this albedo model, only the surface layer of the water is considered for the refraction and reflection of the incident ray. Therefore, ignoring other internal refraction which may add complexity to the model.

The s and p polarised lights as previously described in Chapter 2, subsection 2.4.3.2, have reflection coefficients which can be used to calculate the effective reflectivity. The reflection coefficients, $r_\perp$ and $r_\parallel$, of the s and p polarised lights, respectively, are calculated as a function of the incident angle, θ_i, and angle of transmission, θ_t, as [21], [68], [107]:

$$r_\parallel = \frac{\tan^2(\theta_i - \theta_t)}{\tan^2(\theta_i + \theta_t)}, \tag{3.1.3}$$

$$r_{\perp} = \frac{\sin^2(\theta_i - \theta_t)}{\sin^2(\theta_i + \theta_t)}. \tag{3.1.4}$$

The effective reflectivity is calculated as the average of the two reflection coefficients. The total reflection coefficient, R_u, of the unpolarised light is expressed as [21], [68], [71]:

$$R_u = \frac{r_{\parallel} + r_{\perp}}{2}. \tag{3.1.5}$$

Furthermore, the effective transmission coefficient, T_u, of the unpolarised light is expressed as [21], [68], [71]:

$$T_u = 1 - R_u. \tag{3.1.6}$$

3.2 Sonbesie Weather Station

The Southern African Universities Radiometric Network (SAURAN) has been established with the aim of providing freely available ground-based solar radiometric data [108]. The SAURAN network is an initiative established in 2015 by two research centres in South Africa namely the Centre for Renewable and Sustainable Energy Studies (CRSES) at the University of Stellenbosch, and the Group for Solar Energy Thermodynamics (GSET) at the University of KwaZulu-Natal [108]. Currently, SAURAN has 22 active stations which are located across the Southern African region, including Botswana, South Africa and Namibia [21], [109]. The measured solar data used in this study is acquired from one of the SAURANs solar monitoring station named Sonbesie. The Sonbesie solar measurement station is situated at the rooftop of the civil engineering building of Stellenbosch University. The Sonbesie station provides high-resolution solar data in the intervals of 1 minute, hourly and daily time averages.

The total system installation at the Sonbesie station consists of a data logger which is connected to a Kipp and Zonen Solys 2 dual-axis sun tracker that houses one pyrheliometer, one shaded and an unshaded pyranometer and one UVS-AB-T radiometer; together with a shadow ring, but no rainfall sensor as shown in Figure 3.2.

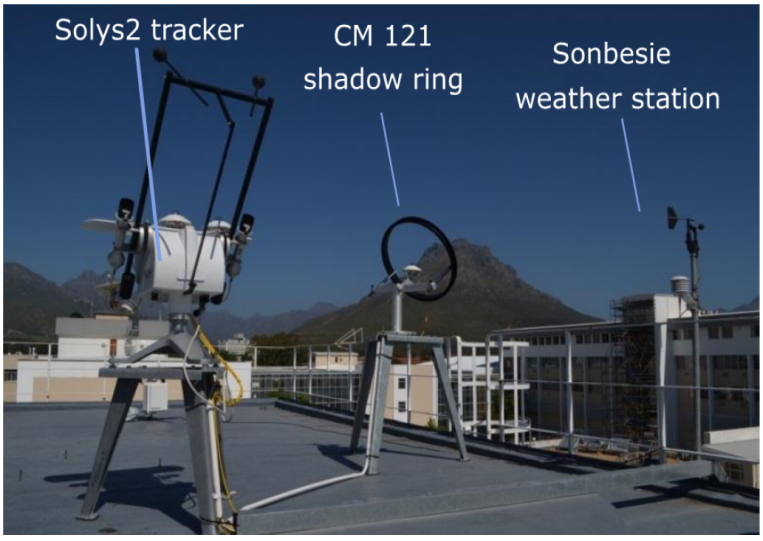

Figure 3.2: Sonbesie station and its instrumentation [109], [21].

3.2.1 Data Collection

At the Sonbesie station, numerous solar radiation data are measured such as DNI, GHI, DHI, long wave ultraviolet A (UVA) and short wave ultraviolet B (UVB) irradiance; and also other weather data such as relative humidity, barometric pressure, air temperature, wind speed and wind direction. From the measured data, only the solar data namely GHI, DNI, and DHI are used in this research work. The measured data from the weather station is freely accessible at [110] which provides the option to select the range of date for downloading the data as a .zip-archive containing files with comma-separated values (CSV). The acquired radiometric data are time-averaged over 1-minute intervals for every day of the year for the period 1^{st} January 2013 to 31^{st} December 2019.

3.2.2 Data Cleaning

Most data sets in the real world, which are collected, may contain missing data. Missing data are simply values which may not be available due to various factors. Missing data fields occurs during the logging process whereby no data values are stored of which some data entries may contain errors. Incomplete or missing data values are a common occurrence in the real world data acquisition process. Factors which often results in uncertainty in the measured data are due to calibration errors, data averaging variations, bad weather conditions, quality of the instrument and its adequate maintenance. In statistical evaluation, missing data values are undesirable and problematic as it may have a significant influence on the conclusion, creating bias estimations, and may

also reduce the statistical power leading to invalid inferences [111].

There are numerous techniques for handling missing data [112]. However, the technique in which the missing data is handled is different for every given application. Therefore, to avoid uncertainties in this study, the measured solar radiation data from the Sonbesie station are thoroughly evaluated for every timeframe, identifying NaN values and missing data values. Minutely datasets timestamps of the rows for the years, 2013 to 2018, with at least 1 NaN value are dropped. Table 3.1 presents the number of missing values for different years. It is evident that most of the years contain none or very few NaN values, except for the year 2015 which results in eliminating 17 hours of data from the entire year which may not introduce a large error.

Table 3.1: Missing values for the various years.

Year	**Number of missing values**
2013	0
2014	28
2015	1017
2016	17
2017	0
2018	4

To understand the type of solar data used in this study, the solar radiometric data are illustrated for the different types of days together with the annual variation of the measured solar data. Figure 3.3 shows the annual variation of the GHI for the year 2018.

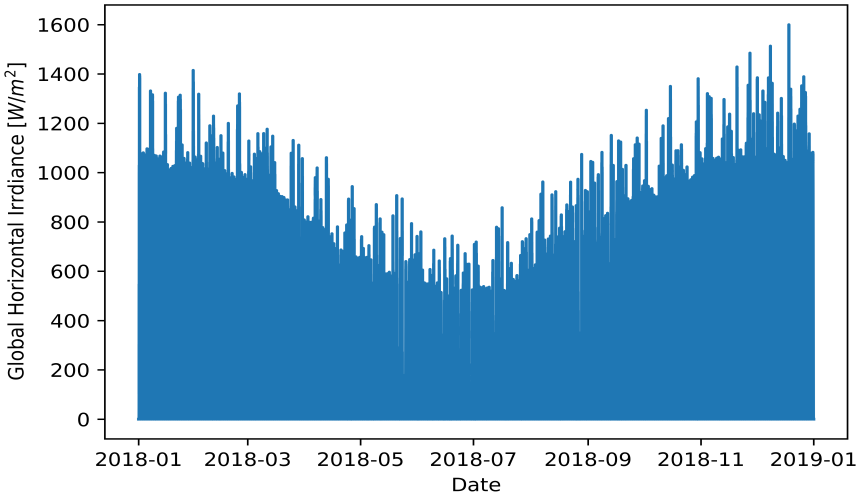

Figure 3.3: Annual GHI for 2018 [21].

The solar radiometric data includes different types of days such as clear-sky, overcast (cloudy), intermittent clear-sky and overcast days. Figure 3.4 illustrates the DNI components for the different types of days measured in the year 2018.

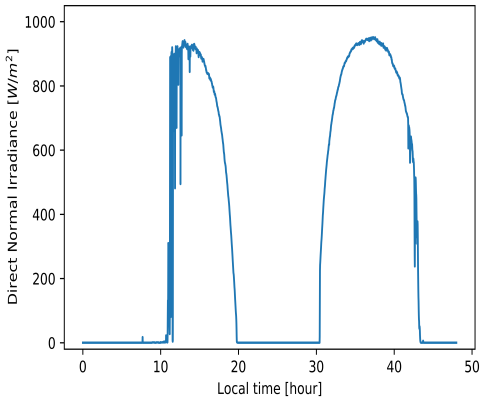

(a) An intermittent clear-sky and a clear-sky day.

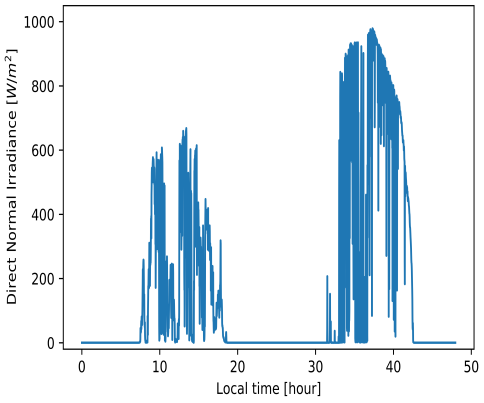

(b) An overcast and an intermittent overcast day.

Figure 3.4: Illustration of different types of days [21].

After analysing and cleaning the measured solar radiometric data, clear-sky days for each of the seasons, i.e. summer, spring, autumn and winter are identified to evaluate the effect of the water surface albedo model on the reflected irradiance.

3.3 Clear Sky Model

In the absence of measured clear sky irradiance, relevant clear sky models are identified to predict the clear sky irradiance. The clear sky models are the foundation in developing the water surface albedo model. The two clear sky models namely Ineichen and Perez [113] and the Simplified Solis [114], which are available in PVLIB-Python, are implemented to estimate the solar radiation, i.e. GHI, DNI and DHI. The measured irradiance for each of the identified clear-sky days in the four seasons is compared to the predicted clear-sky days of solar radiation. To validate the performance of the model accuracy, relative performance matrices, performance matrices i.e. MBE and RMSE are assessed.

3.3.1 Simplified Solis

The clear-sky Simplified Solis model estimates the clear sky GHI, DNI, and DHI. These estimated irradiances are parameterized in relation to the Aerosol Optical Depth (AOD) and the precipitable water. AOD measures the extinction of the solar beam due to particles that are present in the atmosphere, such as dust, haze and pollution [115]. These atmospheric particles can block sunlight by absorbing or by scattering light [115]. An AOD value indicates how much of the direct radiation is prevented from reaching the Earth's surface by the atmospheric aerosol particles [115]. The AOD value is a dimensionless quantitative estimate that is related to the amount of aerosol in the vertical column of the atmosphere over the observation location [115]. According to PVLIB-Python, the proposed AOD values should range between 0 and 0.45 [116]. The AOD value for each of the seasons is adjusted for accurate approximation of the clear sky days. For the given location of the Sonbesie station, the AOD value ranges between 0.049 and 0.117 as shown in Table 3.2. The presented AOD values for the different season in Table 3.2 corresponds to the reported AOD values in Cape Town [117].

Precipitable water is a measure of the atmospheric moisture that indicates the amount of water which may be potentially available in the atmosphere for precipitation. According to PVLIB-Python, the values of the precipitable water could range between 0.2 *cm* and 10 *cm* [116]. To show the correlation between the AOD and the precipitable water, Ranjan et al. reported that the water vapour increases with an increase in AOD [118]. However, implementing this clear-sky model in PVLIB-Python, the python tool uses a default value of 1.0 *cm* with the assumption that all the water vapour in a vertical column of air is precipitated into liquid water [119].

3.3.2 Ineichen and Perez

The clear-sky Ineichen and Perez model estimate the clear sky GHI, DNI, and DHI. These estimated irradiances are parameterised in relation to the Linke turbidity factor. The Linke turbidity factor is a dimensionless estimate which indicates the measure of the atmospheric turbidity and the attenuation of the direct beam solar radiation [120]. The Linke turbidity factor defines the optical thickness of the atmosphere which results from the scattering and absorption by the aerosol particles and absorption by the water vapour relative to a clean and dry atmosphere [120].

The Linke turbidity factor is a very convenient approximation which is used to model the atmospheric absorption together with the scattering of the solar radiation under clear skies [120], [121]. The Linke turbidity factor for each of the seasons is adjusted for accurate approximation of the clear sky days. For the given location of the Sonbesie station, the Linke turbidity factor ranges between 0.635 and 1.425 as shown in Table 3.2. The Linke turbidity factor increases as the attenuation of the solar radiation increases by the clear sky atmosphere [120]. The presented Linke turbidity factor values for the different season in Table 3.2 corresponds to the reported Linke turbidity factor values in Cape Town [122].

Table 3.2: AOD and Linke turbidity for each season [21].

Season	**AOD**	**Linke turbidity**
Autumn	0.049	1.102
Winter	0.056	0.635
Spring	0.069	1.425
Summer	0.117	0.848

3.3.3 Clear Sky Model Verification

To evaluate which clear-sky model best fits the measured solar radiation, the performance metrics are evaluated for the two clear-sky models for each of the seasons. The measured solar radiation for each of the clear sky days of the seasons are compared to the estimated clear-sky solar radiation using the following two performance metrics [123]:

$$MBE = \frac{1}{N}\sum_{i=1}^{N}(\hat{y} - y_m), \tag{3.3.1}$$

$$RMSE = \sqrt{\frac{1}{N}\sum_{i=1}^{N}(\hat{y} - y_m)^2}\,. \tag{3.3.2}$$

With N the number of samples, $\hat{y}$ the predicted value and y_m the measured value.

Table 3.3 presents the performance metrics for the two clear-sky models which are calculated using the GHI component for each of the seasons. The two clear-sky models error differences are dependent on the AOD and Linke turbidity factor.

Metrics $[W/m^2]$		
Season	**RMSE**	**MBE**
Autumn	3.85	-0.19
Winter	4.45	0.02
Spring	5.86	-0.14
Summer	7.18	-0.23

(a) Ineichen-Perez performance [21].

Metrics $[W/m^2]$		
Season	**RMSE**	**MBE**
Autumn	3.84	0.24
Winter	6.06	0.60
Spring	5.56	0.35
Summer	9.18	0.15

(b) Simplified Solis performance [21].

Table 3.3: Performance metrics of the clear-sky models.

The errors for both clear-sky models are within the acceptable range [124]. Thus, evident that both the clear-sky models attribute an accurate estimate of the solar radiation. However, in this study, the Ineichen-Perez clear-sky model is used for predicting the solar radiation. Figure 3.5 illustrates the measured and estimated GHI component of the two clear sky models on a clear sky day in summer.

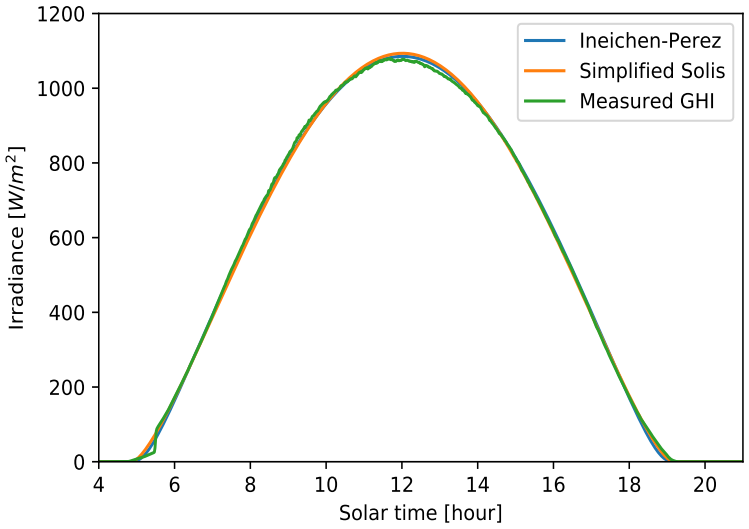

Figure 3.5: Measured and estimated GHI [21].

3.4 Clear-Sky Collector Insolation Illustration

To evaluate the effect of the water surface albedo model on the collector insolation, the measured solar radiometric data for the year 2018 are used. The effect of the water surface albedo model on the total collector insolation is evaluated for each of the solstices and equinox's clear-sky days in the annual data. The total collector insolation constitutes of the 3 components namely the direct beam radiation, I_{BC}, the diffuse sky radiation I_{DC}, and the reflected radiation I_{RC}. Figure 3.6 presents the collector insolation for the equinoxes and solstices. On a summer solstice clear sky day, the DNI from the sun only strikes the collector surface when the solar azimuth angle is larger than 90° at sunrise and smaller than −90° (or 270°) at sunset. This is clearly evident in Figure 3.6a as the solar collector only gets exposed to the direct beam radiation when the sun's position is above the horizon for the range of the solar azimuth angle between 90° and 270°. Therefore, this effectively demonstrates the accuracy of the collector insolation model.

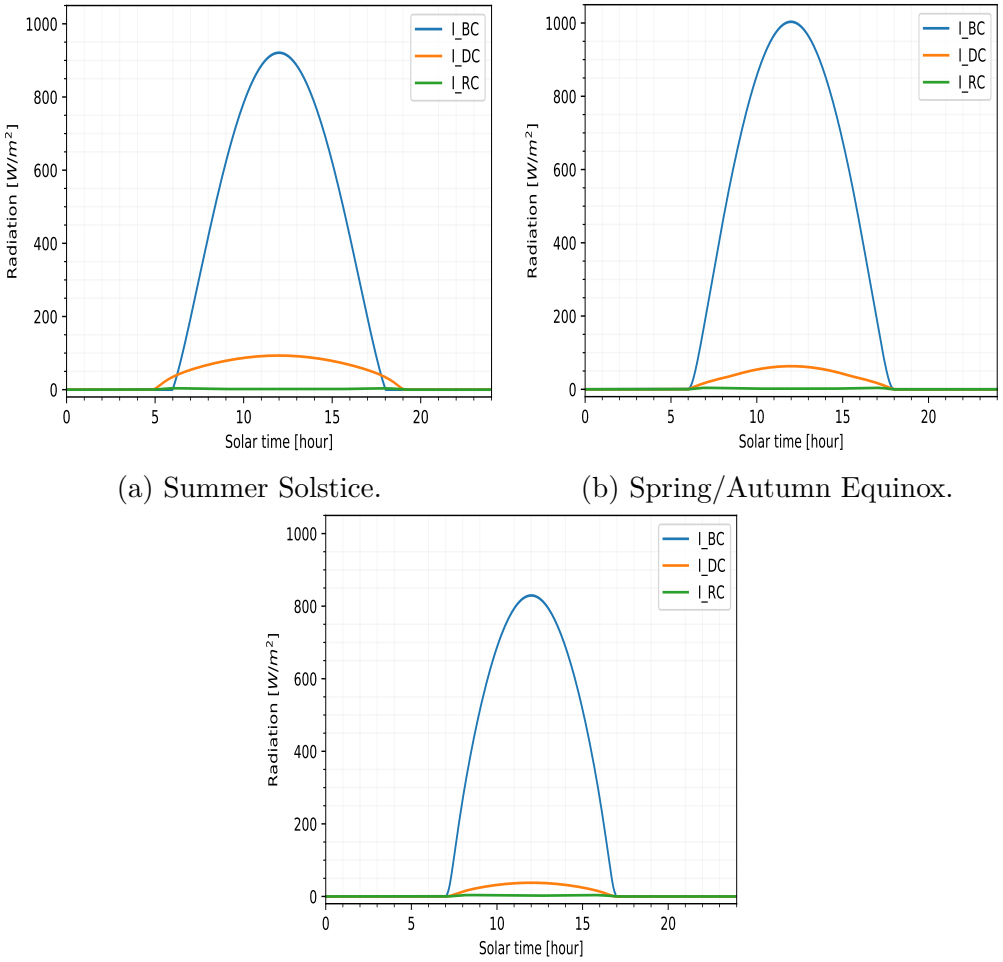

(a) Summer Solstice.

(b) Spring/Autumn Equinox.

(c) Winter Solstice.

Figure 3.6: Total insolation on an inclined collector surface [103].

3.5 Refractice Index

3.5.1 Index of Refraction of Air

Figure 3.7 presents the variation in the index of refraction of standard air ($n_{air} - 1$) with respect to the wavelength for temperature ranges from 10 $°C$ to 100 $°C$ with a 10 $°C$ intervals. The effective approximation of the refractive index of standard air decreases with an increase in the wavelength and temperature. The effect of the refractive index of air at a temperature of 0 $°C$ is not illustrated on Figure 3.7 as the absolute zero temperature refers to the perfect stillness in the atmosphere which does not exist as anything in the universe or in fact in a laboratory has ever experienced or reached the absolute zero condition. The absolute zero temperature is equal to 0 K on the Kelvin scale, i.e. -273.15 $°C$. Therefore, the thermodynamic behaviour of the

absolute temperature is non-ideal in the real world scenario.

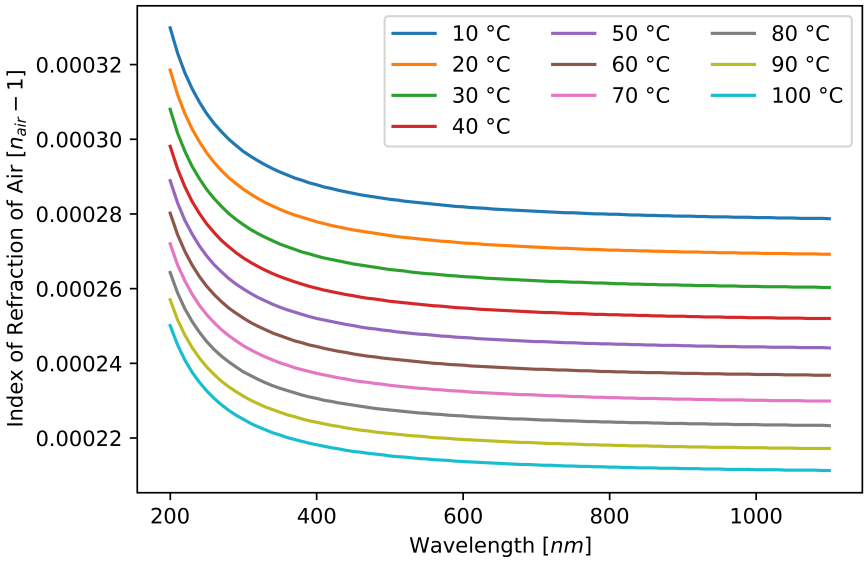

Figure 3.7: Refractive index of standard air relative to the wavelength at various temperatures [21].

Table 3.4 presents the maximum, minimum and the mean values of the index of refraction of air, n_{air}, for the temperature range from 10 $°C$ to 100 $°C$ with a 10 $°C$ interval of the wavelength range from 200 nm to 1100 nm. The maximum value ranges between 1.000250 and 1.000330 and the minimum value ranges between 1.000211 and 1.000279 for the different temperature intervals.

Table 3.4: Maximum, minimum and the average values of the refractive index of air.

Refractive index of air $[n_{air}]$			
Temperature $[°C]$	**Maximum**	**Minimum**	**Mean**
10	1.000330	1.000279	1.000286
20	1.000318	1.000269	1.000276
30	1.000308	1.000260	1.000267
40	1.000298	1.000252	1.000258
50	1.000289	1.000244	1.000250
60	1.000280	1.000237	1.000243
70	1.000272	1.000230	1.000235
80	1.000264	1.000223	1.000229
90	1.000257	1.000217	1.000222
100	1.000250	1.000211	1.000216

Table 3.4 shows that the average value of the refractive index of standard air, n_{air}, is more or less 1.000277 which is typically used for air at STP conditions. Therefore, indicating the accuracy of modified Edlén's equation in approximating the refractive index of standard air in the absence of measured data. The difference in the refractive index of standard air is less than 10^{-3} % for the various temperature ranges. Thus, indicating that the variation in the refractive index of standard air is not largely dependent on the temperature differences but rather the wavelength of the radiation.

3.5.2 Index of Refraction of Water

Figure 3.8 illustrates the effect of temperature variation with an interval of 10 $°C$ on the refractive index of liquid water at different wavelengths. As the wavelength and temperature increases, the index of refraction of water decreases.

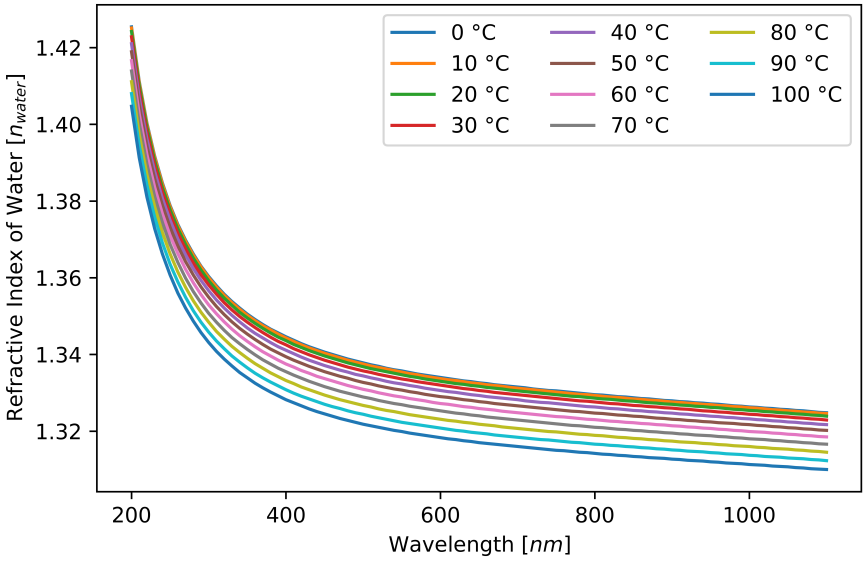

Figure 3.8: Refractive index of liquid water relative to the wavelength at various temperatures [21].

Table 3.5 presents the maximum, minimum and the mean values of the index of refraction of liquid water for the temperature range from 0 $°C$ to 100 $°C$ with a 10 $°C$ interval of the wavelength range from 200 nm to 1100 nm. The maximum value ranges between 1.4047 and 1.4254 and the minimum value ranges between 1.3100 and 1.3248 for the different temperature intervals.

Table 3.5: Maximum, minimum and the average values of the refractive index of water.

Refractive index of liquid water $[n_{water}]$			
Temperature $[°C]$	**Maximum**	**Minimum**	**Mean**
0	1.4254	1.3248	1.3399
10	1.4251	1.3246	1.3396
20	1.4242	1.3239	1.3389
30	1.4228	1.3229	1.3378
40	1.4210	1.3217	1.3365
50	1.4189	1.3202	1.3349
60	1.4166	1.3185	1.3331
70	1.4139	1.3166	1.3310
80	1.4111	1.3145	1.3288
90	1.4080	1.3123	1.3265
100	1.4047	1.3100	1.3239

Table 3.5 shows that the average value of the refractive index of water, n_{water}, is more or less 1.33 which is typically used for a water temperature of 20 $°C$. Therefore, indicating the accuracy of the Lorentz-Lorenz function in approximating the refractive index of water in the absence of measured data. The difference in the refractive index of liquid water is less than 0.3 % for the various temperature ranges. Thus, indicating that the variation in the refractive index of liquid water is not largely dependent on the temperature differences but rather the wavelength of the radiation.

3.6 Water surface albedo model

All analysis in this section is conducted with the albedo modelled at a wavelength of 500 nm, the water temperature of 20$°C$ and a standard state air temperature of 25$°C$.

A common misconception is that floating PV has an increased benefit in energy production due to higher reflection from the water surface. However, the water surface albedo model illustrates that the albedo of water is extremely low. As the summer solstice has the most daylight, it is best to evaluate the albedo variation on this day. Figure 3.9 shows the variation of the water surface albedo throughout a clear summer solstice day and the altitude angle relevant to solar time. It is evident that the default albedo value of 0.2 is a far offset and an unreliable estimate for floating PV modelling. The lowest albedo values are observed during daylight after 8 o'clock and before 16 o'clock with an average

albedo value of 0.0207. The maximum albedo value close to 1.0 is observed during sunrise and sunset, indicating total reflection.

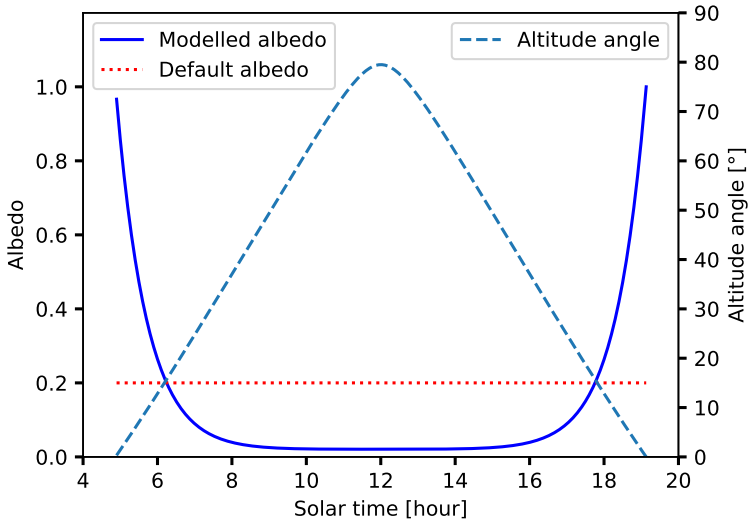

Figure 3.9: Albedo model on the summer solstice [21].

Figure 3.10 presents the clear sky rays, i.e. incident ray, refracted ray and reflected ray, together with the altitude angle for each of the solstices and equinoxes. The albedo effect is evident from the variation of the reflected ray with observed higher albedo values during sunrise and sunset only due to the lower solar elevation. The spring and autumnal equinoxes have equal hours of daylight and darkness, therefore, the effect of the albedo is illustrated as one in Figure 3.10b.

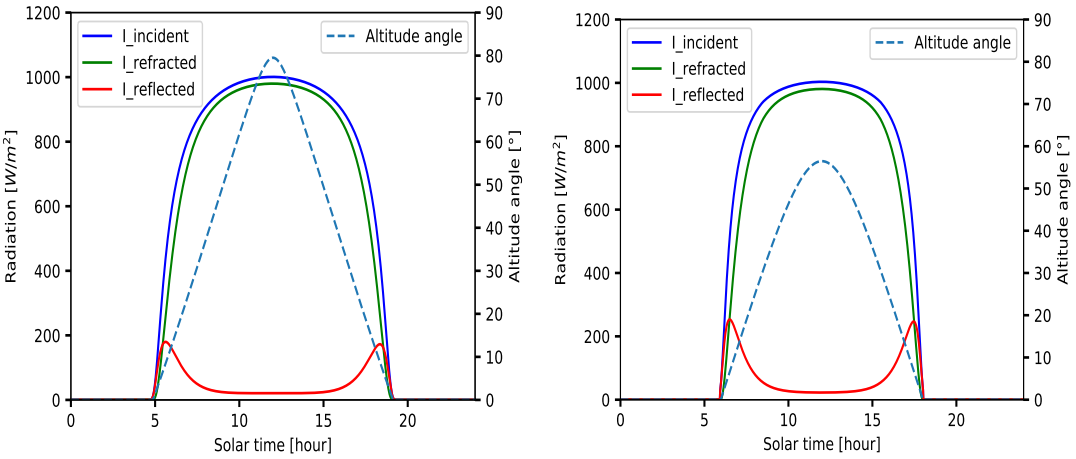

(a) Summer solstice.

(b) Spring/autumn equinox.

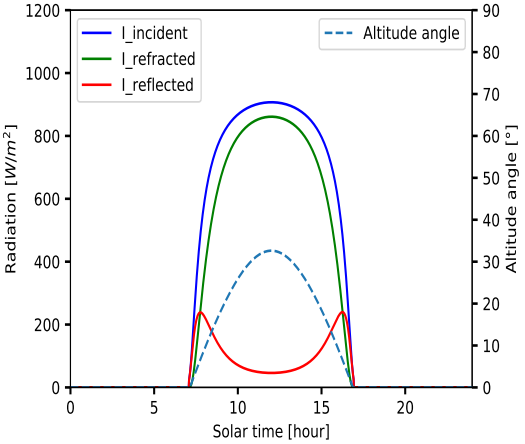

(c) Winter solstice.

Figure 3.10: Albedo effect on solstices and equinoxes [21].

Figure 3.11 illustrates the albedo variation on the summer solstice at the wavelength of 200 nm and 1100 nm. It is evident that a decrease in wavelength causes the albedo to be increased. The effect of the wavelength and temperature variation on the water surface albedo is evaluated for each of the equinoxes and solstice. The difference in the albedo due to the wavelength variation between the minimum and the maximum wavelength of 200 nm and 1100 nm is 3 %. The difference in the albedo due to the temperature variation between the minimum and the maximum temperature of 10 $°C$ and 100 $°C$ is 1 %. Therefore, the albedo dependence on the temperature variation is insignificant and negligible. These minimal variation of the albedo due to the temperature and wavelength difference are not the critical factors affecting the albedo.

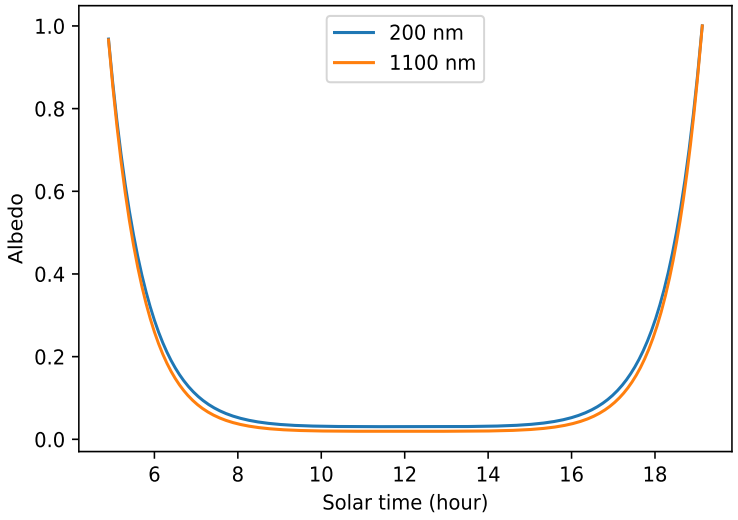

Figure 3.11: Albedo variation at different wavelength [21].

3.6.1 Solar Insolation on a Collector Surface

The real-world measured solar data do not only incorporate clear-sky days, but also days which are affected by cloudiness. Therefore, it is important to evaluate what the effect of the water surface albedo would be on these overcast days. Figure 3.12 illustrates the comparison of the variation of the reflected radiation using the default albedo value of 0.2 and the varying water surface albedo model on the inclined collector surface.

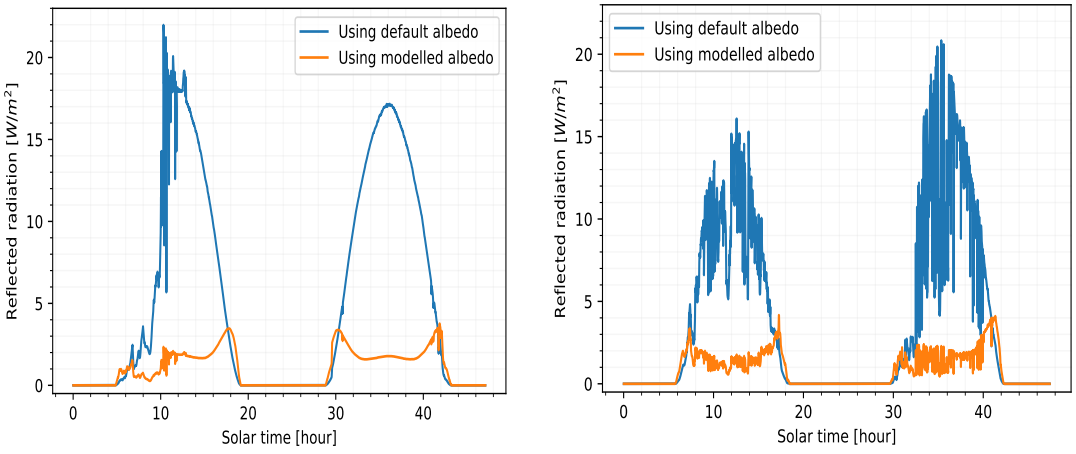

(a) An intermittent clear-sky and an clear-sky day.

(b) An overcast and a intermittent overcast day.

Figure 3.12: Reflected radiation on an inclined collector surface [103].

It is evident that the reflected radiation estimated using the default albedo value of 0.2 generates a larger attenuation when compared to utilising a modelled water surface albedo. Thus, effectively demonstrating the large uncertainty that may be included in the floating PV modelling when using a default albedo value. The reflected radiation estimated using the varying water surface albedo model on the inclined collector surface indicates higher peaks during the early morning and late afternoon only. Such a behaviour of the reflected radiation is due to the solar elevations angular dependency throughout the day on the refractive properties of the air and the water medium.

To better understand the implication of using the varying water surface albedo in estimating the reflected radiation on an annual basis, the dataset from 2018 is used to illustrate this effect. Figure 3.13 shows the annual trend of the reflected radiation on the tilted collector surface using the default albedo value in comparison to the varying water surface albedo. It is evident that the reflected radiation estimated using a default albedo value of 0.2 generates the same trend as the measured GHI, with higher solar radiation observed during summer and the lowest during winter. Whilst, the annual reflected radiation is roughly the same throughout the year when estimated using the varying water surface albedo model due to the fact that the incident angle throughout the days in the year remains the same. The reflected radiation on the inclined surface remains roughly less than 5 W/m^2 throughout the year.

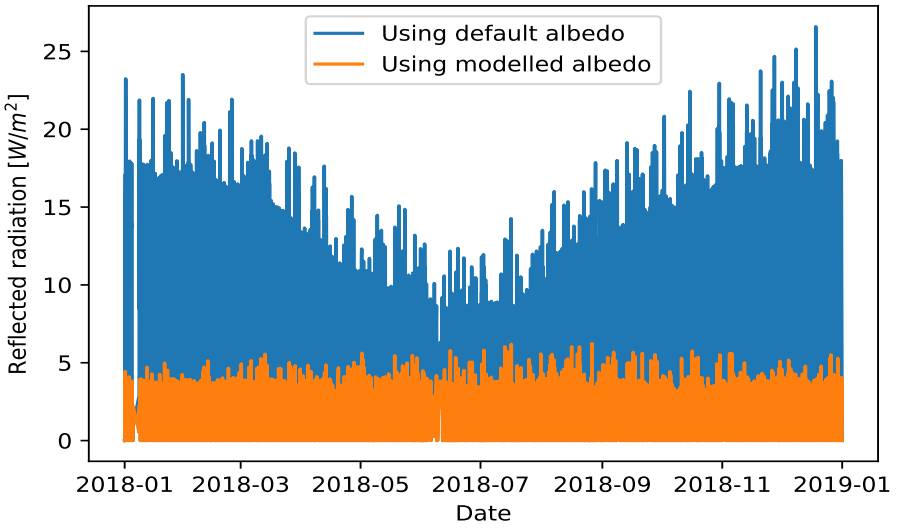

Figure 3.13: Annual reflected radiation on an inclined collector surface [103].

To evaluate the overall effect of the water surface albedo model on the total insolation of the collector surface, the annual insolation energy is calculated. Table 3.6 presents the annual energy for each of the radiation components and the reflected radiation estimated using the modelled water surface albedo and

the default albedo value of 0.2. It is evident that the energy contribution of the reflected radiation component estimated using the modelled water surface albedo is significantly lower than using a default albedo value of 0.2. Therefore, using the default albedo value of 0.2 in predicting the reflected radiation on a collecting surface may overestimate the approximation.

Table 3.6: Annual insolation energy for 2018.

Insolation	**Albedo = 0.2**	**Albedo = Modelled**
I_{BC} $[kWh/m^2]$	1623.46	1623.46
I_{DC} $[kWh/m^2]$	411.49	411.49
I_{RC} $[kWh/m^2]$	30.43	7.88

Furthermore, the annual energy for various years is calculated to the differences created when using the modelled albedo and the default albedo value. Table 3.7 presents the annual energy contribution for the year 2013 to 2018. It is observed that estimating the reflected radiation using the default albedo value overpredicts the annual energy by 1.15 % in comparison to using the varying water surface albedo.

Table 3.7: Annual insolation energy contribution for the various years.

Total Energy $[kWh/m^2]$			
Year	**Albedo = 0.2**	**Albedo = Modelled**	**Differences** [%]
2013	1938.57	1915.92	1.17
2014	1988.79	1965.35	1.18
2015	2042.23	2018.44	1.16
2016	2046.86	2023.43	1.14
2017	2066.11	2043.15	1.11
2018	1985.30	1962.75	1.14

3.7 Summary

In this chapter, the albedo of a flat water surface is modelled as a function of time, temperature and wavelength. A full description of the Sonbesie weather station and its instrumentation set-up from which the solar radiometric data is retrieved is also provided. The procedure for data acquisition and filtering the datasets is also described. The Ineichen-Perez clear-sky model is used to predict the clear sky irradiance.

The refractive index of air and water are theoretically estimated using the Edlén's and Lorentz-Lorens equation, respectively. The difference in the refractive index of standard air and liquid water is less than 10^{-3} % and 0.3 %, respectively, for the temperature range from 0 $^{\circ}C$ to 100 $^{\circ}C$. Thus, indicating that the variation in the refractive index of standard air and liquid water is not largely dependent on the temperature differences but rather the wavelength of the radiation.

The reflection and refraction of water are estimated using Fresnel's and Snell's laws. The results of the albedo model show that an average albedo value of 0.0207 is observed during daylight. Higher albedo values are observed during sunrise and sunset due to the lower solar elevation. The albedo effect on the solstices and equinoxes is also illustrated together with the effect of the water surface albedo on the collector insolation, and the annual energy yield. It is found that estimating the reflected radiation using the default albedo value of 0.2 overpredicts the annual energy by 1.15 % in comparison to using the varying water surface albedo.

The difference in the albedo due to the wavelength and temperature variation is found to be 3 % and 1 %, respectively, between the minimum and the maximum wavelength of 200 nm and 1100 nm and temperature of 10 $^{\circ}C$ and 100 $^{\circ}C$. Therefore, the albedo dependence on the temperature variation is insignificant and negligible.

Chapter 4

PV System Performance Analysis

This chapter provides detailed information about the floating solar system and the ground-mounted PV system. Site assessment and system analysis is also conducted for two different systems. The instrumentation set-up is described as well as the procedure for acquiring the data and filtering the datasets. Finally, the measured data are analysed. Figure 4.1 presents the flow chart of the structure used in this chapter.

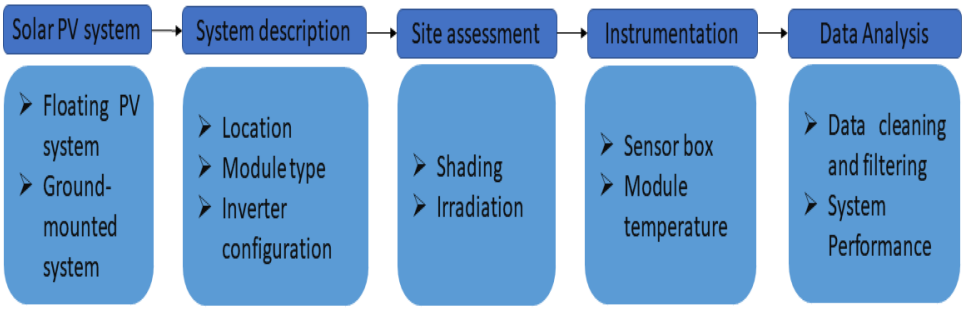

Figure 4.1: Flow diagram of the chapter structure.

4.1 Floating PV System

The most commonly used floating solar technology is deployed on floating pontoons on top of the water-body and the modules are fixed on these floating platforms [23], [43], [44]. Utilising solar PV on floating pontoons does not allow the full benefit of water cooling on the system performance. To fully benefit from the cooling effect of the PV modules on the water surface, deploying modules directly on a thin polymer canvas is a better solution [45].

Therefore, effectively enabling lower cell operating temperatures due to the direct thermal contact of the PV modules with the water surface. Figure 4.2 shows Ocean Sun's patented floating PV technology. The unique design is inspired by nature. The floaters sit on the water surface just like a giant water lily.

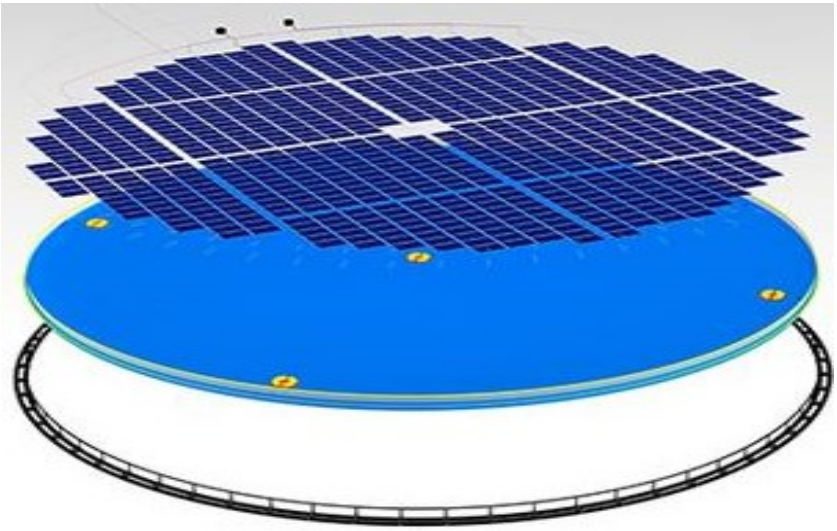

Figure 4.2: Ocean Sun's patented floating PV technology [125].

This innovative technology introduces a cost-effective, efficient, and a durable solution to floating solar [45]. The technology deploys customized PV modules on a thin hydro elastic membrane to achieve greater benefits from floating solar PV. The hydro-elasticity characteristic of the membrane allows the PV modules to move freely with the waves [45]. The hydro elastic membrane is carefully designed allowing walking on it when installed on the water surface. The thin polymer membrane minimizes the use of materials to achieve the required buoyancy and therefore providing the lowest theoretical FPV installation cost [125]. Figure 4.3 shows the layout of the Ocean Sun's patented floating PV technology. This technology allows for easy and faster installation of PV modules [45].

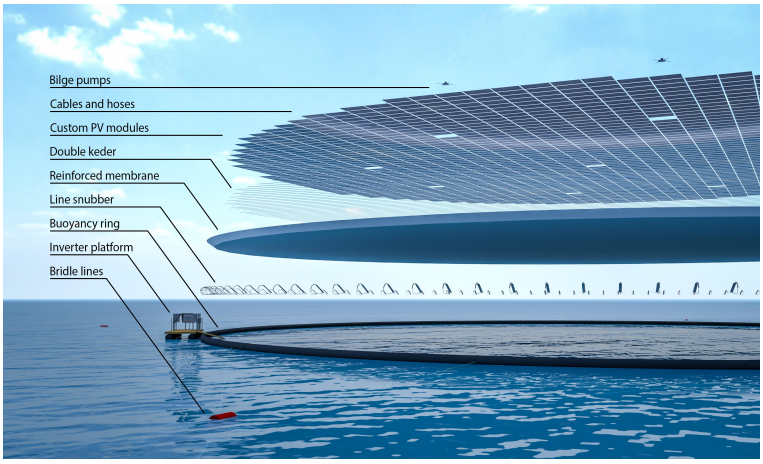

Figure 4.3: Layout of the Ocean Sun's patented floating PV technology [45].

In this research work, Ocean Sun's first FPV pilot project in Skaftå, West Coast of Norway is analysed. The prototype of the floating solar system is shown in Figure 4.4. It is located in a fjord between the mountains near a shore in Osterøy, Hordaland, with latitude 60°27'14.4"N and longitude 5°37'19.2"E. The FPV system was installed and powered in May 2017.

(a) The fjord.

(b) Shoreline and dock proximity.

Figure 4.4: Location of the floating PV system [126].

4.1.1 The system

The floating PV system consists of the floating membrane, PV modules, cables, water pump and the inverter. The PV modules are placed on the floating structure, and the inverter is situated offshore. Figure 4.5 shows the floating solar installation in Norway.

Figure 4.5: Offshore floating solar installation [127].

The water pump is located in the middle of the floating canvas. The primary function of the water pump is to pump the freshwater accumulated through the rain out from the floating structure and back into the ocean. Figure 4.6 shows the water pump between the strings on the floating canvas.

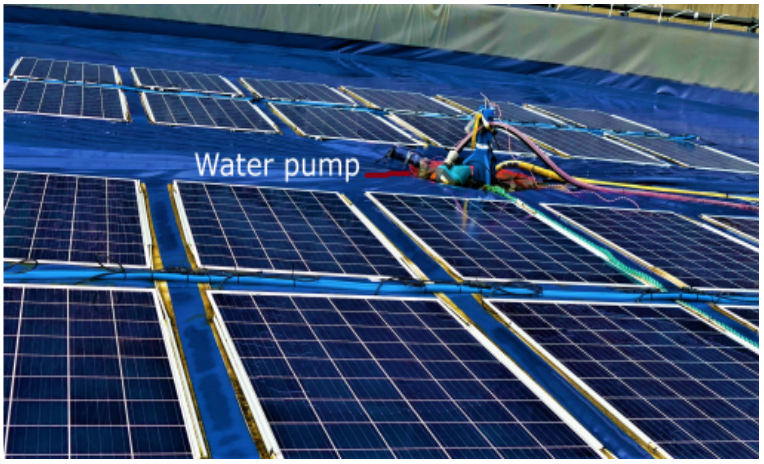

Figure 4.6: Solar modules on the floating canvas with a water pump located between the strings.

The PV modules at the floating PV system are Trina 60 cell multi-crystalline DUOMAX PV modules from Trina Solar; with a rated power of 270 W [128]. The PV modules have a P_{max} temperature coefficient of -0.41 $\%/°C$ [128]. Frameless glass-glass PV modules are used to ensure full contact with the 1 mm thick hydro-elastic canvas. There are 2 strings with 12 modules in each string. Each string is connected with 12 PV modules in series. The 2 strings are connected to different MPPTs. The total rated power is 6.48 kWp. Both strings are connected to a 6 kWp Fronius Primo 6.0-1 inverter [129]. The

inverter has 2 MPP trackers and a voltage range between 80-800 V [129]. The inverter logs the produced power from both the strings separately. The power from the FPV system is transported to the inverter onshore via an approximately 20 m long cable. Figure 4.7 shows the efficiency characteristic of the inverter. The inverter has a maximum efficiency of 98.1 % [129]. The technical specification of the DUOMAX PV modules and the Fronius Primo inverter is accessible at [128] and [129], respectively.

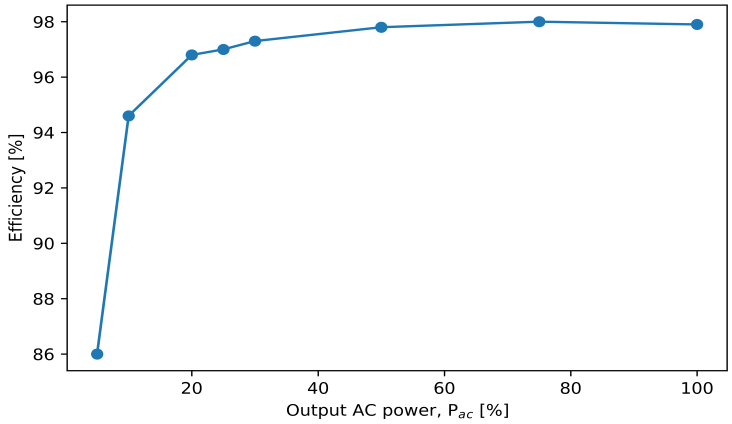

Figure 4.7: Fronius Primo 6.0-1 inverter efficiency (data acquired from [129]).

In this first Ocean Sun's pilot, each PV module has a junction box and cables located on its rear side which will create local air gaps. These air gaps in the area of the junction box will reduce the area of thermal contact between the canvas and the PV modules, which will effectively have an impact on the cooling effect from the water surface.

To investigate the efficiency of this novel technology, it was decided to elevate one string with polypropylene pipes. In February 2019, only two modules were initially lifted with two pipes underneath the back-surface. Pipes with a diameter of 32 mm and 40 mm were both tested to lift the modules. However, the 32 mm diameter pipe was used as it was readily available. Figure 4.8 shows the floating PV system (picture taken at 08:30 am, the day after the modules were lifted) with the two elevated modules which appear as white due to accumulation of frost. It is evident that the two modules which are lifted have a much lower temperature in comparison to the modules that are in direct thermal contact with the canvas.

Figure 4.8: FPV system with two elevated modules (Image courtesy of P De Paoli).

Furthermore, each module in one string is lifted with three polypropylene pipes. The pipes are placed between the rear side of the modules and the canvas which effectively creates air gaps. 2 pipes were fixed on opposite ends of the module and 1 pipe in the centre of the module. The pipes are fixed to their position using strips. Figure 4.9 shows the elevated string with the air gaps between the modules and the canvas.

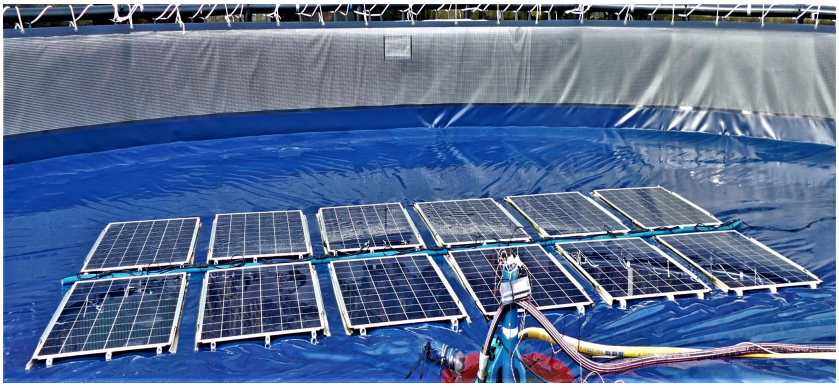

Figure 4.9: Elevated FPV string.

The lifted string or 'air-cooled' string is then compared to the 'water-cooled' string which is in thermal contact with the canvas. The production data from both the strings are compared, and other parameters are also investigated to evaluate the potential of deploying such a floating PV technology. Figure 4.10 shows the water-cooled and the air-cooled string.

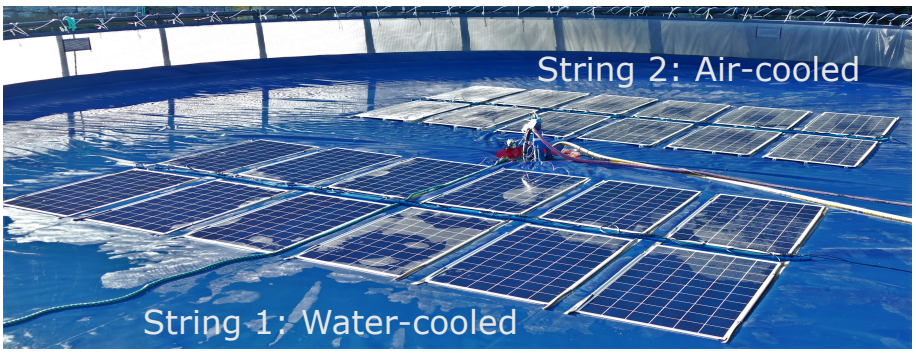

Figure 4.10: The FPV strings at Skaftå.

4.1.2 Instrumentation

4.1.2.1 Fronius Sensor Box

To measure the various parameters, such as irradiance, wind speed, air and water temperature, a Fronius sensor box was utilised. The technical specification of the sensor box is accessible at [130].

4.1.2.2 Temperature measurements

Two PT1000 sensors were used to measure the air and water temperature. Both these sensors have a measuring range of -40 $°C$ to +180 $°C$, and a tolerance of $\pm 0.8\ °C$ (from -40 $°C$ to +100 $°C$) [131]. The air and water temperature sensors are attached along the edge of the rail, below the wind speed sensor. The PT1000 water temperature sensor is submerged approximately 1 m into the water.

4.1.2.3 Irradiance measurement

A Fronius monocrystalline Si sensor is used to measure the irradiance at the FPV system. The Z-shaped weather-proof sensor is mounted on the outer rim of the rail closest to the water-cooled string and is placed approximately 2 m away from the sensor box. The sensor measuring the irradiation is mounted at the same angle as the solar panels, i.e. a tilt angle of zero. On an annual average the sensor has a ± 5 % error [132]. The technical specification of the reference cell is accessible at [132].

The solar radiometric data measured at the FPV site includes different types of days such as clear-sky, overcast (cloudy), intermittent clear-sky and overcast days. Figure 4.11 shows the monthly global horizontal insolation received at the FPV site. The irradiation is summed for each day in the given month. The highest irradiance is recorded in summer, for July.

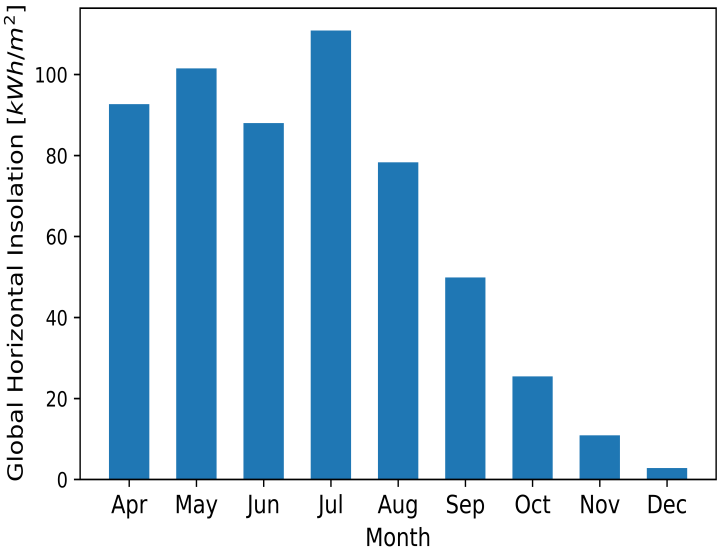

Figure 4.11: Monthly accumulated global horizontal insolation received at the FPV site.

The output power increases with an increase in irradiance level. Therefore, at higher output power the inverter will be operating at constant efficiency. This is in accordance with the inverter efficiency curve provided previously in Subsection 4.1.1, Figure 4.7 for the Fronius Primo inverter. Therefore, the FPV data for higher irradiance with greater output power is further analysed. To conduct realistic observations on the floating PV system, the months with the lowest accumulated insolation, October-December, is avoided for further analysis.

Figure 4.12 shows the heat map of Bergen for the year 2019. The annual clear-sky GHI is estimated using the Ineichen-Perez clear-sky model available in Pvlib Python [104], [113]. As evident, lower GHI is experienced in the months, January-March and October-December, with shorter duration of daylight.

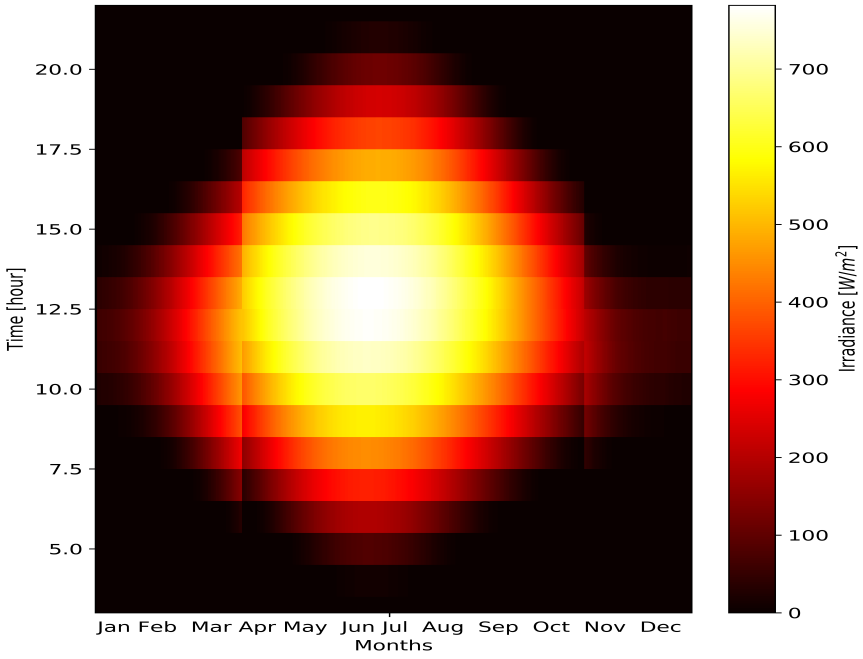

Figure 4.12: Heat map of Bergen.

4.1.2.4 Wind Velocity

The Fronius cup anemometer with reed contact is used to measure the exact wind velocity. The wind sensor has a threshold of 2.5 m/s, which is the minimum velocity at which the wind sensor will measure at its rated reliability. The wind sensor has a resolution of 1 m/s, and a tolerance ± 5 % from 5 m/s upwards [133]. The cup anemometer is attached on a 3 m rod, which is fixed directly above the Fronius sensor box and is approximately 4 m above the reference solar cell. The technical specification of the wind sensor is accessible at [133]. Figures 4.13 and 4.14 shows the instrumentation at the floating PV system.

Figure 4.13: Irradiance sensor mounted on the rail.

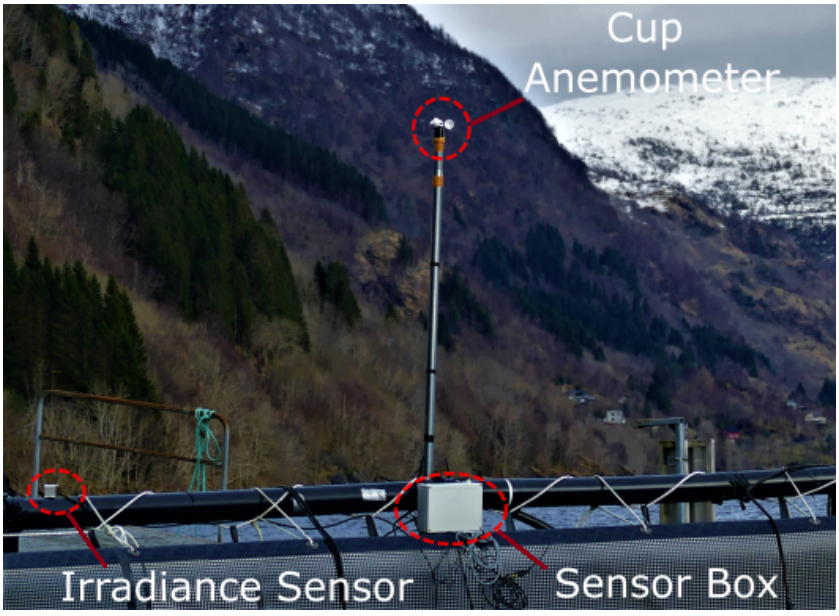

Figure 4.14: Wind speed instrument, sensor box and irradiance sensor.

4.1.2.5 Back-surface module temperature

The PT100 silicon patch sensor is used to measure the back-surface module temperature. The sensor is a 4-wire configuration from Thermosense. The operating range of the sensor is -30 $°C$ to +200 $°C$ [134]. The technical specification of the sensor is accessible at [134]. The back-surface module temperature sensor data is logged on a separate logger, which is mounted on top of the water pump. A 4-channel temperature data logger from MadgeTech with a resistance temperature detector (RTD) is used. The data logger has a temperature range of -200 $°C$ to +850 $°C$ (probe dependent), temperature resolution

of 0.001 $^{\circ}C$ (probe dependent), and a calibrated accuracy of ± 0.04 $^{\circ}C$ (probe dependent) [135]. The technical specification of the RTD temperature data logger is accessible at [135].

In February 2019, 4 temperature sensors were attached on the rear-side of the 4 modules located closest to the water pump and the centre of the canvas. The 2 sensors were attached on the 2 PV modules of the water-cooled string and the remaining 2 sensors on the 2 PV modules of the air-cooled string. Figure 4.15 shows the 4 modules represented in a red square that has temperature sensors mounted on the back surface.

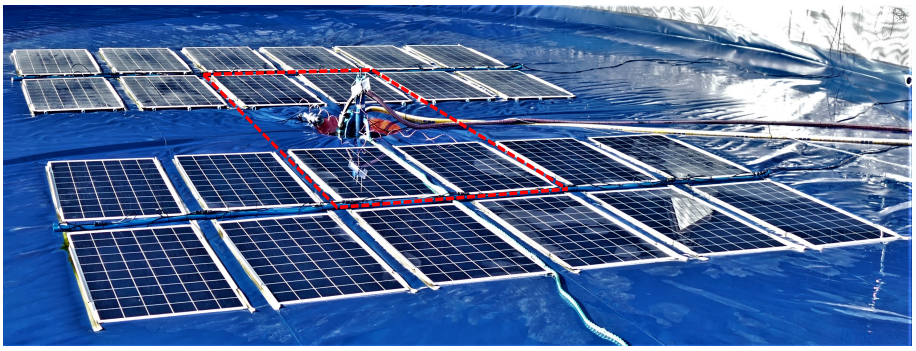

Figure 4.15: Temperature sensor attachment on the selected modules.

The sensors and its cables were reinforced using duct tape to ensure that the sensors did not fall off. Usage of duct tape can affect the heat transfer through the modules. The 4 modules with temperature sensors attached were lifted with only 2 pipes to allow space for the sensors. More specifically, the temperature sensors were attached on either of the two solar cells in the middle of the second row on each of the 4 modules closest to the water pump. Figure 4.16 shows the elevated module with 2 pipes which are represented in a red square, and the 2 solar cells indicated in an orange rectangle on which the temperature sensors are attached.

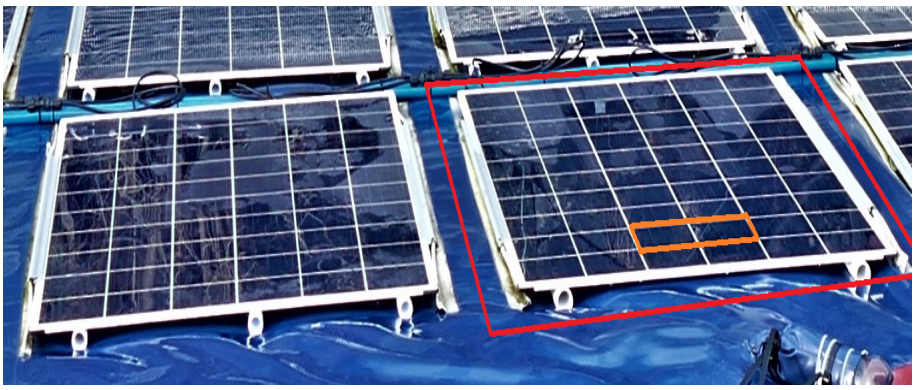

Figure 4.16: Temperature sensor attachement on PV module.

4.1.3 Data Collection

At the floating PV system, the following parameters are logged in real-time: irradiance, wind speed, air and water temperature, string production, and the back-surface module temperature. The operating data from the floating PV system are available for download through an online Fronius Solar.web portal. Solar.web is a free tool which gives an overview of all up-to-date and archive data for monitoring and analysing the system [136]. The required measured data are transferred to Fronius Solar.web via a LAN or WLAN connection through a data-manager that is integrated into the inverter. The online portal provides the option to select the specific parameter and date range for downloading the data as a .zip-archive containing files with comma-separated values (CSV). All the datasets are logged with a five-minute interval.

The production data at the floating PV system is logged since 16 May 2017, while the sensor box data are logged since 12 March 2019. Figure 4.17 shows the milestone of the floating PV system at Skaftå. The measured data from the year 2019 is analysed in this research work.

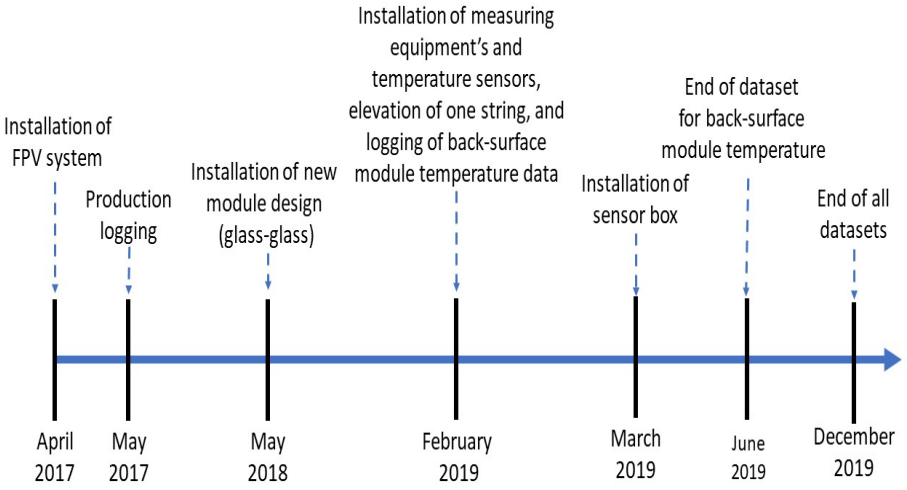

Figure 4.17: Timeline of Skaftå's floating system.

4.1.4 Data Cleaning

To reduce uncertainties in this study, the measured data parameters from the floating PV system are thoroughly evaluated for every timeframe, identifying NaN values and missing data values. Since the one string was only elevated end of February 2019, and the sensor box only started logging data mid-March 2019, only the data with a five-minutes interval from the period 01 April 2019 to 30 September 2019 is of interest. Timestamps for the mentioned period with at least 1 NaN value is identified and dropped. Figure 4.18 shows the missing data for the respective months in evaluation for the unshaded operational time period between 8:00 to 13:00. The shading effect on both the floating PV is explained in detail in Subsection 4.2.1.1.

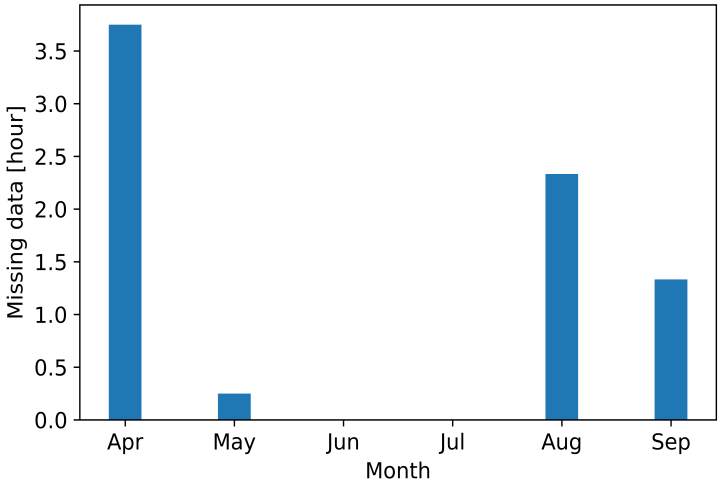

Figure 4.18: Missing data at Skaftå's floating system.

From Figure 4.18, it is evident that most of the months contain none or very few hours of missing values. At a maximum, only 3.75 hours of data is missing in April which may not introduce a large error. Missing data can occur due to inactive or improper functioning of the data logger or instrumentation.

4.2 Data Analysis

All mathematical calculations and measured data are analysed using Python with the data analysis Pandas library, and matplotlib and Bokeh visualization libraries through an open-source Jupyter Notebook for interactive computing and data visualization. All mathematical calculations of the measured solar radiometric data are performed using the open-access simulating tool, PVLIB Python [104], specifically the 0.7.1 version [105].

4.2.1 Site Assessment

In this section, all data from the floating PV system is analysed for the period 01 April 2019 to 30 September 2019.

4.2.1.1 Shading

Since the floating solar system is located in a fjord with mountains on either side, the system becomes shaded for a longer period of the day. Figure 4.19 shows the average instantaneous power every fifth minute of the two FPV strings together with the difference in the power of the strings. The graph shows the average values of the power variation throughout the period, April

to September, and how the shade affects the power produced from the floating PV strings.

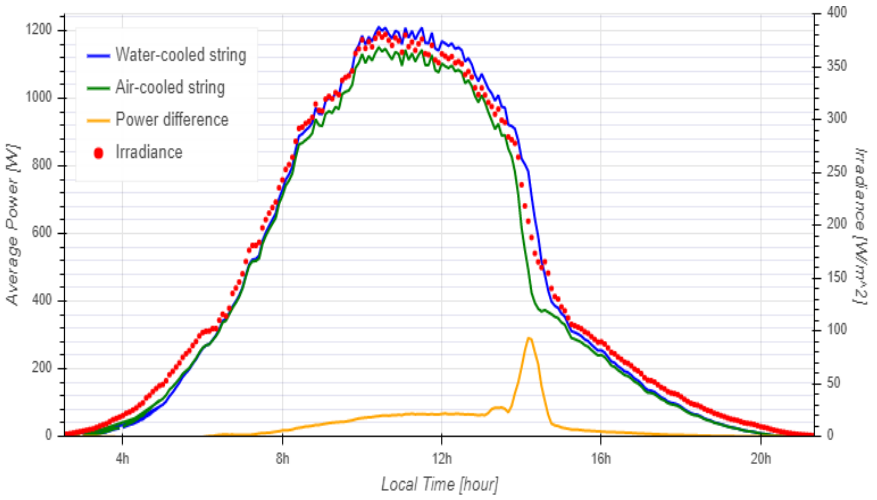

Figure 4.19: Average instantaneous power.

When a spike in the string difference is observed, this shows the difference in shading times. The system provides an unshaded operational time period up until 13:00, and the system experiences shading from 13:00 onwards. Also, important to note that the air-cooled string is located closest to the shore, which means that the air-cooled string will encounter shading earlier than the water-cooled string in the afternoon. Therefore, this will change the production throughout the year. Sunrise and sunset occur before 4:00 and after 20:00. As the intensity of the irradiance level drops, the air-cooled string is shaded first, then the reference cell and lastly the water-cooled string become shaded. A maximum difference of 290 W is observed between the two strings due to the shading.

4.2.1.2 Irradiance

The reference cell measures the GHI at the floating PV site as described previously in Subsection 4.1.2.3. Figure 4.20 shows the fluctuation of the monthly measured GHI at the FPV site. The dataset is plotted for irradiance values with a time interval of 5 minutes for every day of the given month.

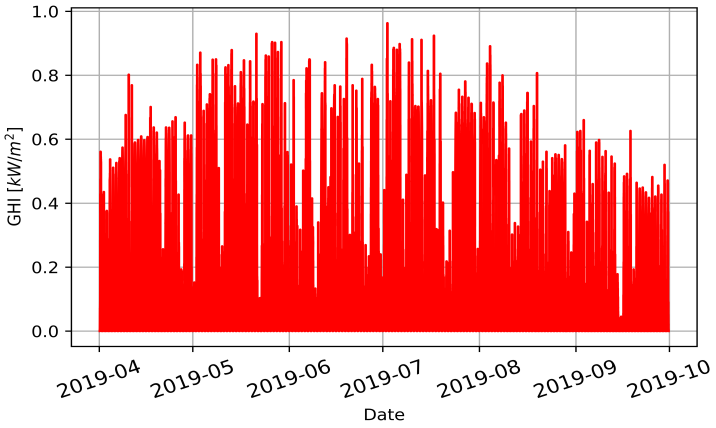

Figure 4.20: GHI at a temporal resolution of 5 minutes received at the FPV site for the year 2019.

Due to the variation of the Sun's path throughout the year, the measured irradiance will vary substantially for every month. Thus, creating a difference in the time when strings become shaded. Figure 4.21 presents the heat map of the GHI for the period 01.04.2019 to 30.09.2019 with hourly averages of irradiance values for every day of the month. High irradiance is measured between 8:00 to 13:00. Lower irradiance represented by dark patches is measured after sunrise and before sunset.

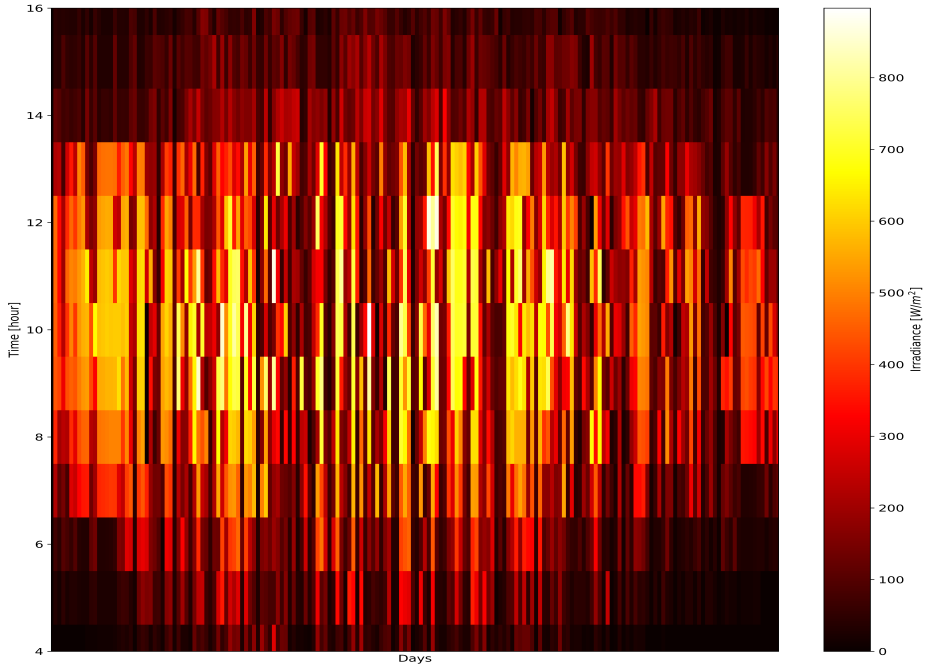

Figure 4.21: GHI from April to September.

Figure 4.22 presents the heat map for July which has the highest amount of irradiance observed. It is evident that the highest amount of GHI is present between 8:00 and 13:00, and there is an abrupt decline in irradiance after 13:00 due to shading.

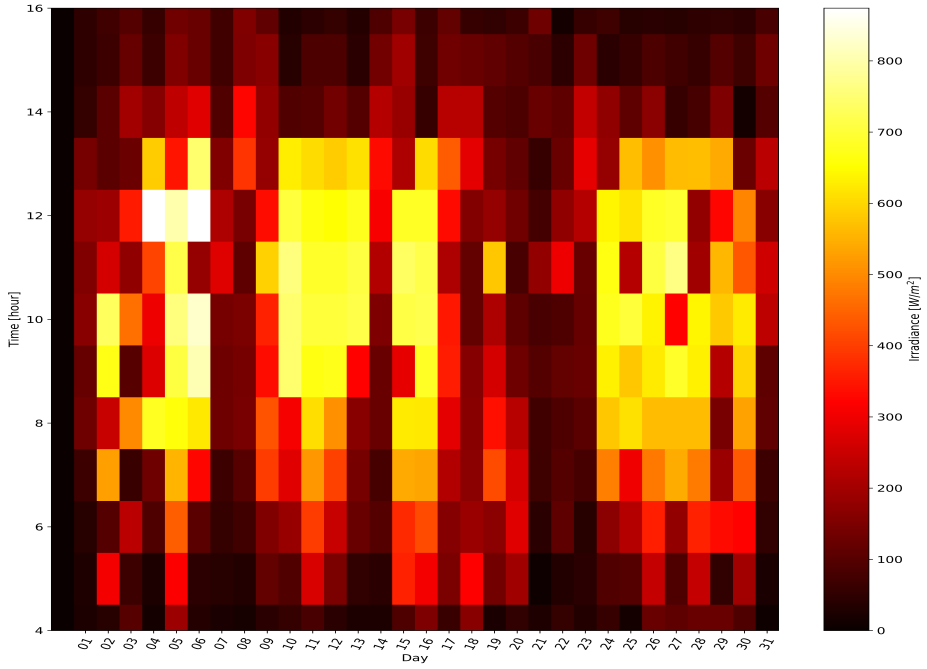

Figure 4.22: GHI for July.

4.2.2 Instantaneous Observation

4.2.2.1 Power production

Figure 4.23 shows the power produced for both the FPV strings for the period 01.04.2019 to 31.12.2019. The values are averages of the power produced every five minutes for every day of the month. A larger difference between the two FPV strings power production is observed during the given months, April to September.

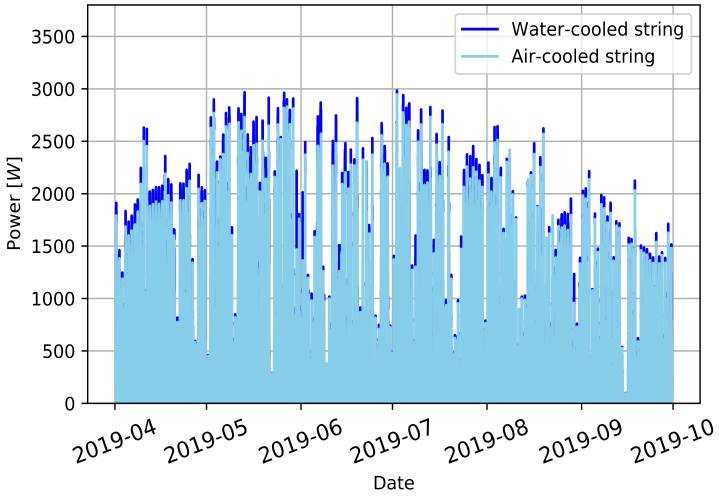

Figure 4.23: Instantaneous power production every five minutes interval.

Due to the variation of the Sun's path throughout the year, the measured irradiance will vary for every month. Thus, creating a difference in the power produced between the floating PV strings. Figure 4.24 presents the monthly average production for both the strings together with the difference from 4:00 to 19:00. Mpp1 and Mpp2 represent the average monthly power for the water-cooled string and the air-cooled string, respectively. The values are determined by taking hourly averages for each day in the given month. The shaded area represents the standard deviation. It is evident that on a monthly average, the air-cooled string becomes shaded first, and the power production declines after 13:00. Therefore, the usage of unshaded operational time between 8:00 to 13:00 for the months, April to September, should not create any differences in the error when comparing monthly evaluations.

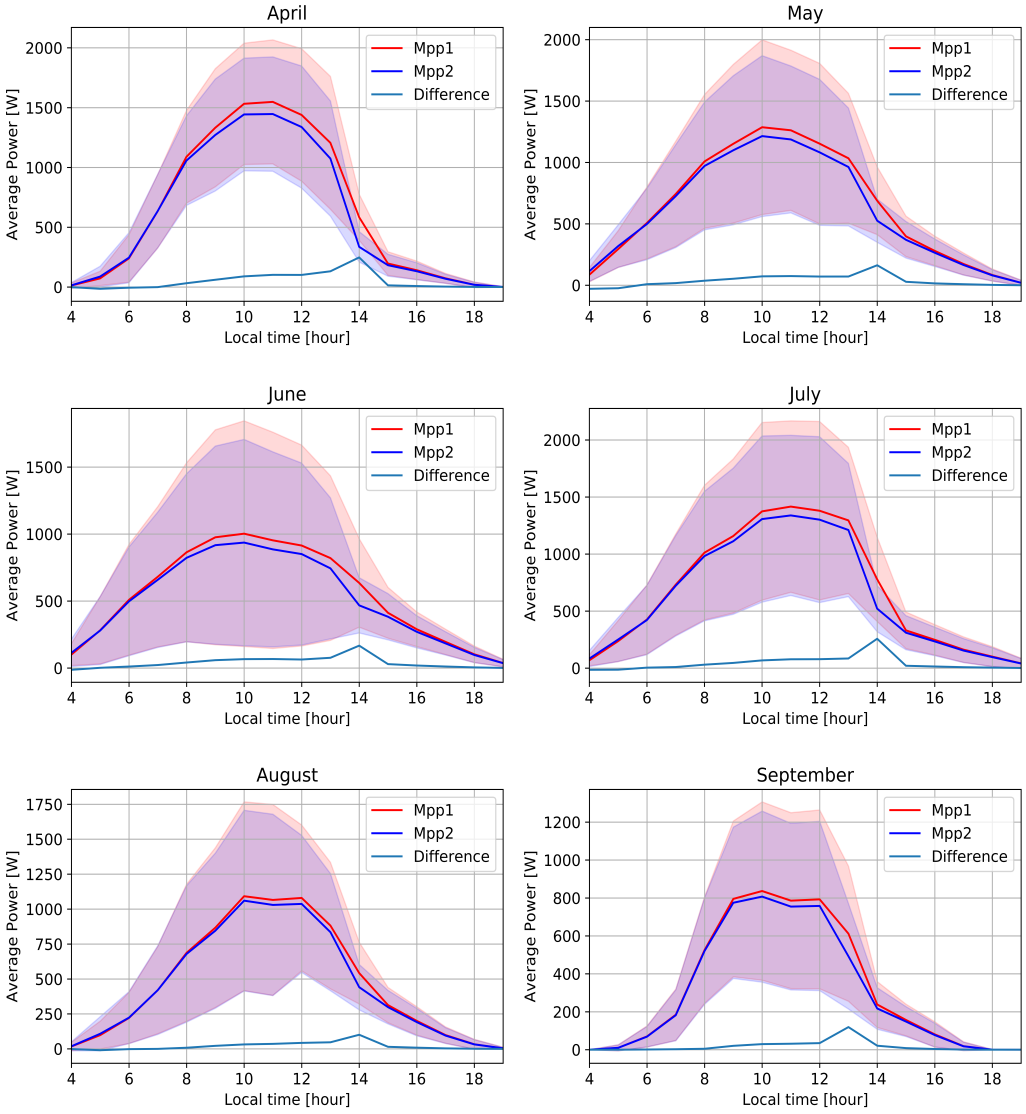

Figure 4.24: Monthly average production and the power difference for the FPV strings.

To evaluate how the string production differs for every given month, the instantaneous difference in the power produced every fifth minute for every day of the given month is determined. The difference in power produced between the air-cooled and the water-cooled string, $P_{diff\_A|W}$, is calculated as follows:

$$P_{diff\_A|W} = P_{WC} - P_{AC}. \tag{4.2.1}$$

Whereby, P_{AC} and P_{WC} is the air-cooled and the water-cooled power production, respectively. Figure 4.25 presents the instantaneous power production from April to September, for the unshaded operational time from 8:00 to 13:00. The positive power difference is experienced during the daylight, after sunrise

and before sunset, when the water-cooled string produces more than the air-cooled string. The maximum power difference is experienced in September, whereby the water-cooled string produces 422.75 W more than the air-cooled string.

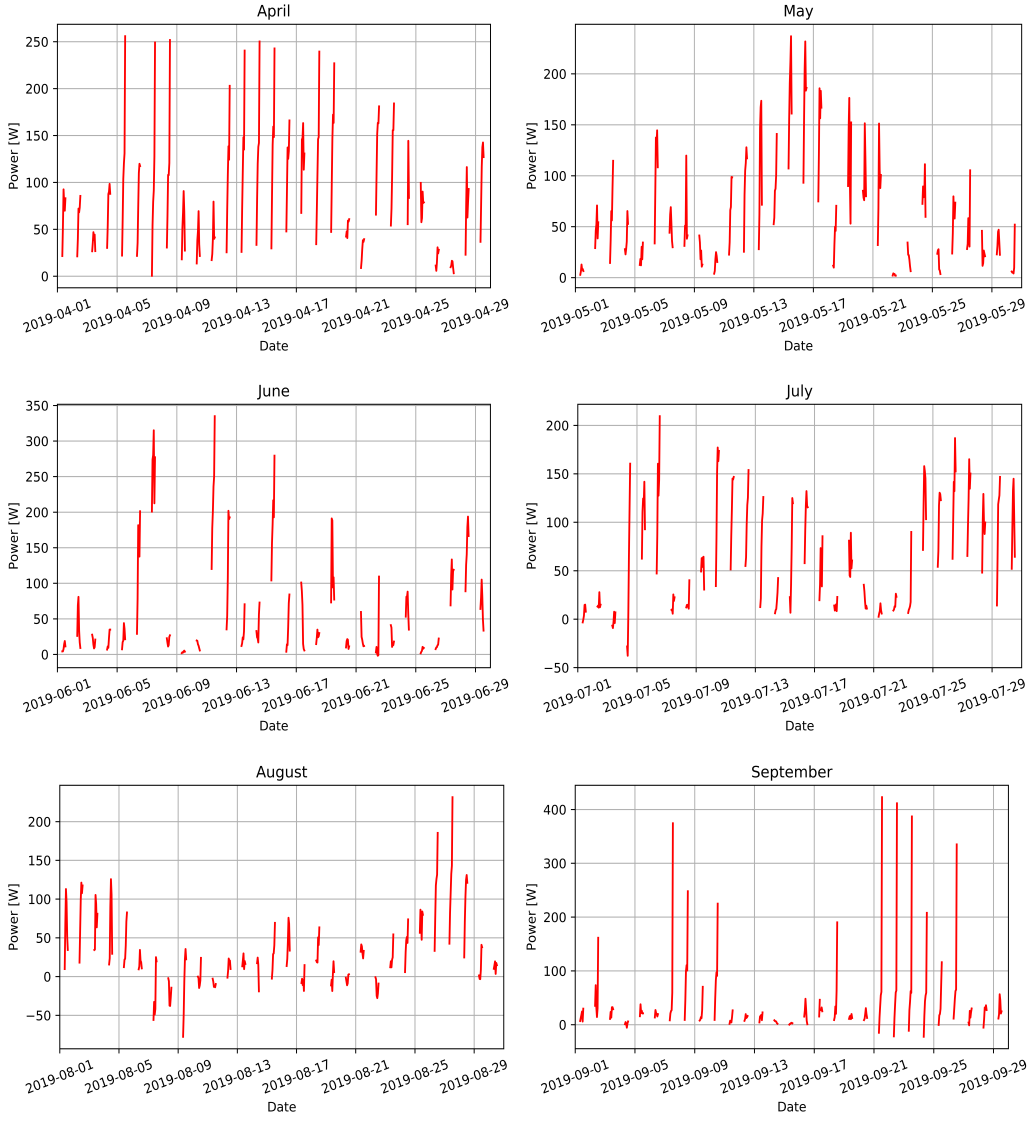

Figure 4.25: Monthly instantaneous string production difference.

Figure 4.26 presents the total energy and the cumulative summation for both the strings for the months April to September, for the unshaded operational time from 8:00 to 13:00. The cumulative energy of the water-cooled string is greater than the air-cooled string. Thus, indicating that the cooling of the water-cooled string is more effective due to the direct contact with the floating canvas.

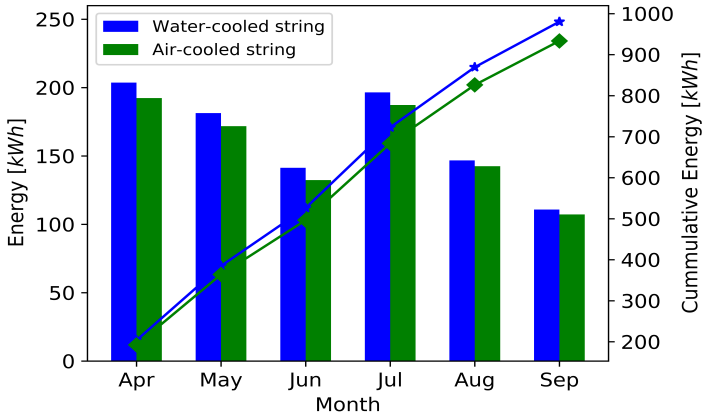

Figure 4.26: Monthly accumulated and cumulative energy production.

4.2.2.2 Difference In String Production

Avoiding the shading effect, and evaluating the floating PV strings for the duration of the unshaded operational time from 8:00 to 13:00, Figure 4.27 presents the accumulated energy for both the strings for each day of the given month and the energy difference for the given months. The energy difference is calculated as a difference between the monthly accumulated energy of the water-cooled string and the air-cooled string, $E_{diff\_A|W}$, as follows:

$$E_{diff\_A|W} = E_{WC} - E_{AC}. \tag{4.2.2}$$

Whereby, E_{AC} and E_{WC} is the monthly accumulated energy of the air-cooled string and the water-cooled string. On a maximum, the water-cooled string produces 11.31 kWh more energy than the air-cooled string. It is evident that for the given months the water-cooled string produces more energy when compared to the air-cooled string with a positive energy difference observed.

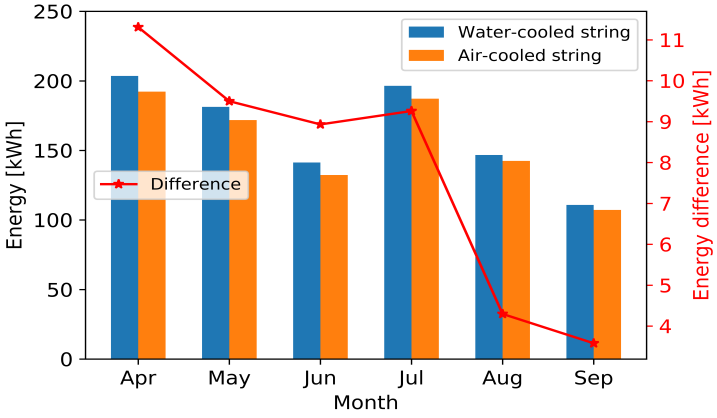

Figure 4.27: Monthly accumulated energy production and difference.

If the power produced is evaluated at different intervals of irradiance, it is possible to evaluate and compare both the FPV strings under specific irradiance intervals. Figure 4.28 shows the power produced for both the FPV strings at specific irradiance intervals of 50 W/m^2. The plotted points are determined by grouping the power production values of both the strings that are within the irradiance intervals for every day of the months, April to September, and then taking an average value of the accumulated power. A linear relationship is observed, as expected, between the average power and irradiance level. As the irradiance level increases the water-cooled string presents a gradual increase in production when compared to the air-cooled string.

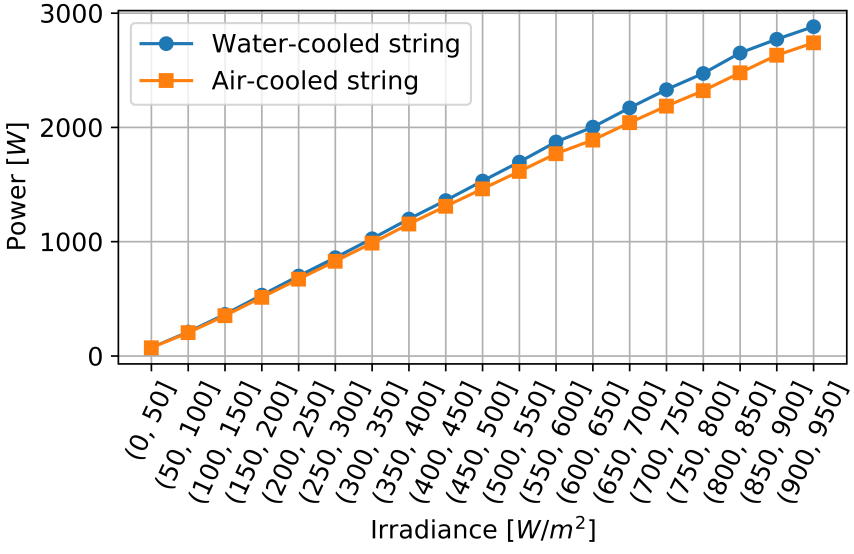

Figure 4.28: Power produced for both strings with variation in irradiance.

4.2.2.3 Water and Air temperature

Figure 4.29 shows the measured instantaneous water and air temperature for the period 01.04.2019 to 31.12.2019. The dataset is plotted for temperature values with a time interval of 5 minutes for every day of the given month. The air temperature fluctuates more in comparison to the water temperature.

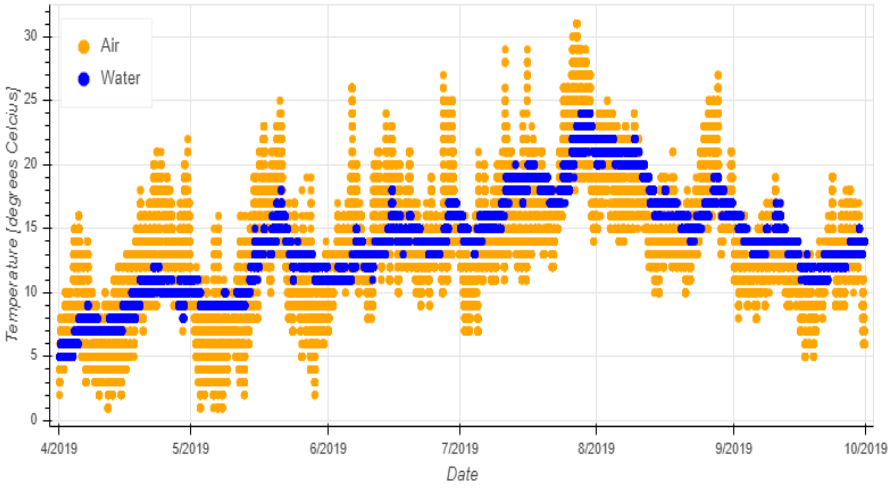

Figure 4.29: Measured air and water temperature.

Figure 4.30 illustrates the instantaneous air and water temperature difference at the floating PV site with a five-minute interval. The temperature difference between air and water, $T_{diff\_A|W}$, is calculated as:

$$T_{diff\_A|W} = T_{air} - T_{water}. \tag{4.2.3}$$

Whereby, T_{air} and T_{water} is the air and water temperature, respectively. The maximum and the minimum temperature difference between air and water is 14 $°C$ and -10 $°C$, respectively. Which means that on a maximum, the air temperature is 14 $°C$ higher than the water temperature. Negative temperature differences between the air and water occur at lower ambient temperatures.

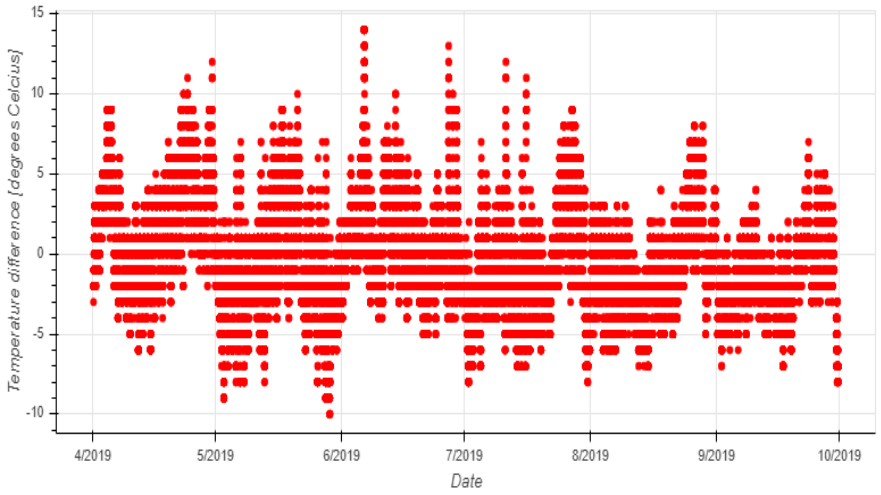

Figure 4.30: Air and water temperature difference.

If the water and air temperatures are evaluated at different intervals of irradiance, it is possible to evaluate the differences between air and water temperature under specific irradiance intervals. Figures 4.31 and 4.32 presents the hourly average of the water and air temperature for the given irradiance, respectively, for the period 01.04.2019 to 30.09.2019. The air temperature shows an increase as the irradiance increases, whereas the water temperature tends to remain more constant throughout the irradiance levels.

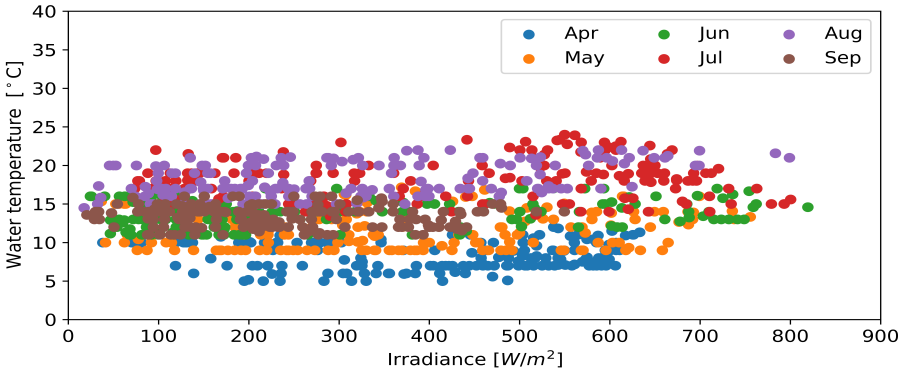

Figure 4.31: Water temperature relative to irradiance.

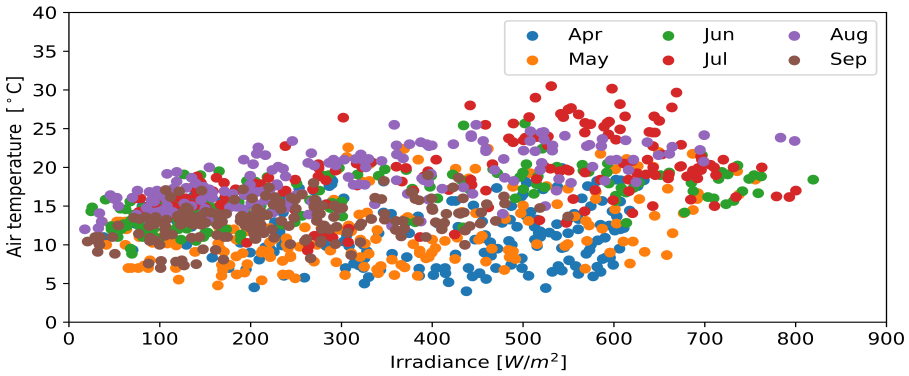

Figure 4.32: Air temperature relative to irradiance.

It is observed that for irradiance levels less than 200 W/m^2, the water temperature is greater than the air temperature under the same irradiance, this is due to the water being warmer than air during lower irradiance. Lower irradiance is typically experienced after sunrise and before sunset due to lower solar elevation. For irradiance higher than 200 W/m^2, the air temperature is (on average) higher than the water temperature. The air temperature increases with an increase in irradiance.

4.2.3 System Performance

The quality of a PV system is commonly measured by the dimensionless performance ratio (PR) metric. PR describes the relationship between the actual energy and the theoretical energy output. The actual energy is the measured energy output of the PV system. The theoretical energy is a possible energy production if the PV system is continuously operational under the STC conditions, together with achieving the STC efficiency. The theoretical energy output is calculated as a product of the radiated power onto the PV modules and the rated efficiency of the PV modules. The PR is defined accordingly in the IEC 61724 standard. The PV system performance ratio is formulated as follows [137]:

$$PR = \frac{P_{AC\_out}}{P_{STC} \times \frac{G_m}{G_{STC}}} = \frac{P_{AC\_out}}{G_m \times \eta_{ref} \times A}. \tag{4.2.4}$$

Whereby, P_{AC_out} is the measured output AC power in kW, and P_{STC} is the total DC power rating at STC in kW. G_m is the incoming irradiance measured for the PV system, and G_{STC} is the irradiance at STC ($1000W/m^2$). η_{ref} is the rated efficiency of the PV modules which is 16.4 % under the STC conditions. A is the total area of the solar panels in usage. Each solar panel used at the floating PV site has dimensions of 1.658 m × 0.99 m. The total area of the 12 modules in each floating PV string is 1.645 × 12 = 19.74 m^2.

The PR calculated for a PV system includes all the system losses such as optical losses, PV conversion, inverter efficiency, etc. PR is not dependent on the irradiance received or the orientation of the PV modules at the particular location, therefore the performance metric provides a comparison between two different PV systems.

PR is greatly dependent on cell temperature. Lower operating cell temperature is favourable for improved PR. PR determines the 'quality' of the system rather than the performance of the system. Since both the floating PV strings were installed at the same timeframe, using the same Trina Solar module type and ratings, it is presumed that the PR of both the FPV strings should be equal for all the months. However, the performance ratio of a system is susceptible to weather factors, temperature effects, shading, soiling, and reflection. Therefore, the performance is often calculated using a temperature-corrected factor. When the PR is evaluated for a longer time period (typically a year) than the weather effect is usually eliminated. However, when working with a shorter period of time, the performance of a system with seasonal changes is analysed. Since the PR in this research work is evaluated for daily averages for a shorter period, the temperature corrected performance ratio is used.

The temperature-corrected PR, PR_{corr}, is calculated using the expression as follows [137]:

$$PR_{corr} = \frac{P_{AC\_out}}{P_{STC}(\frac{G_m}{G_{STC}}) * Ck}, \tag{4.2.5}$$

with,

$$Ck = 1 - (\frac{\gamma}{100})(T_{STC} - T_{cell}). \tag{4.2.6}$$

The term Ck is used to correct the temperature difference between the actual measured temperature and the STC temperature. γ is the temperature coefficient of power in $\%/°C$. The value of γ is usually negative and is unique to the installed PV module. T_{STC} is the cell temperature at STC ($25°C$) and T_{cell} is the cell temperature in $°C$. The STC rated power of an individual Trina Solar PV module is 270 W and the P_{max} temperature coefficient of -0.41 $\%/°C$. The maximum operating power is calculated as $P_{STC} = (12 \times 270)\ W$ since each of the FPV string consists of 12 PV modules.

Since the back-surface module temperature is not available for the entire period of evaluation, the cell temperature is estimated using the Nominal Operating Cell Temperature (NOCT) method. The NOCT is the temperature reached by the open-circuited cells in a PV module. The NOCT model is established on the behaviour of the solar module which is operating under no load. The

electrical conversion efficiency of the PV array under no-load operation is zero. The following test conditions are applicable to the NOCT model [48], [49]:

- Global solar irradiance of 800 W/m^2;
- Ambient temperature of 20 $°C$;
- Wind speed of 1 m/s.

The approximated expression for calculating the NOCT is given by [48]:

$$T_{cell} = T_{amb} + \frac{T_{cell\_NOCT} - T_{amb\_NOCT}}{G_{T\_NOCT}} \times G_T. \tag{4.2.7}$$

Whereby, T_{amb} is the ambient temperature in $°C$, T_{cell_NOCT} is the Nominal Operating Cell Temperature (NOCT) in $°C$, T_{amb_NOCT} is the ambient temperature at which the NOCT is defined as 20 $°C$, G_{T_NOCT} is the global solar radiation at which the NOCT is defined as 800 W/m^2, G_T is the solar radiation striking the PV array $[W/m^2]$. The NOCT equation estimates the wind speed at 1 m/s and with an open rack mounting. The NOCT conditions are defined accordingly in the IEC/TS 61836 standard.

To evaluate the performance of the water-cooled string and the air-cooled string, the performance ratio of both the floating PV strings is calculated using the 'un-corrected' PR equation and the temperature-corrected PR equation. Possible differences are evaluated and compared. All data from the floating PV system is analysed for the period 01 April 2020 to 30 September 2020 for the unshaded operational time from 8:00 to 13:00.

4.2.3.1 Instantaneous observation

Figure 4.33 shows the daily averages using the 'un-corrected' or the 'standard' PR, ignoring the temperature effect, for the water-cooled and the air-cooled string. As evident, the PR of the water-cooled string is higher than the air-cooled string. Interestingly, the PR of both the FPV strings is not consistent throughout the period, as expected. The variation in PR is possibly due to seasonal changes and temperature differences. Since PR is used to show the quality of the system, and the quality for both the FPV strings is the same. Therefore, to account for the differences the floating PV strings is now evaluated using the temperature-corrected PR.

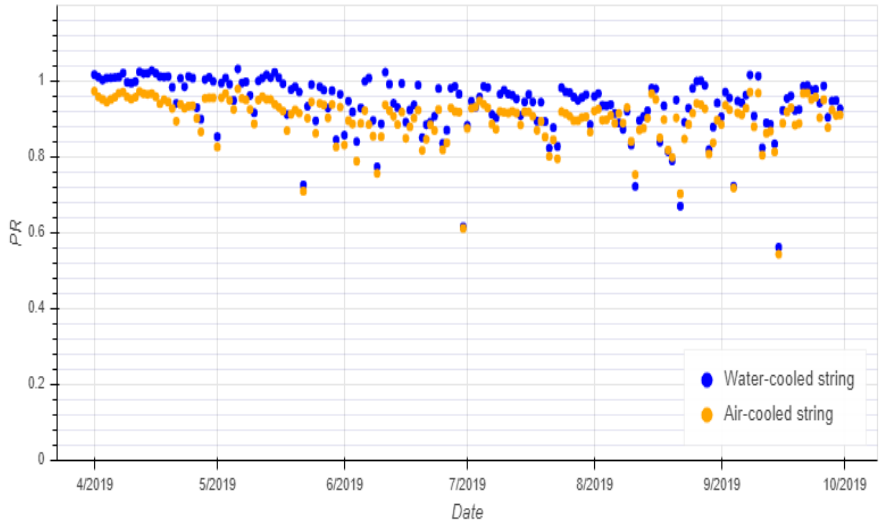

Figure 4.33: 'Un-corrected' PR for the FPV strings.

Figure 4.34 shows the comparison of the standard performance ratio, PR, and the temperature corrected performance ratio, PR_{corr} for the water-cooled string and the air-cooled string, respectively. The PR values are the daily average from April to September, for irradiance greater than 200 W/m^2. Evaluating the PR for irradiance greater than 200 W/m^2 removes the outliers presented previously in Figure 4.33. The PR of the water-cooled string is higher than the air-cooled string. However, even after using the temperature corrected PR, the performance due to seasonal changes has still not been suppressed. Since the PR of both the FPV strings is not the same for the different months, there is a discrepancy present in some measurements. It is possible that an unknown factor could be affecting the temperature-corrected PR. This unknown factor is likely water temperature, which is not accounted for in the temperature-corrected PR. The PR does not account for the differences in the solar spectrum between the various seasonal months, thus influencing the produced results. It is also possible that the measuring equipment at the FPV site was not calibrated often. For future references, further research should be conducted to investigate the temperature corrected PR in terms of the seasonal changes and also to ensure calibration of measuring equipment.

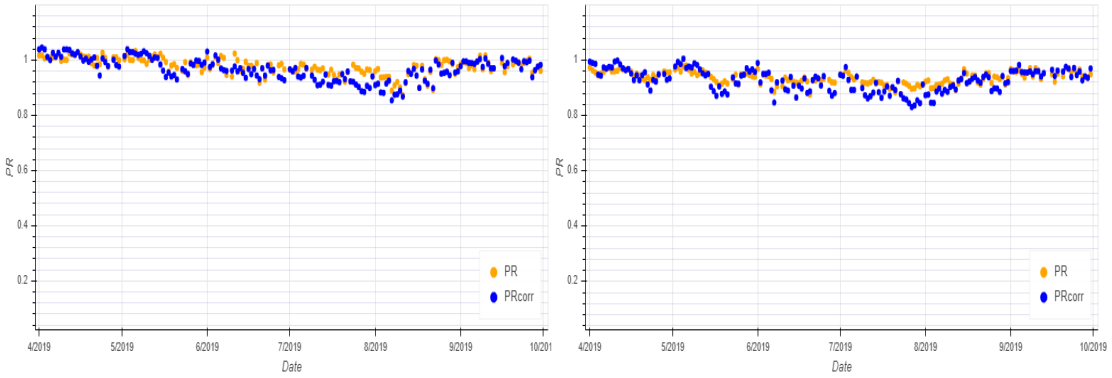

(a) Water-cooled string. (b) Air-cooled string.

Figure 4.34: Comparison of the standard performance ratio and the temperature corrected performance ratio for the FPV strings.

Figure 4.35 presents the daily averages of the temperature corrected PR for both the floating PV strings for the month with higher accumulated irradiance, April to September, for irradiance greater than 200 W/m^2.

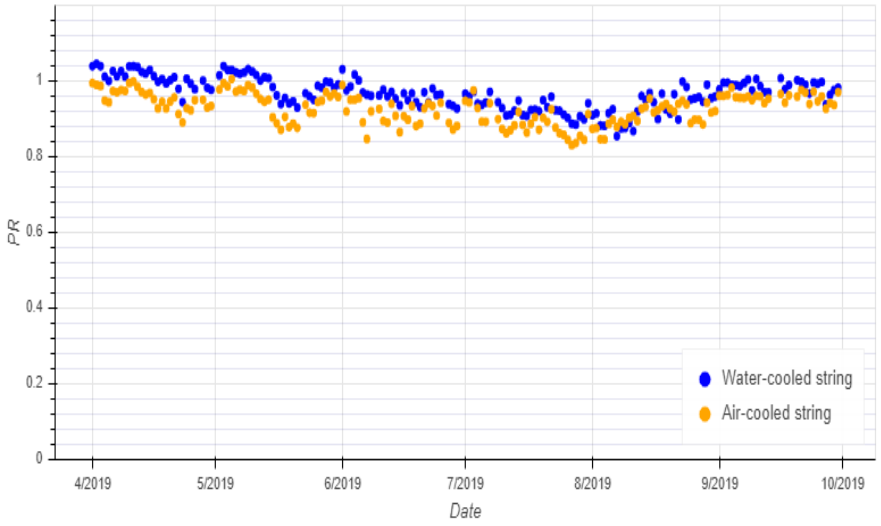

Figure 4.35: Temperature corrected PR for irradiance greater than 200 W/m^2 for the FPV strings.

Figure 4.36 presents the monthly averages of the temperature corrected PR and the air and water temperature for both the floating PV strings for the month with higher accumulated irradiance, April to September. It is evident that the PR of the system is greatly dependent on the temperature differences. Increase in temperature decreases the PR and when the temperature is constant for the months, a constant PR value is observed. This is evident for the PR of the water-cooled string for the months of July and August.

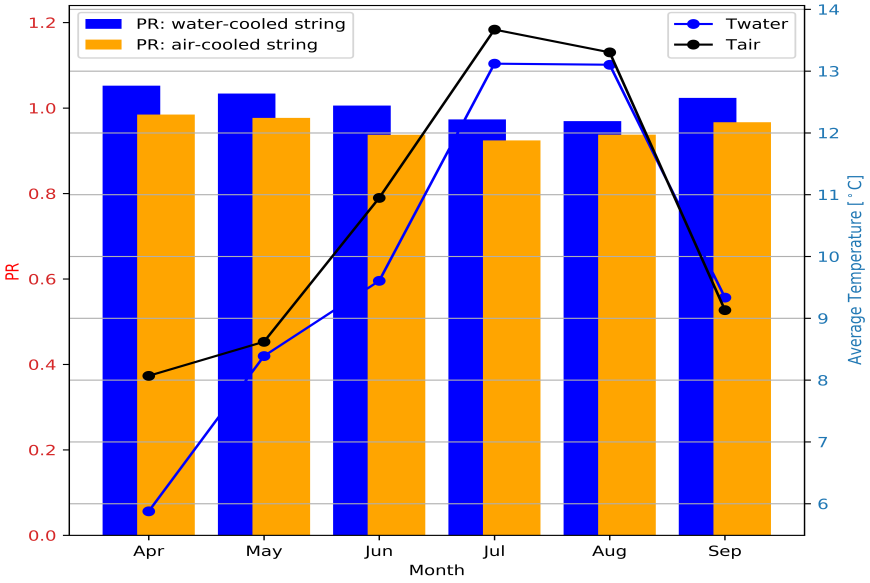

Figure 4.36: Monthly average temperature corrected PR and air and water temperature.

Figure 4.37 presents the boxplot of the temperature corrected PR for both the floating PV strings for the months with higher accumulated irradiance, April to September, for irradiance greater than 200 W/m^2. The green line in the middle of each boxplot represents the median, (Q_2), of observation, and the upper end of the boxplot is the upper quartile, (Q_3), which represents the median of the upper half. The lower half portion of the boxplot is the lower quartile, (Q_1), of the observation, representing the median of the lower half. The central box represents the interquartile range (IQR) of the data under observation given as $IQR = (Q_3 - Q_1)$. The IQR reveals the variability of the data set. The whiskers at the upper half and lower half at each end of the boxplots represent the maximum and the minimum point of observation given as $Q_3 \pm (1.5 \times IQR)$. Any observations outside this range are considered to be the outliers which are represented by the black circle shapes.

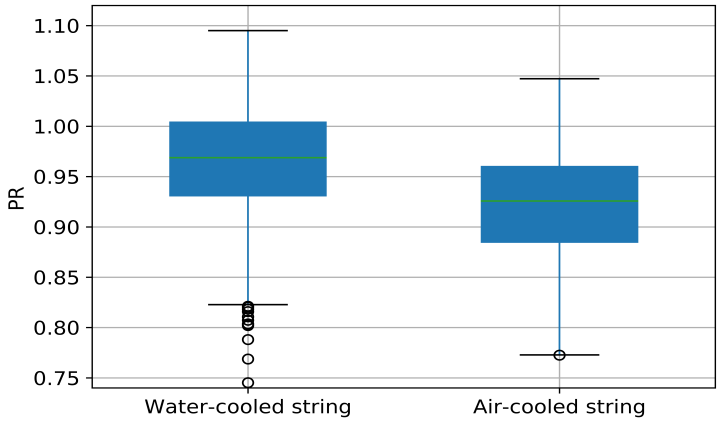

Figure 4.37: Box plot of the temperature corrected PR for the FPV strings.

The median for both the FPV strings is below the PR equal to one, but substantially higher for the water-cooled string in comparison to the air-cooled string. The average PR for the water-cooled and the air-cooled string is 0.97 and 0.92, respectively, for irradiance greater than 200 W/m^2. The average performance values of the FPV strings are very high, especially in the Nordic context. PR values for newly installed PV systems typically range between 0.7 to 0.9 [138]. The higher PR values are also due to the fact that the FPV system is relatively a small system, with shorter cables. Thus, indicative to presume that the net system losses are small and the cooling effect is favourable considering the climatic conditions in Norway.

In this research work, the main scope is to determine how well the water-cooled string performs in comparison to the air-cooled string, and not the 'quality' of the floating PV strings. The PR of both the FPV strings is also not the same for the different months, as there is a discrepancy present in some measurements. Therefore, it is recommended that further research should be conducted to correct the PR for temperature and also to ensure the calibration of measuring equipment.

4.2.3.2 String Comparison

Figure 4.38 presents the yield difference of the water-cooled string relative to the air-cooled string for the months with the most accumulated irradiance, April to September, for irradiance greater than 200 W/m^2. The percentage yield difference is calculated as follows:

$$Yield_{diff} = \frac{MPP1_{power} - MPP2_{power}}{MPP2_{power}} \times 100. \tag{4.2.8}$$

Whereby, $MPP1_{power}$ and $MPP2_{power}$ is the accumulated monthly power production of the water-cooled string and the air-cooled string, respectively. The water-cooled string that is in direct contact with the canvas has higher power than the air-cooled string which is elevated from the canvas with an air gap of 32 mm. The water-cooled string performs between 3.17 % to 7.32 % better than the air-cooled string.

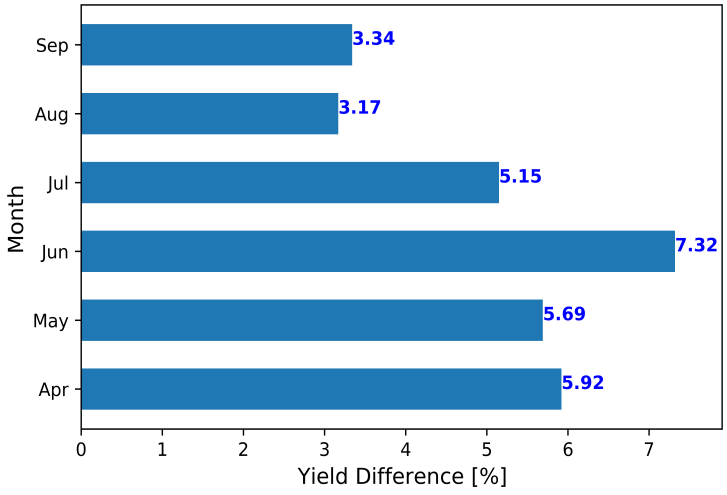

Figure 4.38: Yield of the water-cooled string.

4.3 Ground-mounted PV System

The operational data from a solar PV plant, Kalkbult power plant, in the Northern Cape, South Africa, with latitude 30°09'31.1"S and longitude 24°08'13.7"E is acquired for this research work to determine the heat transfer coefficient of the PV modules. It is a fixed-tilt ground-mounted PV plant with a capacity of 75 MW. And is actively delivering electricity to the grid since September 2013. The PV modules are tilted at an angle of 30 °C, as measured from the ground as the reference axis. Standard practice is for PV modules to be tilted at the same angle as the latitude angle of the location. The solar PV plant consists of 312 000 solar panels. The solar panels are from BYD, P6-30 series model, with a 240 Wp maximum power at STC conditions and a module efficiency of 14.75 % [139]. The PV modules have a P_{max} temperature coefficient of -0.47 %/°C [139]. This utility-scale PV power plant covers a land space of 105 hectares. The power plant is connected to inverters, transformers and a high voltage sub-station. The SMA Sunny Central 800CP XT inverter logs measured current of string-pairs [140], whereby each string pair consists of two parallel PV module strings each with 24 PV modules. A string is constructed from 24 PV modules in series and 2 strings are connected in parallel to form

string-pairs. The technical specification of the SMA inverter is accessible at [140]. Figure 4.39 shows the aerial view of the solar power plant.

Figure 4.39: Aerial view of the Kalkbult solar PV power plant [141].

4.3.1 Data Collection

The solar PV power plant has 5 weather stations of which one weather station is located at the main control building and the other four weather stations are located at different positions throughout the power plant. Figure 4.40 shows the distribution of the 5 weather stations at the solar power plant. Weather stations denoted by CB and TR means control building and transformer stations, respectively. At the weather stations, the string-pair current output, solar irradiance, wind speed, ambient temperature, absolute air pressure, rain intensity, relative humidity, wind direction and back-surface module temperature are measured. These various meteorological data are measured in real-time at a time interval of five minutes by the Supervisory Control And Data Acquisition (SCADA) system using the Modbus communication protocol. Modbus is widely used for transmitting information over serial lines between electronic devices [142].

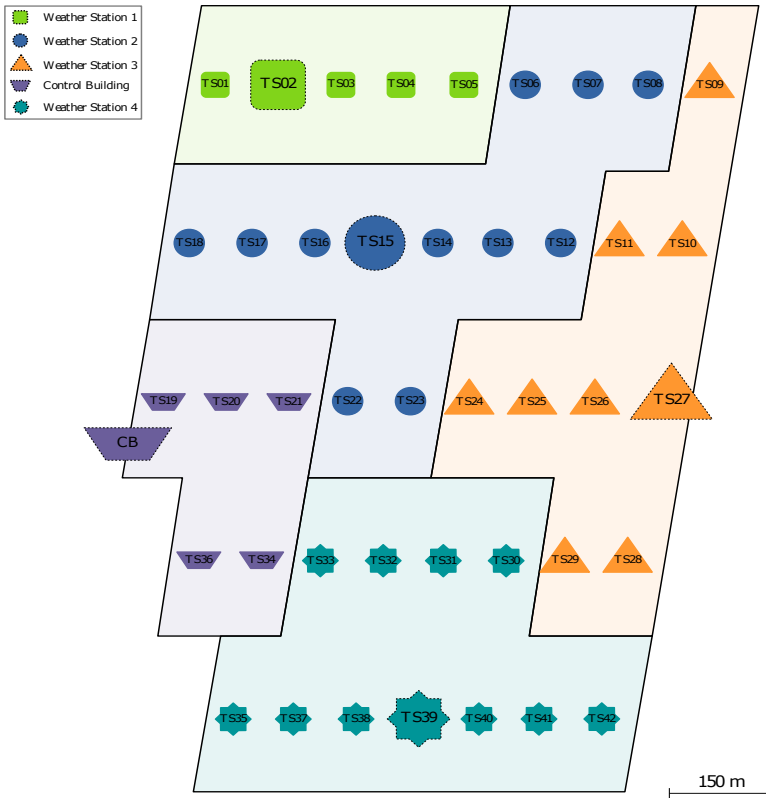

Figure 4.40: Weather station and inverter location at the solar power plant [143].

The DC current measurement of each string-pair is received at the inverter through a reliable monitoring system, the Sunny String-Monitor (SSM). The SSM is a DC sub-distributor which allows several strings to be connected in parallel to monitor the input string currents [144]. At the power plant, 10 string-monitors are used to measure the DC current of up to 8 string-pairs connected to each string-monitor.

4.3.2 Data Cleaning

The weather station at the control building has a lot of erroneous and missing data and does not measure irradiance and any temperature parameters such as back-surface module temperature and ambient temperature. Therefore, measured data from only the remaining on-site 4 weather station is used in this research work. Raw data with a resolution of the five-minutes time interval for the period 01 May 2015 to 31 May 2019 is acquired from the weather stations. Figure 4.41 illustrates the data handling process. All columns with missing

data < 1 hour are linearly interpolated to obtain a more complete and accurate dataset value.

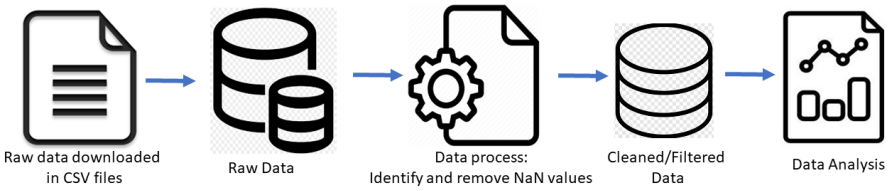

Figure 4.41: Data handling process.

4.4 Data Analysis

All data from the ground-mounted PV system is analysed for the 4 weather stations, TR02, TR15, TR27, and TR39 for the period 01 January 2018 to 31 December 2018.

4.4.1 Irradiance

Figure 4.42 shows the measured instantaneous average GHI at a temporal resolution of 5 minutes. The irradiance values are calculated as an average from the 4 weather stations, i.e $((GHI_{TR02} + GHI_{TR15} + GHI_{TR27} + GHI_{TR39})/4)$, whereby GHI_X represents the measured GHI at the given weather stations. The GHI is evaluated for the string-pairs closest to the respective weather stations. The maximum recorded GHI is 1472.06 W/m^2.

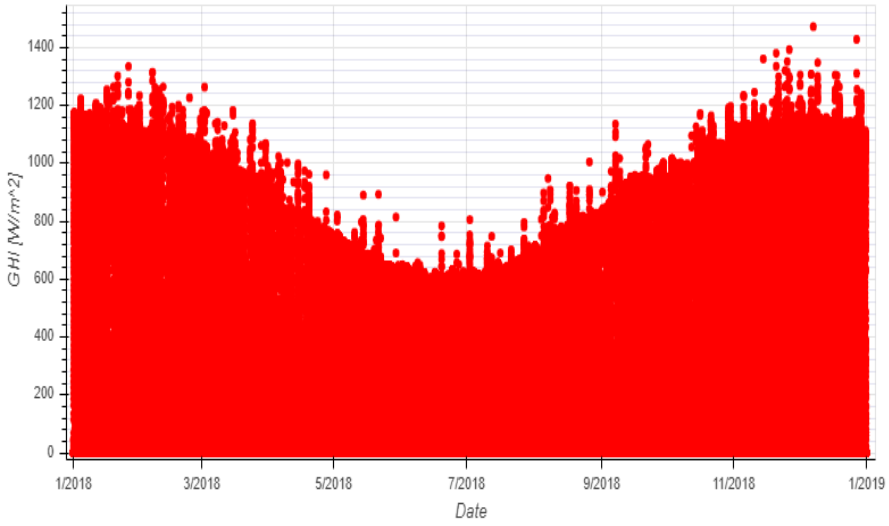

Figure 4.42: GHI at a temporal resolution of 5 minutes received at the ground-mounted system for the year 2018.

Due to the variation of the Sun's path throughout the year, the measured irradiance will vary substantially for every month. Figure 4.43 presents the heat map of Kalkbult solar power plant with hourly averages of irradiance values for every day of the given months. The irradiance values are calculated as an average from the string-pairs closest to the respective 4 weather stations. High irradiance is measured between 7:00 to 16:00. Lower irradiance represented by dark patches is measured after sunrise and before sunset. Lower GHI is experienced in the winter months, June-August, with shorter duration of daylight. To maximise the reliability of the data analysis, the operational time is chosen for the ground-mounted system to be between 7:00 to 16:00.

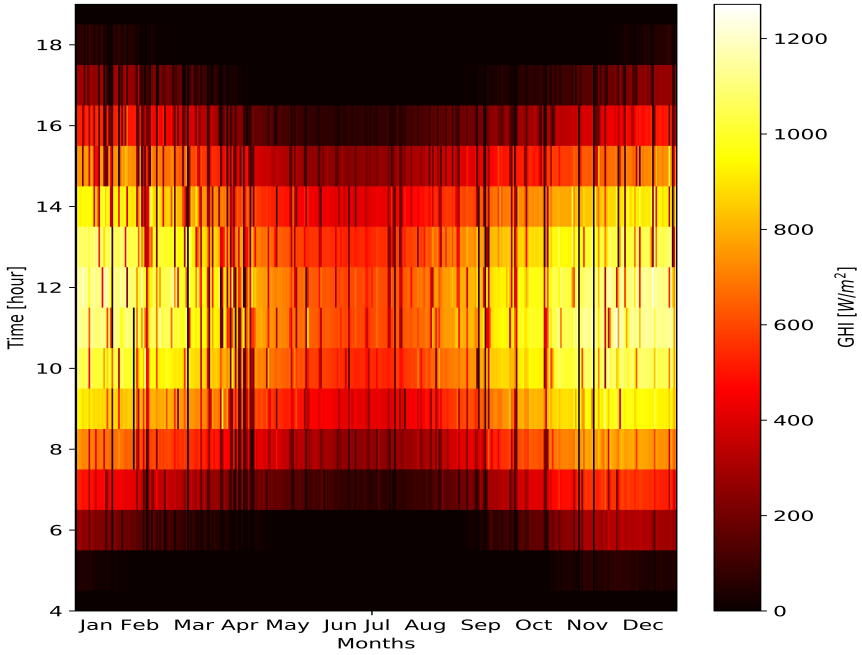

Figure 4.43: Heat map of Kalkbult solar power plant.

Figure 4.44 shows the monthly accumulated measured global horizontal insolation for each of the given weather stations. Highest accumulated insolation is experienced in the summer month, December.

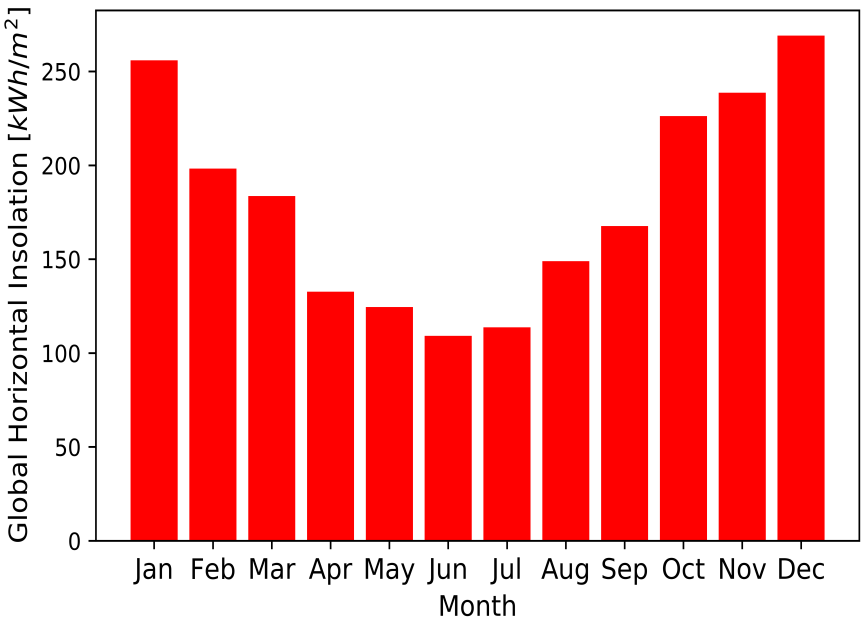

Figure 4.44: Monthly accumulated global horizontal insolation for the Kalkbult solar power plant.

Figure 4.45 shows the monthly accumulated measured global horizontal insolation for each of the given weather stations from January to December for the operational time between 7:00 to 16:00. Since all the weather stations are situated at the same location, the irradiance experienced should be equal. However, the measured solar radiation at the string-pairs of the respective weather stations slightly differs for the given months. The difference in irradiance experienced at the weather stations could occur due to inactive or improper functioning of the data logger or instrumentation.

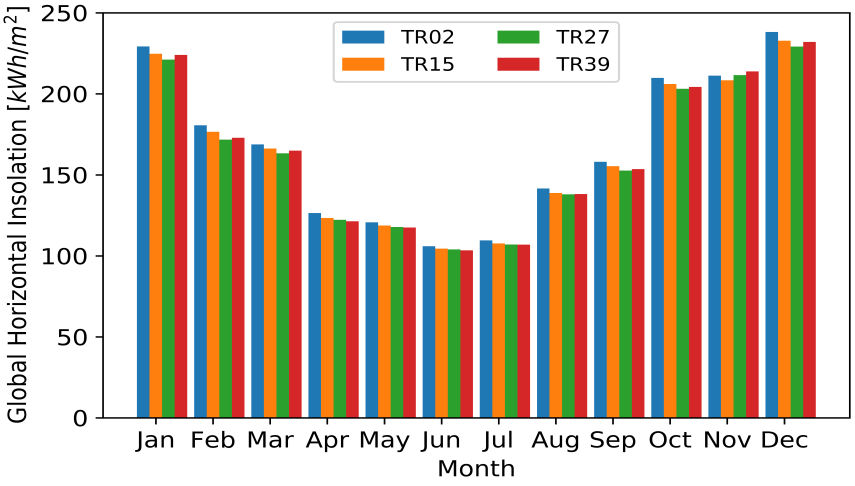

Figure 4.45: Monthly global horizontal insolation received at the ground-mounted system.

4.4.2 Power

Since the heat transfer coefficient of the ground-mounted PV system is only determined for the string-pairs closest to the weather stations, only the string-level data is acquired for evaluation. Therefore, only the measured DC current is available at the string-pair level and no AC power output data was used. Since each string-pair consists of two parallel PV module strings, the voltage readings are equal for the string-pairs that are connected to the same inverter. The DC output power, P_{DC} at string-level pairs is calculated using the inverter DC voltage and the string-pair DC current readings of the PV-module strings closest to the weather station as follows:

$$P_{DC} = V_{DC} \times I_{DC}. \tag{4.4.1}$$

Whereby, V_{DC} and I_{DC} is the voltage and current readings for the DC-side, as directly measured from the PV modules.

Figure 4.46 shows the measured instantaneous power from May 2015 to December 2015. The average power values are calculated as an average from the 4 weather stations, i.e $((P_{TR02} + P_{TR15} + P_{TR27} + P_{TR39})/4)$, whereby P_X represents the measured GHI at the given weather stations. The maximum recorded DC output power is 12.34 kW.

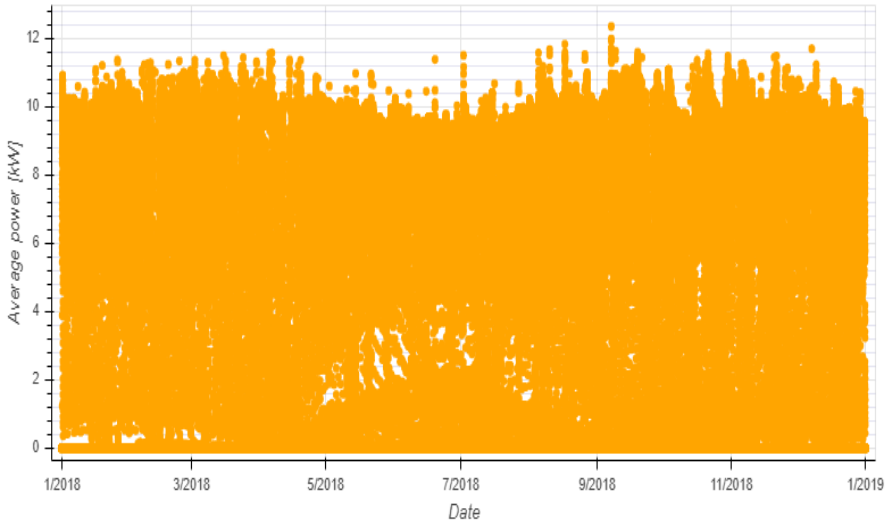

Figure 4.46: Average DC output power at the ground-mounted system.

Figure 4.47 shows the total hourly DC output power of the single string-pair closest to the weather stations for the months, May to December for the operational time between 7:00 to 16:00. For very low irradiance the inverter will operate outside the MPPT interval, thus affecting the system performance. A linear relationship is observed, as expected, between the hourly DC power output for the given months and the irradiance level. The higher the incoming irradiance, the greater the output current, thus, the greater the power produced.

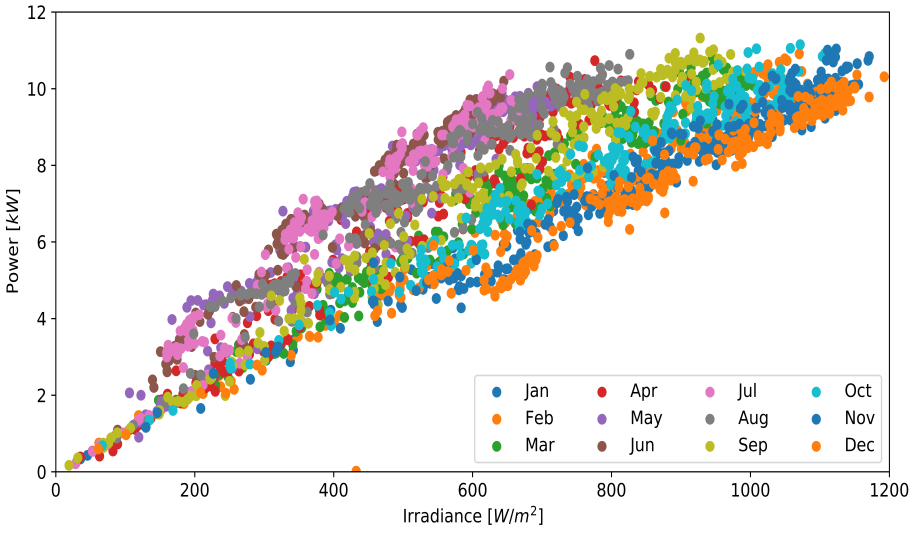

Figure 4.47: Total hourly DC power output for given months.

4.4.3 Air and Module Temperature

Due to the accumulated heat energy in the PV cells, the module temperature is raised. However, the extremely high surface temperature of solar panels is also not desirable as solar panel efficiency declines. Figure 4.48 presents instantaneous air and module temperature. For illustration purposes, only the TR27 weather station's air and module temperature is given in Figure 4.48, while the air and module temperature comparison of the other weather stations reflects the same. Important to note the measured module temperature is higher than the ambient temperature, as expected.

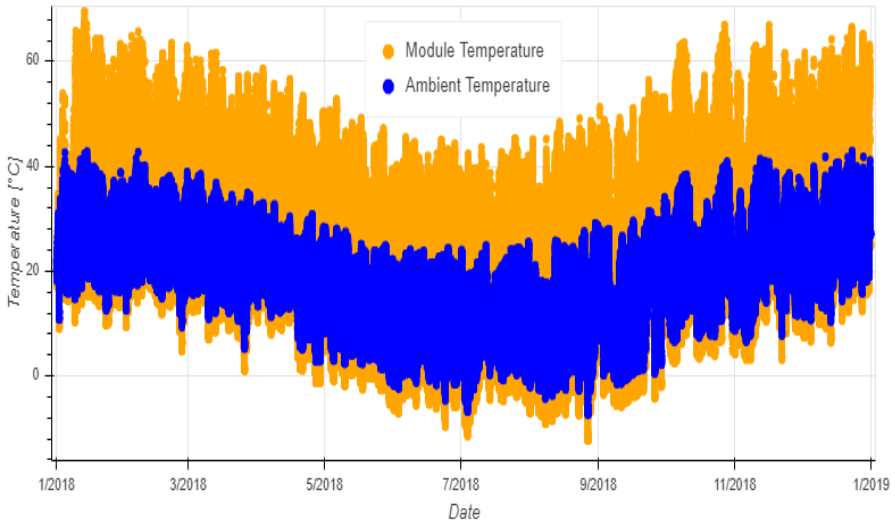

Figure 4.48: Air and module temperature.

By evaluating the hourly distribution of the different month's data at given irradiance level, the variation of the air and module temperature can be identified. Figures 4.49 and 4.50 presents the hourly distribution of the air and module temperature relative to the irradiance level, respectively. The measured ambient temperature shows more fluctuation as the irradiance increases. As the irradiance levels increase the air and module temperature also increases, as expected.

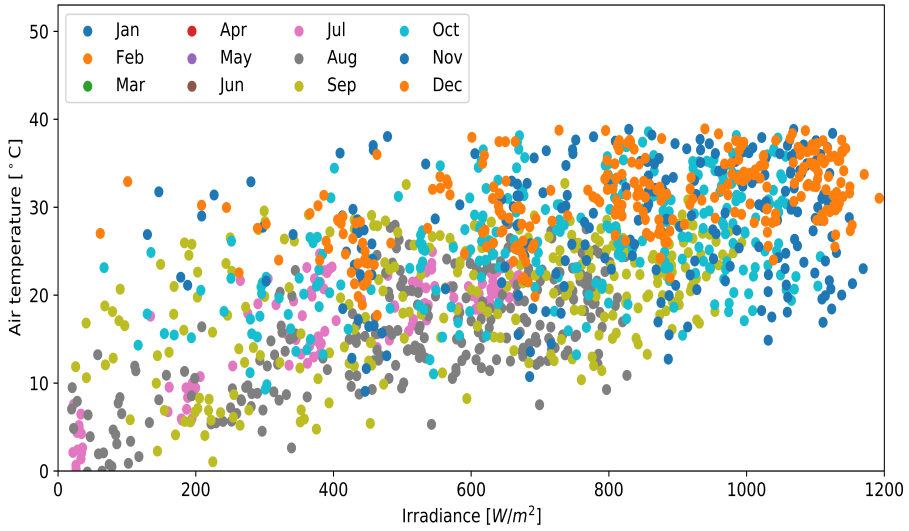

Figure 4.49: Total ambient temperature with variation in irradiance.

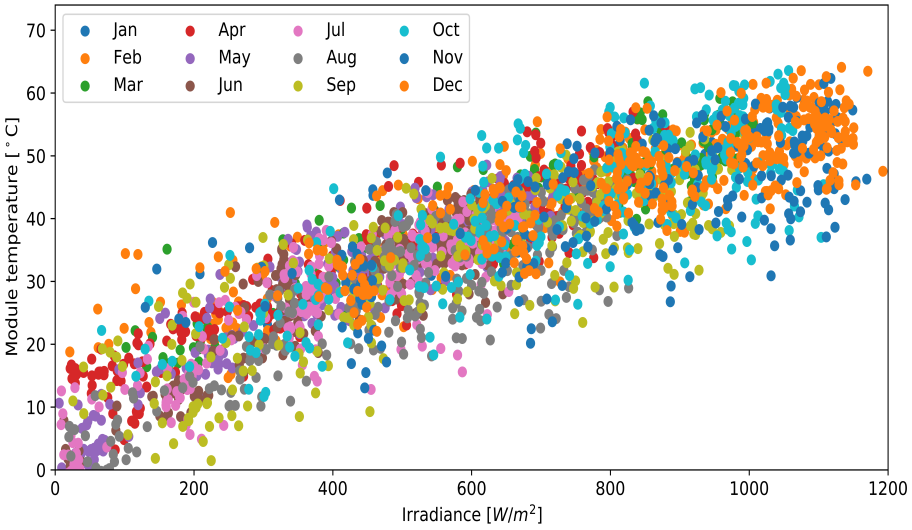

Figure 4.50: Total module temperature with variation in irradiance.

To evaluate the data under observation and outliers in the datasets, a box plot is created for the distribution of air and module temperature for the respective weather stations. Figure 4.51 shows the distribution and the density of outliers of the air and module temperature for the given weather stations. Any observations outside the minimum and the maximum point of observation of the air and module temperature are considered to be the outliers which are represented by the red diamond shapes for each of the given weather stations. The air and module temperature data in the observation are positively and negatively skewed, respectively.

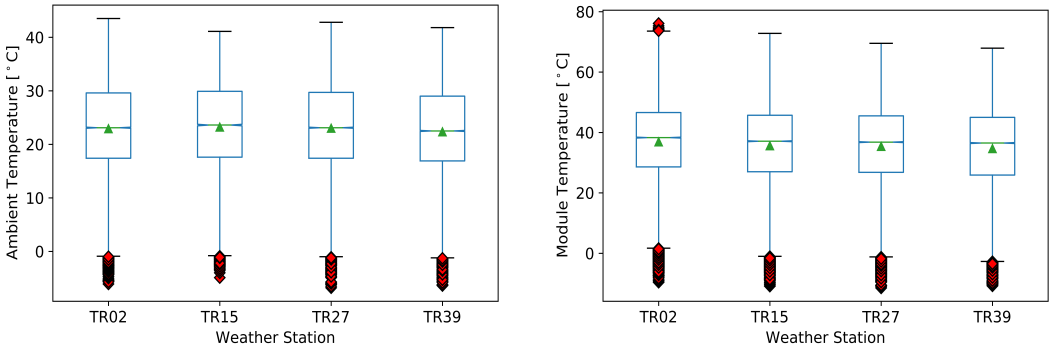

(a) Ambient temperature. (b) Module temperature.

Figure 4.51: Box plot of air and module temperature.

Since PR indicates the 'quality' of the system and does not give information about the performance itself, therefore, the PR of the ground-mounted PV system at the string-pair level of each weather stations is not determined. And also the PR of the ground-mounted PV system is not comparable to the FPV system due to the available AC power for the FPV system and the DC power at the ground-mounted system.

4.5 Summary

In this chapter, a detailed analysis of two different PV systems, FPV and ground-mounted PV system is conducted. The measured data from the two FPV strings, the water-cooled string and the air-cooled string, were analysed. For the ground-mounted PV system, the measured data from the single string-pair closest to the weather stations, TR02, TR15, TR27 and TR39, were analysed. Initially, the system type is introduced and the instrumentation set-up is briefly provided. The data acquisition process and the data cleaning method is discussed. The following parameters are analysed: irradiance, power production, water and air temperature, and the back-surface module temperature.

All the measured data with a five-minutes interval from the FPV system is analysed for the two FPV strings for the period 01 April 2019 to 30 September 2019. Performance analysis of an air-cooled string and a water-cooled floating PV string is conducted. Upon analysis, it was concluded that the water-cooled string performs between 3.17 % to 7.32 % better than the air-cooled string, for irradiance greater than 200 W/m^2. As expected, a linear relationship was observed between the irradiance level and the output AC power of the FPV strings. The measured air temperature at the FPV site showed more fluctuations as the irradiance level increased. The measured water temperature at the FPV site remained more constant throughout the irradiance level in

comparison to the ambient temperature. The PR of both the FPV strings is determined using the standard 'un-corrected' PR and also the temperature corrected PR, PR_{corr}. It was found that even after using the temperature corrected PR, the performance due to seasonal changes were not suppressed. The PR of the water-cooled string is found to be higher than the air-cooled string. The average temperature corrected PR for the water-cooled and the air-cooled string was found to be 0.97 and 0.92, respectively, for irradiance greater than 200 W/m^2. The average performance values of the FPV strings were found to be very high, especially in the Nordic context. The higher PR values are due to the fact that the FPV system is relatively a small system, with shorter cables. Thus, indicative to presume that the net system losses are small and the cooling effect is favourable considering the climatic conditions in Norway. The PR of both the FPV strings were also not the same, as there is a discrepancy present in some measurements. Therefore, it is recommended that further research should be conducted to correct the PR for temperature and also to ensure the calibration of measuring equipment.

All the measured data with a five-minutes interval from the ground-mounted PV system is analysed for the 4 weather stations for the period 01 January 2018 to 31 December 2018. It was observed that the measured GHI at the string-pairs of the respective weather stations were slightly different. The difference in irradiance experienced at the weather stations could have occurred due to inactive or improper functioning of the data logger or instrumentation. As expected, a linear relationship was observed between the irradiance level and the output DC power of the ground-mounted string-pairs. The measured air temperature at the ground-mounted PV system showed more fluctuations as the irradiance levels increased. As the irradiance levels increased the air and module temperatures also increased, as expected. The PR of the ground-mounted PV system at the string-pair level of each weather stations were not determined. The PR of the ground-mounted PV system is not comparable to the FPV system due to the available AC power for the FPV system and the DC power at the ground-mounted system.

Chapter 5

Heat Transfer

This chapter provides detailed information about the approximations used to evaluate the heat transfer coefficient for a floating solar PV system and a ground-mounted PV system. The temperature data logging and retrieval from the floating PV site are explained. The application of the clear-sky filter and data cleaning process is explained. The module temperature is analysed and the cell temperature estimation is presented. Finally, the heat loss coefficient is determined for the two different solar PV systems, and a comparison is made to evaluate the differences in the heat loss for an FPV system vs. a ground-mounted PV system. PVsyst simulation software is also used to investigate the effect of the heat loss coefficient, U-value, on the annual energy yield. PVsyst simulation is also conducted to understand the influence of the tilted panels at various tilt angles on the energy yield of the FPV system using the default albedo value of 0.2 vs. the modelled albedo value of 0.02.

5.1 Heat Transfer Process

The heart of solar PV systems is the solar PV cells. The photovoltaic effect is the foundation of the working principle of solar PV cells. Solar PV cells are capable of converting sunlight into electricity. The cells capture the light which may reflect, transmit, or absorb light through a given surface. When a PV module gets exposed to sunlight, depending on the PV cell technology used, the PV cell typically converts around 20-40 % of the incoming sunlight into electrical energy to generate electricity, of which the remaining energy is converted into heat [145], [146]. The amount of electricity produced is dependent on the type of cell material, cell technology, cell size and the intensity of the sunlight. The conversion process of the incoming sunlight into electrical energy is known as the photovoltaic effect. The photovoltaic effect is defined as the generation of a potential difference at the junction between two layers of semiconductor material in response to electromagnetic radiation [50]. The

photovoltaic effect relates to the photoelectric effect which is explained by Albert Einstein [50].

Packets of energy called photons enter the cells which excite the electrons present in the semiconducting materials. Under the right conditions, the cells convert the absorbed sunlight into electrical current when the electrons flow into the conductive carriers which effectively stimulates the photovoltaic effect. The operating temperature of the solar cell plays an important role in the photovoltaic conversion process. The electrical efficiency and the output power of a PV module are linearly dependent on the operating cell temperature [147]. The solar cell temperature is greatly dependent on the heat transfer effect which is described through the conduction, radiation and convection processes [148], [149], [150].

5.1.1 Conduction

Conduction is the process which is defined as the transfer of heat due to collision between neighbouring atoms or molecules [148]. The conductive heat loss occurs due to thermal gradients between two surfaces such as the PV module and the surrounding atmosphere [148]. The energy is transferred from a more energetic particle to a less energetic particle between layers of substances [148].

5.1.2 Convection

The initial transfer of heat between the object and the fluid substance is through conduction, but the transfer of the bulk of the heat is due to the motion of the fluid. Convection is the transfer of heat due to the movement of molecules between a solid surface and a liquid or gas in motion that is adjacent to the solid surface [149]. There are two types of convection, namely natural and forced convection which is defined by the motion of the fluid that is influenced either by natural means or external means, respectively [149]. Natural or 'free' convection is caused due to the buoyancy forces in which the motion of the fluid generates a change of density that is stimulated by the temperature variations when the fluid is heated [149]. Forced convection is caused when the motion of the fluid is generated due to the external sources such as a pump, or a fan [149]. The heat transfer in forced convection is affected due to external factors. In PV modules, the convective transfer of heat is caused due to the movement of the wind across the surface of the PV modules.

5.1.3 Radiation

Radiation is defined as the transfer of heat to the surrounding environment from an object such as the Sun. It is the emission of high-energy particles in the form of electromagnetic waves [150]. The intensity of the radiation is largely

dependent on the temperature and emissivity. The net radiative losses of a PV module is the difference between the heat transferred from the surrounding environment to the PV module and vice versa. For horizontally mounted PV modules, only the top surface of the PV module is largely exposed to the incoming radiation as the radiation from the sides of the module is negligible due to the small surface area.

Figure 5.1 illustrates the heat transfer processes on a floating PV module. The front glass experiences the incoming radiation from the open environment. The front glass and the back glass together with the EVA experiences conduction. The front-side and the rear side of the PV module is exposed to the air convection and water surface convection, respectively. Heat is also transferred from the rear side of the PV module to the canvas/water.

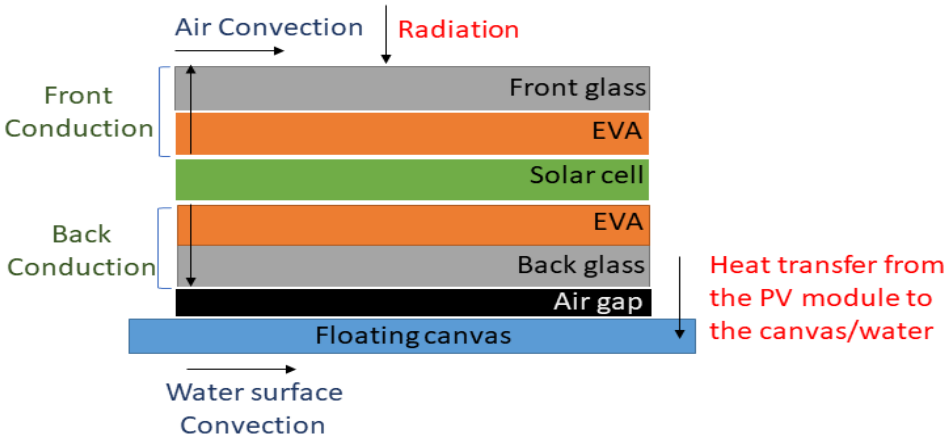

Figure 5.1: Heat transfer on an FPV module.

5.2 FPV system

5.2.1 Retrieving temperature data from Skaftå

The back-surface module temperature data is logged by a 4-channel temperature data logger from Madgetech with a resistance temperature detector (RTD), as previously described in Chapter 4, subsection 4.1.2.5. The logger box is attached on top of the pump system at the floating PV system, as previously shown in Figure 4.6, Chapter 4, subsection 4.1.1. The logged back-surface module temperature has to be retrieved manually from the data logger by utilising the Madgetech 4 software. The temperature data are downloaded as a .zip-archive containing files with comma-separated values (CSV). All the datasets are logged with a five-minute interval.

5.2.1.1 Back-surface module temperature

The back-surface module temperature measurement is available for the period 05.02.2019 to 30.06.2019. However, the sensor box data, irradiance, wind speed, air and water temperature, only started logging on 12 March 2019, as mentioned previously in Chapter 4, subsection 4.1.3. Therefore, the back-surface module temperature data measurements for the period 14.03.2019 to 30.06.2019 is evaluated.

Attachment of the four temperature sensors (RTD1, RTD2, RTD3, RTD4) on the water-cooled string and the air-cooled string was distributed as follows:

- RTD2 and RTD3 on the water-cooled string.
- RTD1 and RTD4 on the air-cooled string.

5.2.2 Data Cleaning

To avoid uncertainties in the evaluation of the heat transfer study, the retrieved back-surface module temperature data parameters from the floating PV system are thoroughly evaluated for every timeframe, identifying NaN values and missing data values. Timestamps for the period 14.03.2019 to 30.06.2019 with at least 1 NaN value is identified. After evaluation, the logged back-surface module temperature datasets did not have any NaN values present.

From the initial attachment of the four temperature sensors (RTD1, RTD2, RTD3 and RTD4) on the rear-side of the 4 PV modules, as previously described in Chapter 4, subsection 4.1.2.5, only 3 temperature sensors (RTD1, RTD, RTD3) remained active for the duration of the period, 30.06.2019. While RTD4 became inactive on 26.02.2019 at 14:05. From 20.04.2019 to 23.04.2019, the remaining temperature sensors (RTD1, RTD2 and RTD3) all were inactive. Inactiveness of the temperature sensors was identified by the logged back-surface module temperature values which abruptly changed and ranged between -192 $°C$ and -243 $°C$. Such temperature values for a module surface is not expected and unreasonable. The inactiveness of the temperature sensor could have been caused due to improper functioning of the data logger, temperature sensors or due to the mechanical stress on the PV module from the windy environment which stimulates a wavy water-surface condition. Therefore, detaching the sensor from the PV module. Reinforcement of the sensors using duct tape might not have been the best solution after all.

To clean the measured back-surface module temperature datasets, undesirable values were identified and dropped. The back-surface module temperature of the air-cooled string is extracted from the logged temperature values from

RTD1. And the average back-surface module temperature of the water-cooled string was calculated as $(RTD2 + RTD3)/2$.

5.2.2.1 Clear-sky Filter

The heat transfer models are usually used for steady-state conditions, which is not the case for solar PV plants with continuously changing irradiation. Therefore, to avoid times with large fluctuations in irradiation and to eliminate the outliers, a clear-sky filter is applied to the irradiance measurement from the floating PV system. A clear-sky filter helps to identify the smallest deviation in the irradiance dataset. The clear-sky filter is applied in pvlib python using the built-in '*pvlib.clearsky.detect_clearsky*' method [151]. This method detects the periods of clear sky irradiance in time series of GHI measurements through an algorithm developed by [152]. By statistical comparison of an expected clear-sky time series and a measured time series, the algorithm detects the clear-sky times through an iterative process. This method simulates a clear sky GHI using the Ineichen-Perez clear sky model [113]. The Ineichen-Perez clear-sky model estimates the clear-sky GHI using the floating PV site location which has an altitude of 32 m.

The clear-sky method can be applied to an entire day or to shorter periods. To classify a time period as clear, the following criteria are applied to the clear-sky filter [152]:

- Maximum value of GHI;
- Mean value of GHI;
- Standard deviation of the rate of change in GHI;
- Length of irradiance vs. time curve;
- Maximum difference between changes in GHI and clear sky time series.

To determine the clear-sky GHI from the measured GHI dataset, the clear-sky times are identified by setting criterion parameters to the algorithm. These criteria are unique to every individual irradiance dataset which needs to be detected for clear-sky times. The input criterion parameters are iteratively selected until all the datasets are successfully evaluated for clear times. Figure 5.2 presents the flow diagram used to detect the clear-sky times.

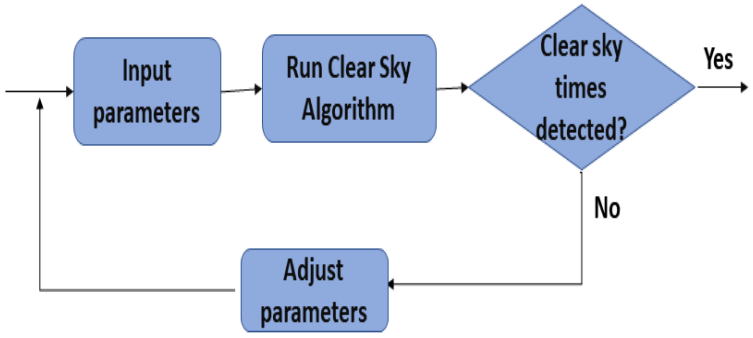

Figure 5.2: Flow diagram for the detection of clear time.

The criterion parameters are defined and set as follows for the measured irradiance at the FPV site:

- Mean interval = 5 minutes. This is the average frequency interval of the dataset.
- Window length = 60 minutes. This is the length of the sliding time window in minutes.
- Mean difference = 100. This is the threshold value for agreement between the mean values of the measured GHI and the clear-sky in each time interval [151].
- Maximum difference = 100. This is the threshold value for agreement between the maxima of the measured GHI and the clear-sky in each time interval [151].
- Lower line length = -125. This is the lower limit of the line length. This criterion is satisfied with lower line length < line length difference < upper line length [151].
- Upper line length = 125. This is the upper limit of the line length. This criterion is satisfied with upper line length > line length difference > lower line length [151].
- Variable difference = 0.025 Hz. This is the threshold value for the agreement between normalized standard deviations of the rate of change in the irradiance.
- Slope deviation = 2.39. This is the threshold value for agreement between the largest magnitude of change in successive values.
- Maximum iterations = 50. This is the maximum number of times the algorithm must apply a different scaling factor to the clear-sky and to redetermine the clear-sky time [151].

Figure 5.3 illustrates the clear-sky GHI which is detected using the algorithm. The measured GHI data are for the late winter/spring and early summer season in Norway. Which means that observing full day clear-sky times in the fjords is limited. As evident, the clear-sky times identified are very little, with few intermittent clear-sky days and most clear-sky times detected after sunrise and before sunset.

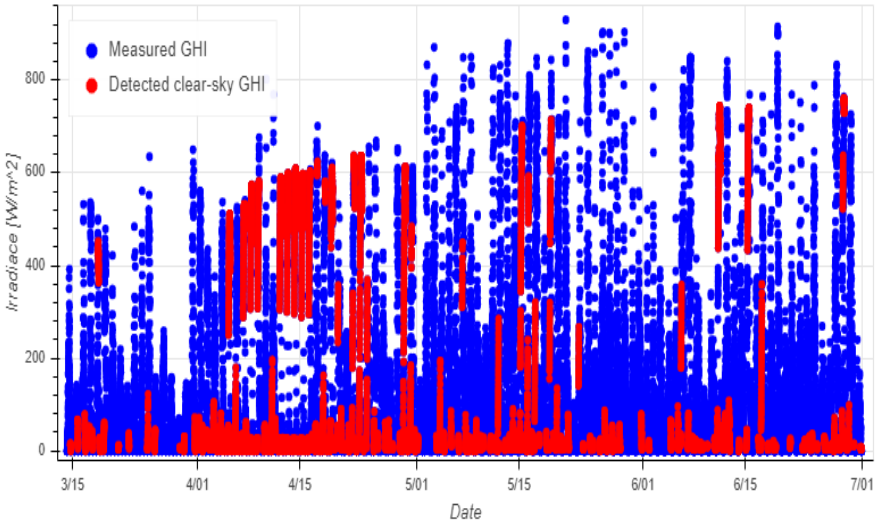

Figure 5.3: Detected clear-sky GHI.

Continuous clear-sky time is identified in April for the unshaded operational time period, 8:00 to 13:00, at the floating PV site. Figure 5.4 presents the identified 7 clear-sky days. These detected clear-sky days are now used to determine the heat-loss thermal coefficient or 'U-value' for the floating PV strings as described in Section 5.4.1.

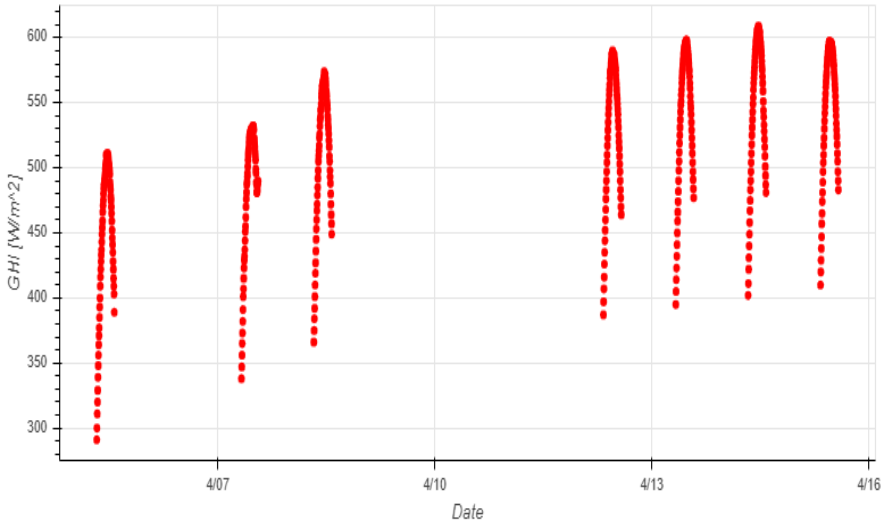

Figure 5.4: Identified clear-sky days.

5.2.3 Data Analysis

To evaluate the heat transfer effect of the floating PV systems, the available data from Ocean Sun's pilot project is used as previously well described in Chapter 4. All mathematical calculations and measured data are analysed using Python with the data analysis Pandas library, and matplotlib and Bokeh visualization libraries through an open-source Jupyter Notebook for interactive computing and data visualization.

5.2.3.1 Back-surface module temperature

Figure 5.5 presents the instantaneous back-surface module temperature of the floating PV strings with a five-minute interval. The inactive period of the temperature sensors from 20.04.2019 to 23.04.2019 is evident. Over the entire period of evaluation, the average back-surface module temperature of the water-cooled string and the air-cooled string is 10.20 $^{\circ}C$ and 11.06 $^{\circ}C$, respectively. From Figure 5.5, the back-surface module temperature of the water-cooled string is lower than the air-cooled string. Therefore, indicating that the cooling of the water-cooled string modules is more effective due to the direct thermal contact of the canvas with the water-surface. Elevated module temperatures are not desirable as it reduces the energy yield and therefore is a major loss factor for PV systems.

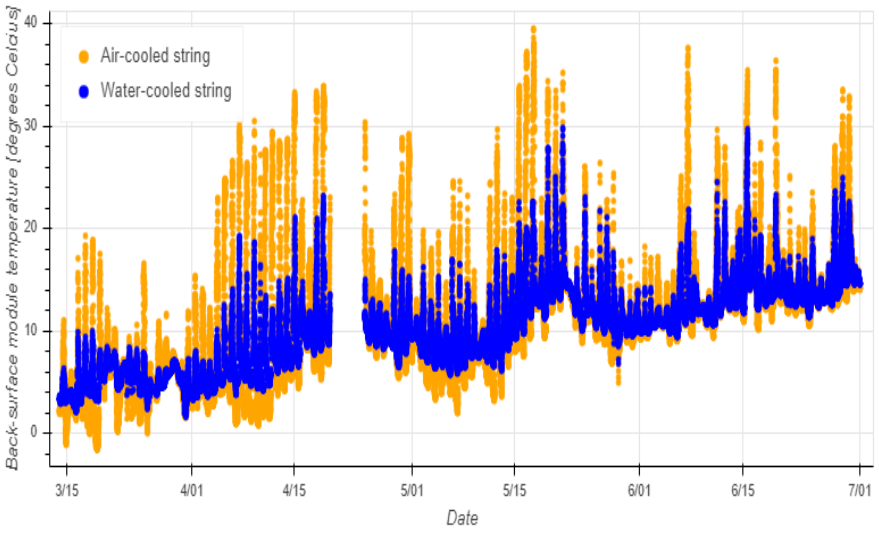

Figure 5.5: Back-surface module temperature of the floating PV strings.

Figure 5.6 illustrates the instantaneous back-surface module temperature difference of the floating PV strings with a five-minute interval. The back-surface module temperature difference, T_{diff_mod}, is calculated as:

$$T_{diff\_mod} = T_{mod\_AC} - T_{mod\_WC}. \tag{5.2.1}$$

Whereby, T_{mod_AC} and T_{mod_WC} is the back-surface module temperature of the air-cooled string and the water-cooled string, respectively. The maximum and the minimum back-surface module temperature difference is 19.31 $^{\circ}C$ and $-5.38^{\circ}C$, respectively. Which means that at a maximum, the back-surface module temperature of the air-cooled string is 19.31 $^{\circ}C$ higher than the water-cooled string.

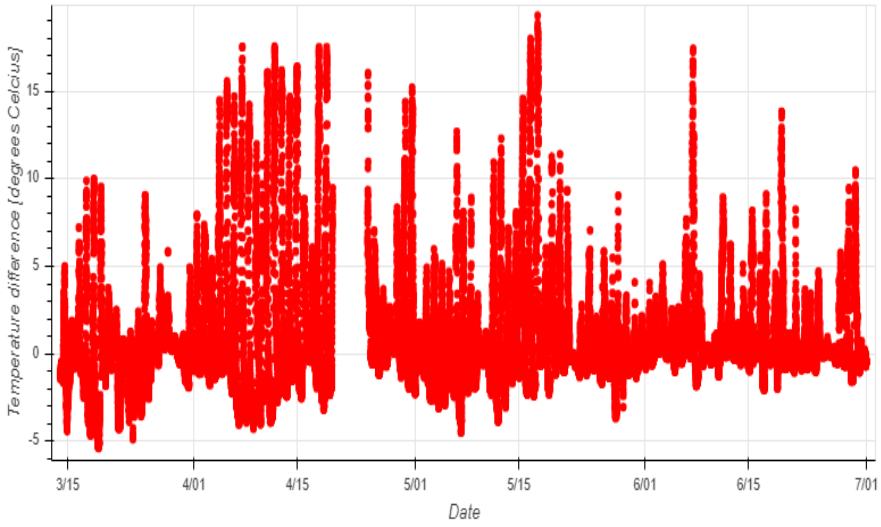

Figure 5.6: Back-surface module temperature difference of the floating PV strings.

Figure 5.7 presents the instantaneous temperature difference between water and the water-cooled string, and air and the air-cooled string.

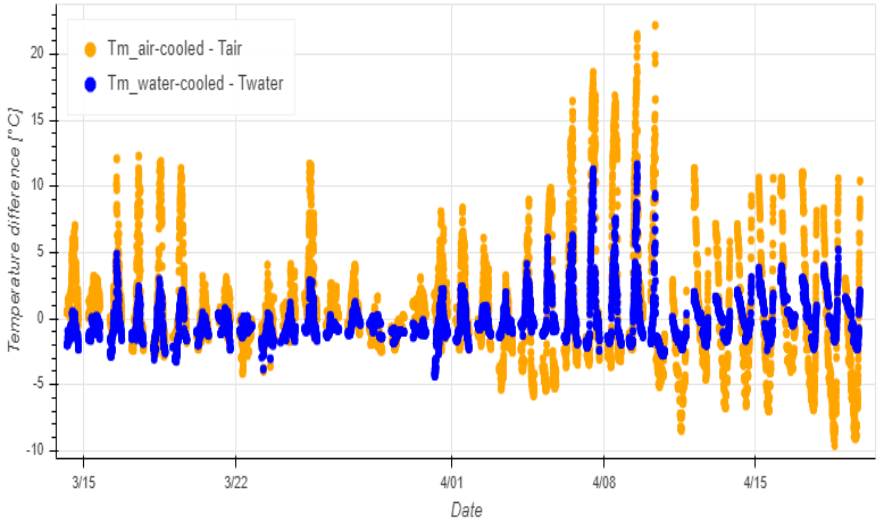

Figure 5.7: Temperature difference between water and the water-cooled string, and air and the air-cooled string.

It is evident that the temperature difference between the back-surface module temperature of the water-cooled string ($T_{m\_water-cooled}$) and the water temperature (T_{water}) is smaller than the temperature difference between the back-surface module temperature of the air-cooled string ($T_{m\_air-cooled}$) and the air temperature (T_{air}). Therefore, it is not only the cooler water temperatures

that provide lower operating module temperatures. But, it is also the more efficient heat transfer between the modules and the surroundings, i.e. water and air, which provides lower operating module temperatures. A greater heat transfer means that water is a better absorber of heat than air. Thus, Ocean Sun's FPV technology will have a greater cooling effect due to the direct thermal contact of the PV modules with the floating canvas on the water surface.

For a better visual representation of the module temperature of both the floating PV strings, IR-pictures were also taken to illustrate the effect of thermal contact with the water surface and the lifting of the PV modules. Figure 5.8 illustrates the IR images of the module temperature difference between the two FPV strings. The pictures were taken by representatives at Ocean Sun using a Mavic Enterprise Dual FLIR Camera on 17 April 2019. The images were taken with the total power production at approximately 4.6 kW and under good operating conditions.

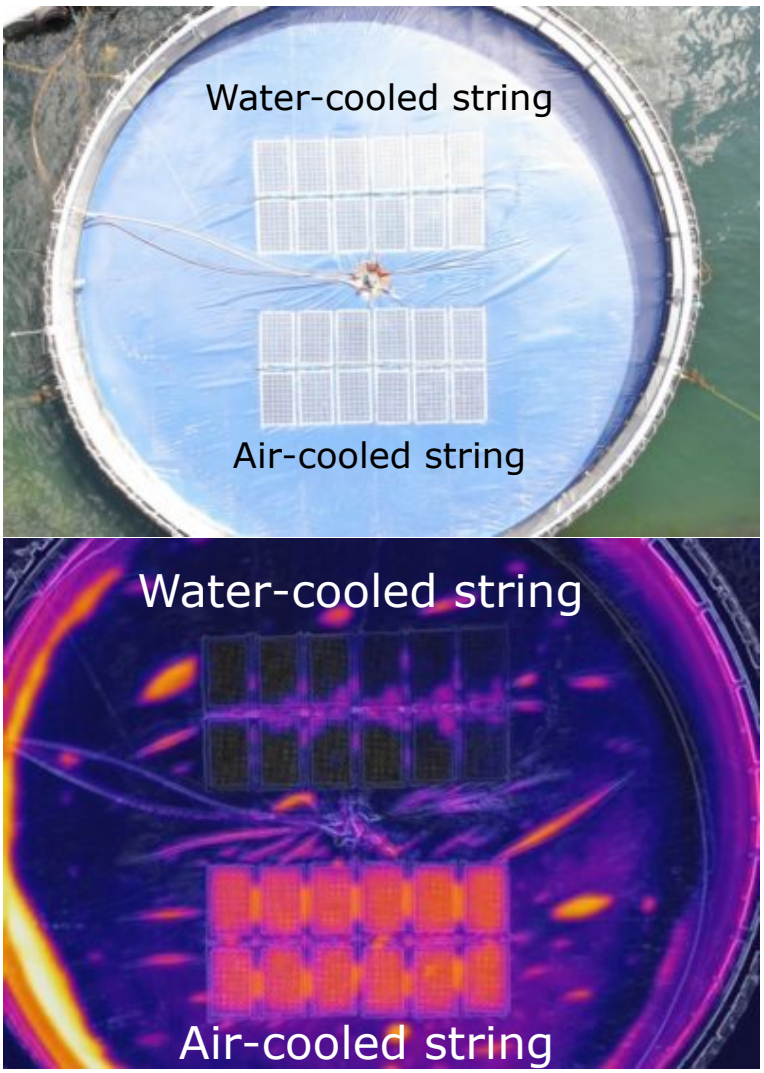

Figure 5.8: IR pictures of the floating PV system [45].

The 'water-cooled' string with the PV modules in direct thermal contact with the floating canvas is depicted on the top. The elevated or 'air-cooled' string with an air gap between the PV modules and the floating canvas is depicted to the bottom. The IR images in Figure 5.8 does not include a temperature measurement scale. The graphical display illustrating the effect of thermal contact with the water surface shows that the water-cooled string does, in fact, have a lower operating module temperature in comparison to the air-cooled string. Interesting to visualise how the water-cooled string adapts to the floating canvas/water temperature. It is also possible to identify hot spots of the junction boxes and the cables. No other indications of faulty PV modules are observed.

Figure 5.9 presents the instantaneous back-surface module temperature together with the irradiance and the temperature difference for the clear-sky

days of the floating PV strings. The back-surface module temperature of the water-cooled string and the air-cooled string is denoted by T_{mod_WC} and T_{mod_AC}, respectively. The temperature difference, $T_{air} - T_{water}$, is the difference between air and water temperature. As expected, the back-surface module temperature for both the floating PV strings are high in the middle of the days due to high irradiance, and the back-surface module temperature of the water-cooled string is lower than the air-cooled string, as expected.

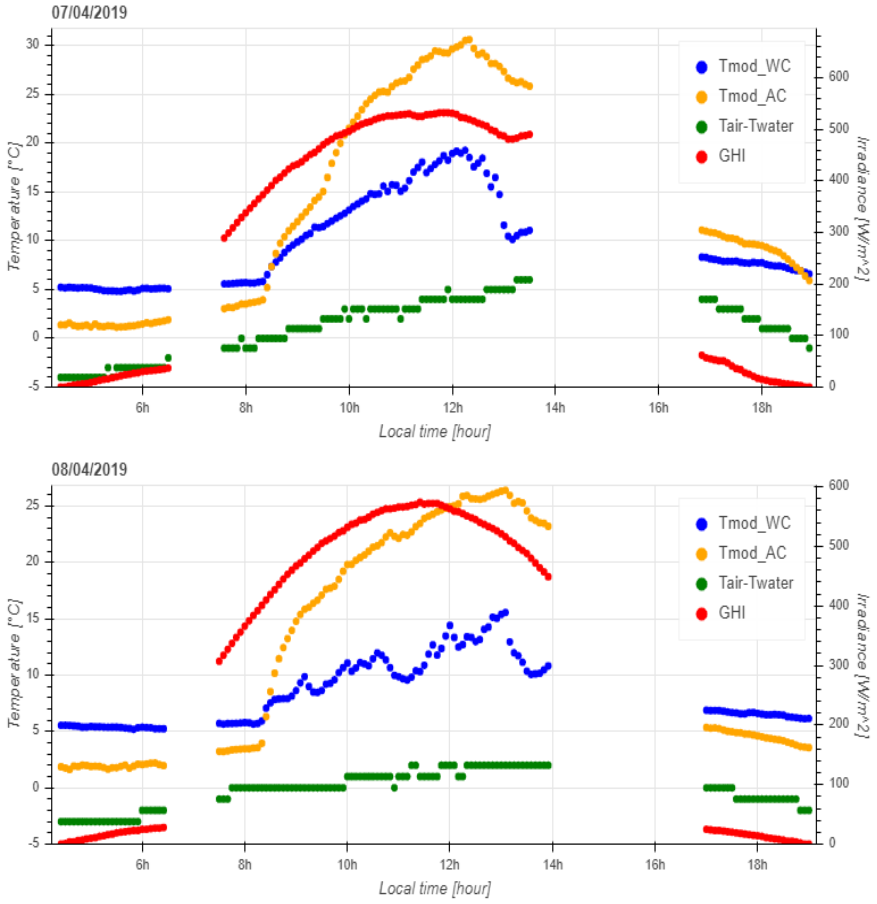

Figure 5.9: Back-surface module temperatures of the clear-sky days.

Under high irradiance, the temperature difference is larger since the air temperature is higher than the water temperature. The temperature difference is also higher at higher irradiation due to increase in cell temperature. Since the water is colder than the air at higher irradiance, the back-surface module temperature of the water-cooled string is lower in comparison with the air-cooled string. This is evident in both the clear-sky days presented in Figure 5.9. The back-surface module temperature of the water-cooled string is lower than the air-cooled string just after sunrise and before sunset, as the irradiance and the

ambient temperature gradually increases.

At higher irradiance and ambient temperatures, the semiconductor closer to the back-surface glass layer of the glass-glass frameless PV modules of the water-cooled string gets cold due to the lower water temperatures. The module temperature of the water-cooled string is affected by the water temperature. Therefore, heat flow is faster due to the thermal contact of the PV modules with the canvas on the lower water temperature surface. The PV modules of the air-cooled string absorb thermal energy which elevates the module temperature. The same happens to the water-cooled string, however, the PV modules lose the heat again to the floating canvas/water which acts as a heat sink. Water is a good heat sink under higher irradiance because it has a higher heat capacity and thus higher absorption of thermal energy.

At lower irradiance, the ambient temperature drops lower than the water temperature. Since the water is warmer than the air at lower irradiance, the back-surface module temperature of the water-cooled string increases in comparison to the air-cooled string. This is due to the decrease in the temperature difference between air and water temperature at night. This is evident in both the clear-sky days presented in Figure 5.9. Whereby, the back-surface module temperature of the water-cooled string is higher than the air-cooled before sunrise and after sunset, and also just after sunrise and before sunset.

The back-surface module temperature of the water-cooled string fluctuates less than the back-surface module temperature of the air-cooled string. This is due to the fact that the back-surface module temperature of the water-cooled string is regulated by the water temperature and the water temperature remains more consistent while the ambient temperature fluctuates as shown previously in Chapter 4, Subsection 4.2.2.3.

Figure 5.10 presents the instantaneous back-surface module temperature for some clear-sky days of the floating PV strings. Interesting to observe that the back-surface module temperature of the water-cooled string is presented to be higher than the air-cooled string. This phenomenon occurs when the water temperature is higher than the ambient temperature during daylight under higher irradiance since water has a higher heat capacity than air. This situation is particularly frequent in colder temperatures at higher latitudes, whereby the water surface may get frozen. Thus, liquid water will be warmer than air. The PV modules therefore do not get hot enough and the module temperature does not reach higher than the ambient temperature. The semiconductor closer to the back-surface glass layer of the elevated PV modules gets cold due to the lower temperature difference between air and water at high irradiance. The glass layer removes the heat flow faster, thus, the back-surface module temperature of the air-cooled string remaining lower than the

water-cooled.

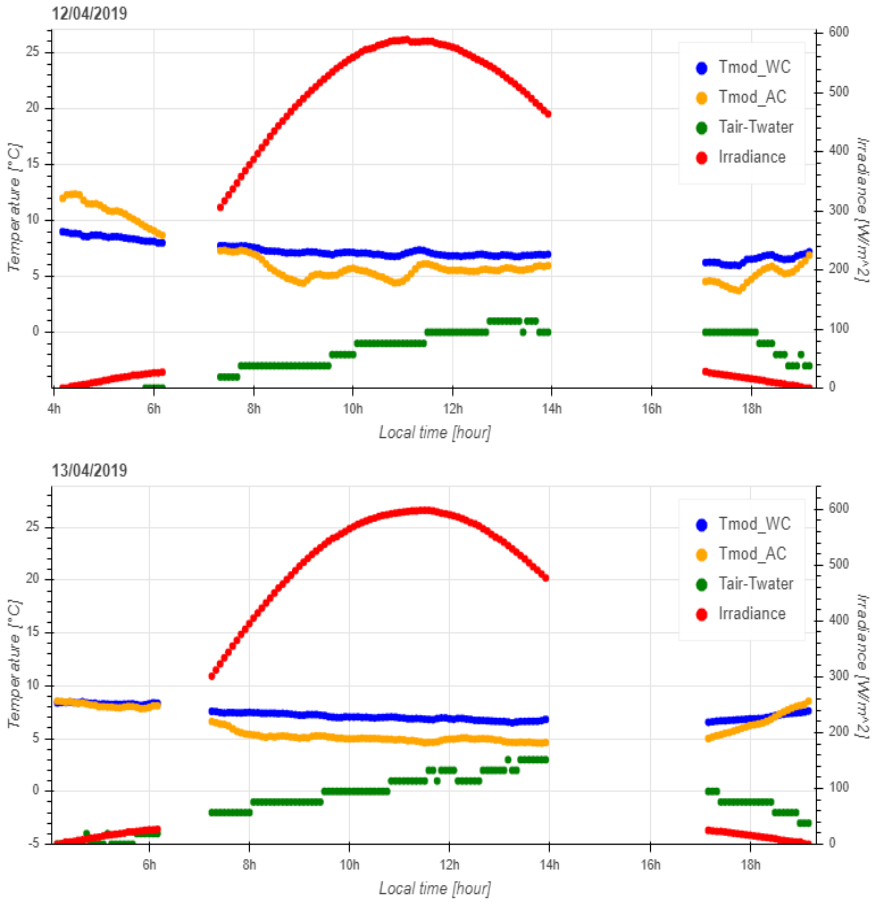

Figure 5.10: Back-surface module temperature difference of the floating PV strings.

It is also possible that since lower temperature difference between the air and water temperature is experienced under higher irradiance, the air-cooled string experienced light frost on the elevated PV modules, as previously shown in Figure 4.8, Chapter 4, subsection 4.1.1. Therefore, the accumulated frost lowers the module temperature of the elevated string in comparison to the water-cooled string.

At night, the temperature difference between the air and water increases as the water temperature is higher than the air temperature. Therefore, resulting in a higher back-surface module temperature of the water-cooled string as shown before sunrise and after sunset in each of the clear-sky days in Figure 5.10.

5.3 Cell Temperature Estimation

The operating cell temperature of a PV module is the temperature of the solar cell. The cell temperature is an important parameter in determining the solar panel efficiency and output power. In the absence of operating cell temperature measurement, it is crucial to determine the appropriate estimation of the cell temperature. There are various different models used to estimate the cell temperature [153], [154], [155]. The models are generally derived from climatic data such as global solar irradiance, ambient temperature, and wind speed.

The cell temperature is defined by the heat generation and loss mechanism of a PV module. Dependent on whether the back-surface module temperature measurement is available or not, the cell temperature can be estimated using two different approaches. If the back-surface module temperature measurement is unknown, the Nominal Operating Cell Temperature (NOCT) estimate is commonly used. The NOCT method is briefly described previously in Chapter 4, subsection 4.2.3.

Alternatively, if the back-surface module temperature measurement is available, the cell temperature, T_{cell}, can be estimated using the following expression [156]:

$$T_{cell} = T_m + \frac{G_T}{G_{T\_STC}} \times \triangle T. \tag{5.3.1}$$

Where T_m is the measured back-surface module temperature in $°C$, G_T is the solar radiation striking the PV array in W/m^2, and G_{T_STC} is the reference solar irradiance at Standard Test Conditions (STC) defined as 1000 W/m^2. $\triangle T$ is the change in temperature difference between the cell temperature and the back-surface module temperature which is expressed as:

$$\triangle T = T_{cell} - T_m. \tag{5.3.2}$$

Since the back-surface module temperature measurement of both the FPV strings, the water-cooled (WC) string and the air-cooled (AC) string, is available from the floating PV system, the cell temperature approximation for both the strings is expressed as follows:

$$T_{cell\_WC} = T_{m\_WC} + \frac{G_T}{G_{T\_STC}} \times \triangle T, \tag{5.3.3}$$

$$T_{cell\_AC} = T_{m\_AC} + \frac{G_T}{G_{T\_STC}} \times \triangle T. \tag{5.3.4}$$

Whereby, T_{cell_WC} and T_{cell_AC} is the cell temperature of the water-cooled string and the air-cooled string, respectively. T_{m_WC} and T_{m_AC} is the measured back-surface module temperature of the water-cooled string and the

air-cooled string, respectively.

In approximating the cell temperature of both the floating PV strings, the back-surface module temperature and the global solar irradiance are the two parameters which remain fixed depending on the measurements. The only challenge now remains is the correct estimation of $\triangle T$. Table 5.1 shows the $\triangle T$ for different module and mounting type.

Table 5.1: Change in temperature difference for different module and mounting type [156].

Module type	**Mounting type**	$\triangle T$ [$^{\circ}C$]
Glass/cell/glass	Open rack	3
Glass/cell/glass	Close roof mount	1
Glass/cell/polymer sheet	Open rack	3
Glass/cell/polymer sheet	Insulated back	0
Polymer/thin-film/steel	Open rack	3
22X Linear Concentrator	Tracker	13

Since the water-cooled string modules are directly in contact with the floating canvas, $\triangle T$ is chosen to be estimated as 0 $^{\circ}C$ with insulated back in a well-ventilated condition [156]. Therefore, the cell temperature is equivalent to the back-surface module temperature of the water-cooled string. The cell temperature of the air-cooled string is estimated using $\triangle T$ as 1 $^{\circ}C$, which is the same as a close roof mounting type for a glass/cell/glass module type.

5.4 Heat Transfer Approximations

5.4.1 Heat Loss Factor

By definition, the thermal heat loss factor or 'U-value' is a measurement unit to determine the loss of heat in a PV module. The U-value expresses the effectiveness of a material to act as an insulator. The lower the U-value, the less heat is lost by the PV module, making it more insulated and vice versa. In PV simulation software such as PVsyst, there are various detailed loss factors which are accounted for. One of them is the thermal parameters. The thermal loss factor indicates the behaviour of the array through a thermal balance between the atmospheric environment and the PV module. The thermal balance is the heat loss factor (U), which is expressed as [46]:

$$U = U_c + (U_v \times v). \tag{5.4.1}$$

Whereby, U is measured in units $W/m^2.K$, v is the wind velocity in m/s, U_c is the constant component in $W/m^2.K$, and U_v is the factor proportional to the wind velocity in $W/m^2.K/m/s$.

When reliable measured wind velocity data is not available, PVsyst software proposes default U-values without wind dependency. The following proposed U-values are all defined at zero wind velocity, i.e. $U_v = 0\ W/m^2.K/m/s$:

- 29 $W/m^2.K$, for free-standing systems with air circulation all around the collectors [46].
- 15 $W/m^2.K$, for fully insulated backside and no heat exchange at the backside, i.e. only one side contributes to the convection of heat exchange [46].
- 20 $W/m^2.K$, for intermediary cases, i.e. semi-integration, air duct below the collectors [46].

If reliable measured wind velocity data are available, PVsyst software proposes default U-values with an average wind dependency. For a free-standing system, 25 $W/m^2.K$ and $U_v = 1.2\ W/m^2.K/m/s$ [46]. With an average wind velocity of 3 m/s, a U-value of 28.6 $W/m^2.K$ is proposed [46].

However, the U-value is often used as an equivalent to the constant heat transfer factor U_c since the wind velocity is typically measured to be relatively small. Thus, $U_v \times v$ does not contribute a large amount to the total heat loss factor U. For the FPV system used in this study, the measured maximum velocity is 6 m/s with an average velocity of 0.076 m/s throughout the period which is relatively low. Therefore, the wind dependency of $U_v \times v$ factor is ignored in the calculation.

The following approximation is used for the U-value [46]:

$$U = \frac{\alpha \times G_T \times (1 - n_c)}{T_{cell} - T_{amb}}. \tag{5.4.2}$$

Whereby, n_c is the electrical conversion efficiency of the PV array [%], and α is the absorption coefficient of solar irradiation. The absorption coefficient α is estimated as:

$$\alpha = 1 - albedo. \tag{5.4.3}$$

Albedo is the reflection coefficient. The U-value is not greatly dependent on the absorption coefficient, α, due to extremely lower reflection off the water surface. It is assumed that the back surface of the PV module used for the Ocean Sun's technology will experience a much lower reflection (or almost close

to zero) since the PV modules are fully covered by the canvas.

For conventional PV systems, PVsyst recommends default values of α and albedo to be 0.9 and 0.2, respectively [46]. Therefore, α is used as 0.9 for the U-value approximations. The U-value approximation for the air-cooled, U_{AC}, is expressed as follows:

$$U_{AC} = \frac{\alpha \times G_T \times (1 - n_c)}{T_{cell\_AC} - T_{amb}}. \tag{5.4.4}$$

The U-value approximation for the water-cooled string is evaluated using two different base values, particularly the ambient temperature, T_{amb}, and the water temperature, T_{water}. The U-value approximations for the water-cooled string are expressed as follows:

$$U_{WC\_amb} = \frac{\alpha \times G_T \times (1 - n_c)}{T_{cell\_WC} - T_{amb}}, \tag{5.4.5}$$

$$U_{WC\_water} = \frac{\alpha \times G_T \times (1 - n_c)}{T_{cell\_WC} - T_{water}}, \tag{5.4.6}$$

Whereby, U_{WC_amb} and U_{WC_water} is the U-value approximation using the ambient temperature and the water temperature as the bases, respectively. The U-value is evaluated for these two different bases to show that the cooling effect is in fact due to the water. Ignoring the water temperature in the U-value approximation may underestimate the true functioning of the heat transfer effect for PV modules with direct contact with the canvas/water.

An accurate estimation of the U-value for the Ocean Sun's FPV technology is important as the heat loss factor strongly influences the electrical performance of the technology. The heat loss factor is greatly dependent on the mounting mode of the FPV modules, this includes, sheds, roofing, facade, etc [13]. In terms of the floating PV technology with PV modules directly in contact with the floating canvas, and in comparison to other FPV technologies which uses floats or pontoons, the Ocean Sun's FPV technology, as demonstrated by the water-cooled string, should have a larger U-value in comparison to the air-cooled string. As the thermal contact of the PV modules with the floating canvas for the water-cooled string should provide a much effective cooling effect.

5.4.2 Analysis

Avoiding the shading effect at the floating PV site, the heat transfer approximations for the floating PV strings are evaluated for the duration of the

unshaded operational time from 8:00 to 13:00, as previously described in Section 4, Subsection 4.2.1.1.

Figure 5.11 presents the U-value distribution of the water-cooled and the air-cooled floating PV strings for the given clear-sky days. U_{AC} represents the U-value of the air-cooled string. U_{WC_amb} and U_{WC_water} represents the U-value of the water-cooled string with the ambient temperature and the water temperature as bases for the approximations, respectively. The U-value of the water-cooled string is presented higher than the air-cooled string, as expected. The higher the U-value, the better the cooling effect is. Thus, indicative that the PV modules with thermal contact with the water surface have a better cooling effect. Before 9h the U-value of both the string is noted to be higher in the positive and the negative ranges. These unexpected higher U-values are due to the temperature difference between the cell temperature and the ambient temperature, i.e. when the cell temperature is lower than the ambient temperature, as previously shown in Figure 5.9.

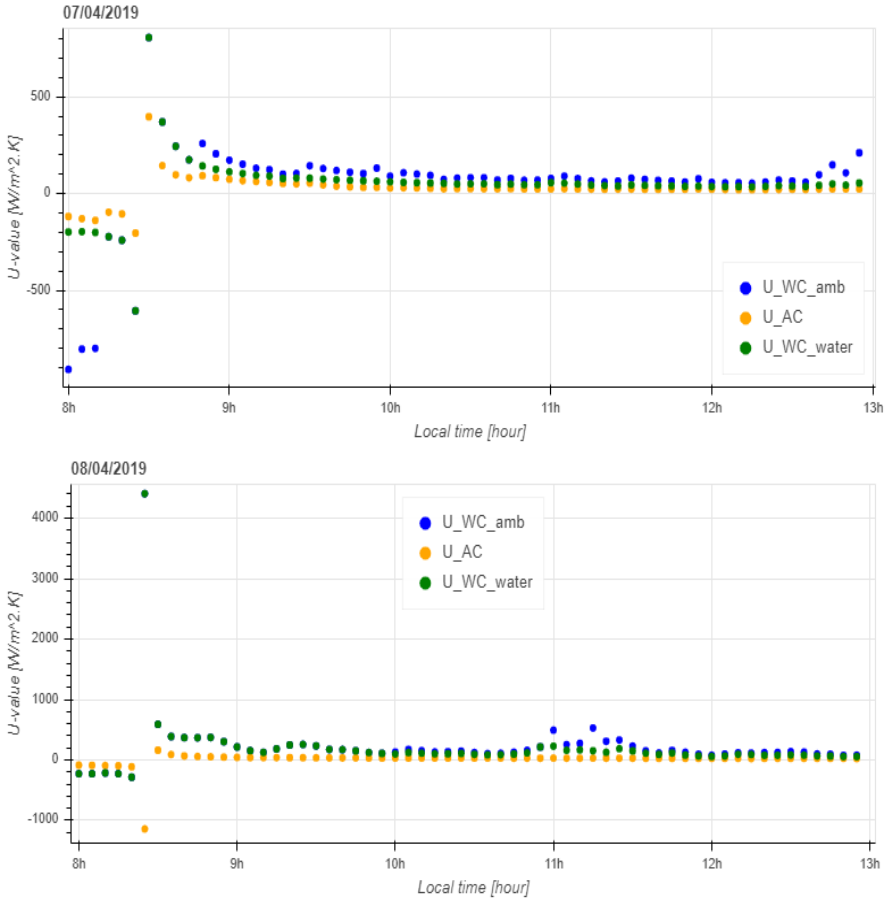

Figure 5.11: U-value distribution of the floating PV strings for the clear-sky days.

When a smaller positive and negative temperature difference between the cell and the ambient temperature is noted, a relatively higher positive and negative U-value is observed. However, when a larger positive and negative temperature difference between the cell and the ambient temperature is noted, a smaller positive U-value is observed, as expected. This abrupt change in the U-value is evident for the clear-sky days shown in Figure 5.12.

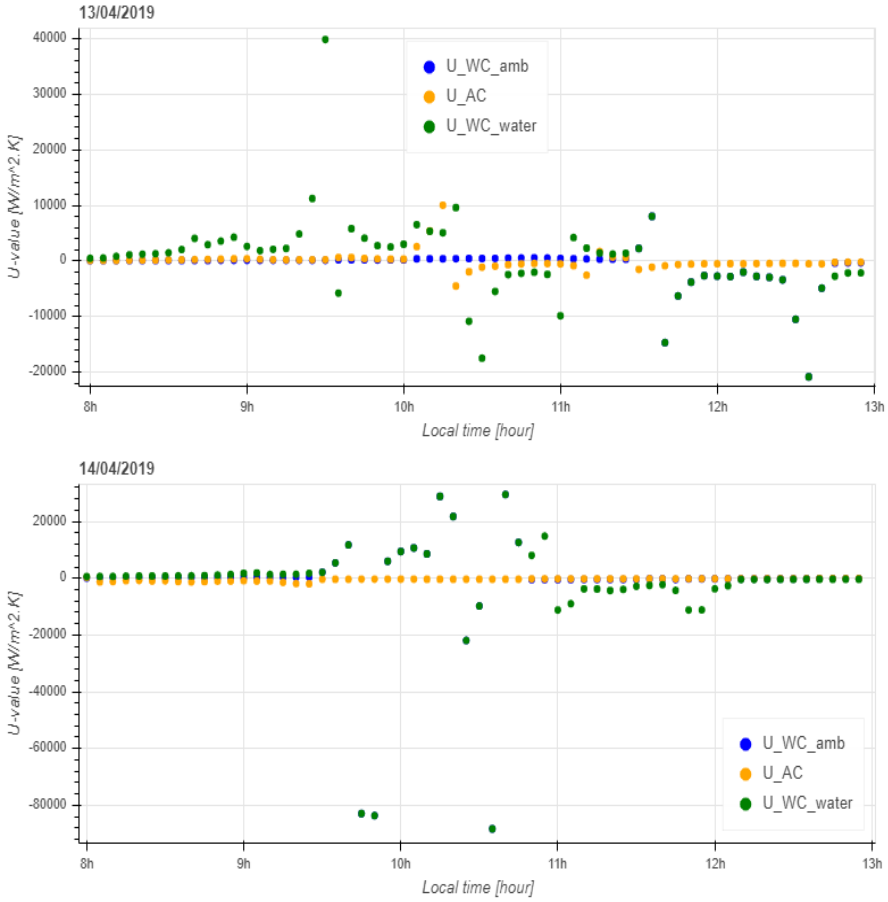

Figure 5.12: Variation of U-value for the clear-sky days.

Since the U-values of the floating PV strings presented for the clear-sky days in Figure 5.11 is more realistic, the 2 clear-sky days, 07.04.2019 and 08.04.2019, will now be further analysed from 9hr to 13hr to make a comparison between the estimated U-values for the water-cooled string and the air-cooled string. Figure 5.13 presents the U-value variation of the floating PV strings for the times 9hr to 13hr. It is observed that the U-value of the water-cooled string, approximated using both the ambient and water temperatures as bases, abruptly changes in comparison to the air-cooled string. Therefore, the U-values of the water-cooled string fluctuates more, while the U-values of the air-cooled string remains consistent throughout the period. As evident, the U-values of the

water-cooled string approximated using the water temperature as the base, is lower in comparison to the U-value approximated using the air temperature as the base.

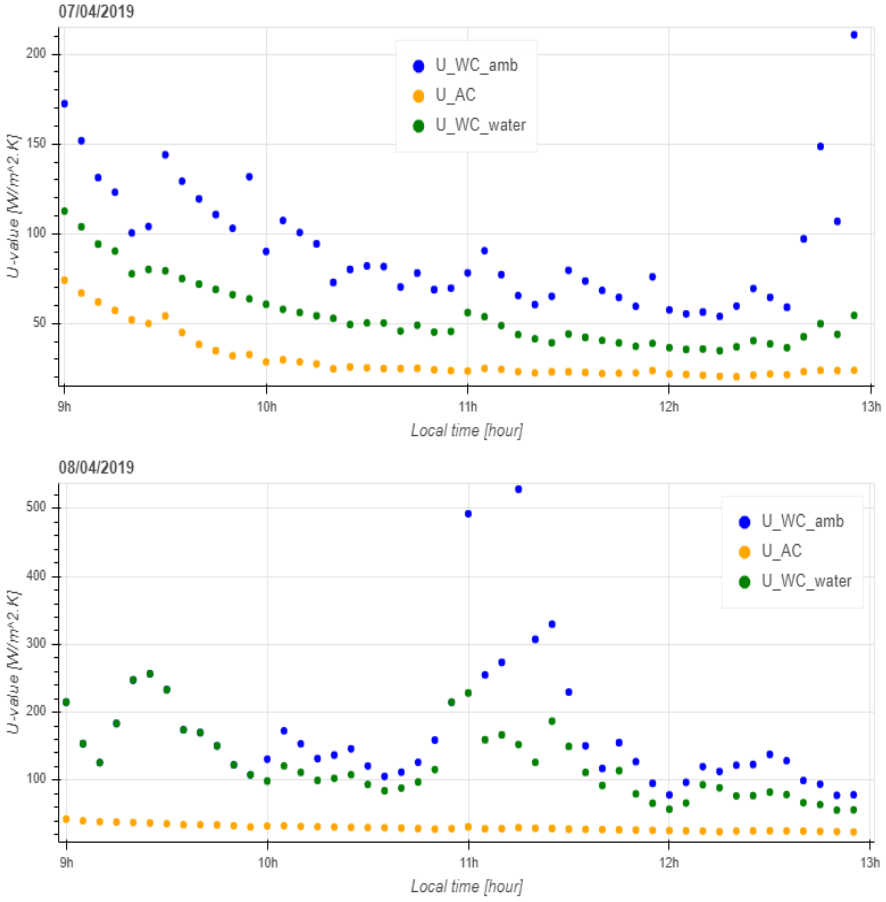

Figure 5.13: U-value distribution of the floating PV strings.

To evaluate the outliers and differences of the U-value for both the floating PV strings, a box plot is created for the distribution of U-value. Figure 5.14 shows the U-value distribution and the density of outliers for the air-cooled string. The U-value distribution is calculated for the clear-sky days as previously shown in Figure 5.13. An average U-value of 30.14 $W/m^2.K$ is recorded for the air-cooled string.

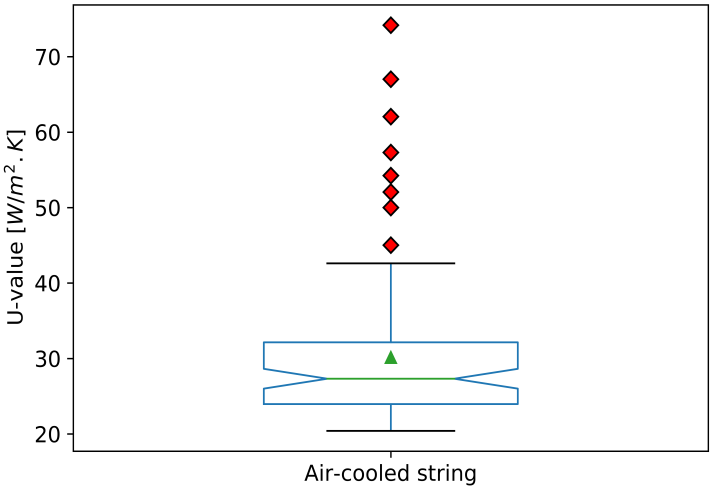

Figure 5.14: Box plot of the U-value distribution of the air-cooled string.

Figures 5.15 shows the U-value distribution and the density of outliers for the water-cooled string. The U-values are approximated using the air and water temperature as the base as previously formulated in section 5.3. The U-value distribution is calculated for the clear-sky days as previously shown in Figure 5.13. Average U-values of 131.23 $W/m^2.K$ and 89.44 $W/m^2.K$ is recorded for the water-cooled string using the ambient temperature and the water temperature, respectively, as the bases for the approximations.

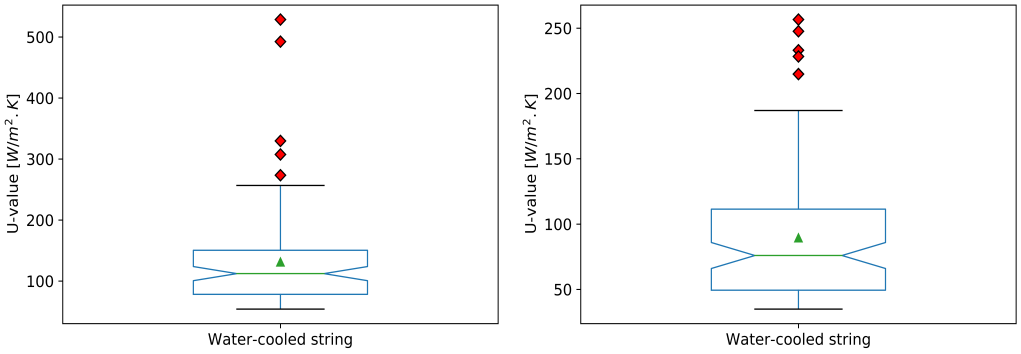

(a) Air temperature as the base. (b) Water temperature as the base.

Figure 5.15: Box plot of the U-value distribution of the water-cooled string.

The average U-value of 30 $W/m^2.K$ of the air-cooled string as shown in Figure 5.14 is close to the PVsyst standard value of 29 $W/m^2.K$ for a free-standing system which has an air circulation all around the collectors [46]. PVsyst proposed default values are without wind dependency, i.e. $U_v = 0$ $W/m^2.K/m/s$ [46]. The average U-value of 89 $W/m^2.K$ of the water-cooled string using water

temperature as the base for approximating the U-value as shown in Figure 5.15 corresponds to a better cooling effect due to the direct thermal contact of the PV modules with the floating canvas on the water surface. Since water is a better absorber than air with efficient heat transportation as previously shown in Figure 5.7, a higher U-value is observed for the water-cooled string. The higher U-values are effective in maintaining lower PV module temperatures which effectively contributes to better electrical performance and vice versa. Interestingly, the U-values observed for the air-cooled string is close to a good heat sink.

5.5 Ground-mounted PV System

To evaluate the heat transfer effect of the ground-mounted PV system, the available data from the Kalkbult's solar power plant is used as previously well described in Chapter 4, Section 4.3. All mathematical calculations and measured data are analysed using Python with the data analysis Pandas library, and matplotlib and Bokeh visualization libraries through an open-source Jupyter Notebook for interactive computing and data visualization.

5.5.1 Clear-sky Filter

To avoid times with large fluctuations in irradiation and to eliminate the outliers, a clear-sky filter is applied to the irradiance measurement from the ground-mounted PV system. The clear-sky detection method as previously discussed in subsection 5.2.2.1 is used. A clear-sky filter helps to identify the smallest deviation in the irradiance dataset. Since the measured GHI is available for all the 4 weather stations, and the GHI experienced at all the weather stations should be the same due to the same location, only the TR02 weather station's GHI is used for detecting clear times at the location. When the criterion parameters of the FPV dataset was applied to the ground-mounted system, the entire new GHI dataset was not detected for the clear-sky times. Since it is a different GHI dataset than the floating PV system, the criterion parameters are re-evaluated and set as follows for the measured irradiance at the ground-mounted PV site:

- Mean interval = 5 minutes.
- Window length = 60 minutes.
- Mean difference = 1000.
- Maximum difference = 1000.
- Lower line length = -2500.

- Upper line length = 2500.
- Variable difference = 0.045 Hz.
- Slope deviation = 48.391.
- Maximum iterations = 400.

The clear-sky filter does not determine the clear times for clear-sky days only but also clear-intermittent, intermittent overcast and overcast days. For illustration purposes, Figure 5.16 shows the clear times detected from the measured GHI for the different day types in April 2018. The detected GHI for the clear times is then manually sorted by day types. Day type classification helps to identify the smallest deviation in irradiance. The day types are classified as clear-sky, clear-intermittent, intermittent and overcast days.

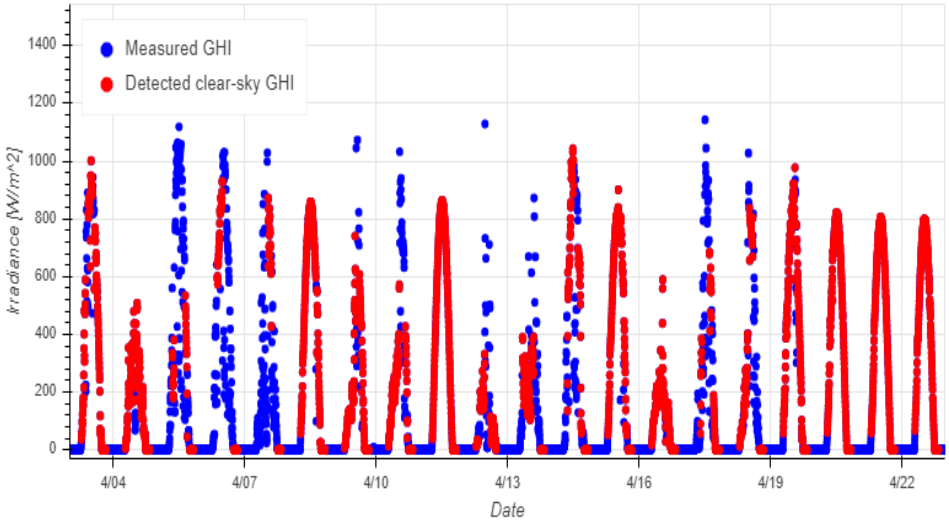

Figure 5.16: Clear times detected from GHI.

To evaluate the heat-transfer effect of the ground-mounted PV system in comparison to the floating PV system, only the classified clear-sky days are used. Evaluating U-values for clear-sky days provides the true functioning of the heat transfer effect under clear-sky conditions and thus providing more realistic observations without cloudiness. Figure 5.17 presents the number of clear-sky days detected for each of the months for the period 01.02.2018 to 31.12.2018. The clear-sky days are extracted from the annual GHI data.

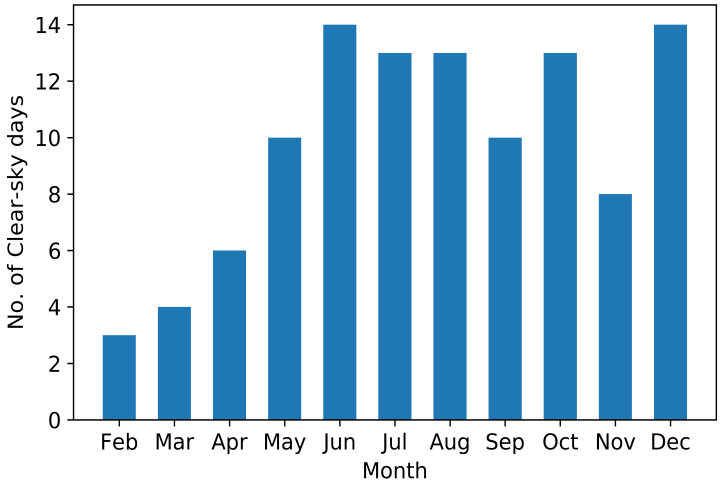

Figure 5.17: Detected clear-sky days at the Kalkbult solar PV power plant for 2018.

The measured module temperature of the string-pairs closest to the TR15 and TR39 weather station is not available for the period 01.01.2018 to 19.07.2018 and 01.01.2018 to 31.01.2018, respectively. Therefore, the U-values are only determined for the string-pairs closest to the weather stations, TR02, TR27, and TR39 for the clear sky days detected, as previously shown in Figure 5.17, for the period 01.02.2018 to 31.12.2018

5.5.2 Cell Temperature

The cell temperature is estimated using the theoretical application as previously described in Section 5.3. Since the back-surface module temperature measurement of the string-pairs closest to the weather stations is available, the operating cell temperature is approximated as follows:

$$T_{cell} = T_m + \frac{G_T}{G_{T\_STC}} \times \triangle T. \tag{5.5.1}$$

Where T_m is the measured back-surface module temperature of each of the respective string-pairs for the given weather stations in $^{\circ}C$, and G_{T_STC} is the reference solar irradiance at Standard Test Conditions (STC) defined as 1000 W/m^2. $\triangle T$ is the change in temperature difference between the cell and the back-surface module temperature which is estimated as 3 $^{\circ}C$ for glass/cell/polymer sheet module with open rack mounting in a well-ventilated condition [156].

By theoretical definition, the cell temperature is expected to be higher than the surface module temperature. In this approximation, the cell temperature will

be estimated to be higher than the module temperature with an addition of a fraction, $\frac{G_T}{G_{T\_STC}} \times \triangle T$. This fraction provides less than 3 $^{\circ}C$ higher estimated cell temperature than the measured module temperature. Figure 5.18 presents the daily average approximated operating cell temperature and the measured module temperature for the TR27 weather stations, while the cell and module temperature comparison of the other weather stations remains true.

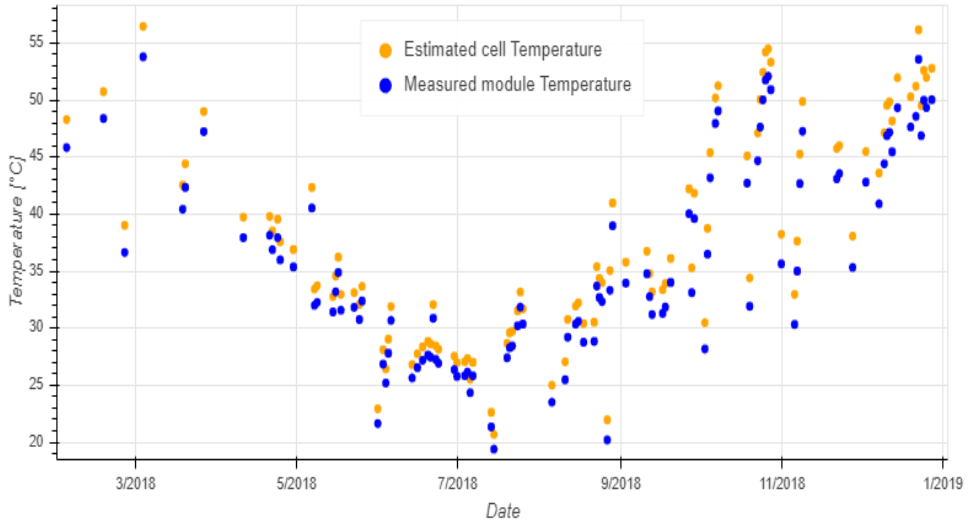

Figure 5.18: Estimated daily operating cell temperature and the measured module temperature.

5.5.3 Heat Loss Factor Estimation

The heat loss factor or 'U-value' is estimated using the theoretical application as previously described in Section 5.4.1. The approximation for the U-value is as follows:

$$U = \frac{\alpha \times G_T \times (1 - n_c)}{T_{cell} - T_{amb}}. \tag{5.5.2}$$

Whereby, n_c is the electrical conversion efficiency of the PV array [%] which is 14.75 % for the specified BYD PV modules, and α is the absorption coefficient of solar irradiation which is typically used as 0.9 for conventional PV systems [46].

Figure 5.19 presents the distribution of the U-values for the given weather stations for the identified clear-sky days for the operational time between 7:00 to 16:00. As evident, the U-values of the given weather stations is noted to be higher in the positive and the negative ranges. These unexpected higher U-values are due to the temperature difference between the cell temperature and the ambient temperature, i.e. when the cell temperature is lower than the

ambient temperature. The large U-values are experienced just after sunrise when the irradiance level is low.

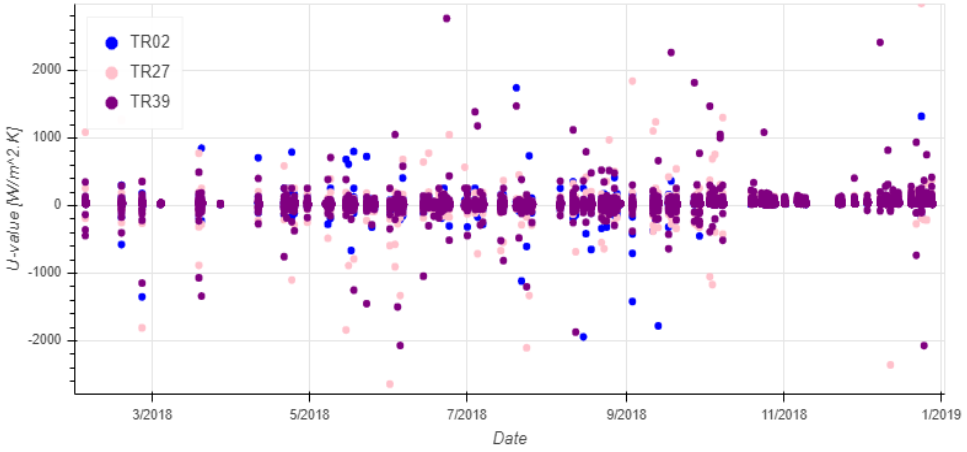

Figure 5.19: U-value for the given weather stations.

Figures 5.20 presents the distribution of the U-values and the temperature difference for the TR02 weather station for a randomly selected clear-sky day, 7 July 2018, for the operational time between 7:00 to 16:00. As evident, the evaluated U-values are large in the positive and negative ranges. When a smaller positive and negative temperature difference between the cell and the ambient temperature is noted, a relatively higher positive and negative U-value is observed. However, when a larger positive and negative temperature difference between the cell and the ambient temperature is noted, a smaller positive U-value is observed, as expected. This abrupt changes in the U-value are evident before 8h for the clear-sky day shown in Figure 5.20. After 8h, the U-value remains consistent in the ranges between 15-25 $W/m^2.K$

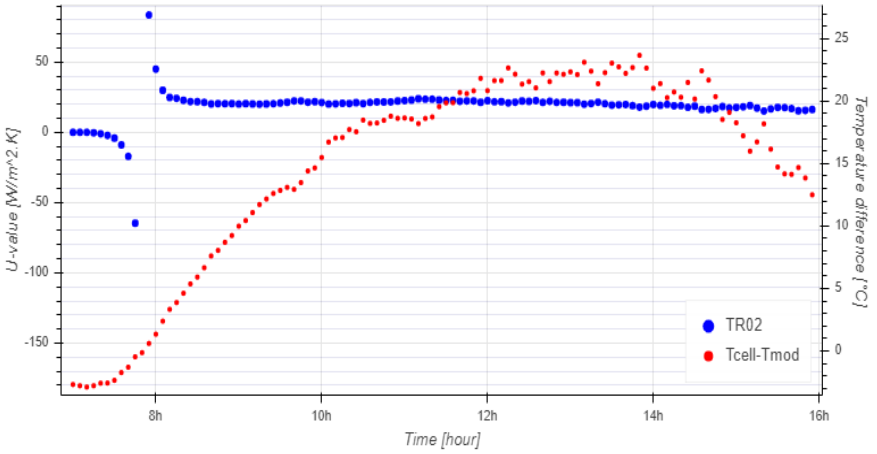

Figure 5.20: U-value distribution for a clear-sky day.

To eliminate the time period of abrupt changes in the U-values for each of the weather station, the U-values are now evaluated for the operational time between 9:00 to 15:00. Figure 5.21 presents the U-value distribution for the respective weather stations for the operational time between 9:00 to 15:00. As evident, the higher ranges positive and negative ranges are eliminated. Therefore, better observation of the U-value can now be conducted.

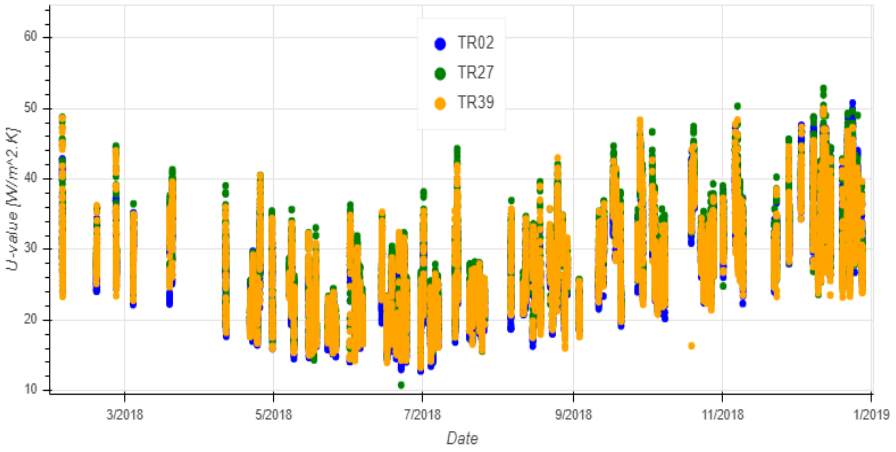

Figure 5.21: U-value distribution for the different weather stations.

Figures 5.22 and 5.23 presents the distribution of the hourly U-values at the given weather stations for the identified clear-sky days, for the operational time between 9:00 to 15:00, relative to wind velocity and for irradiance greater than 200 W/m^2. The TR27 weather station demonstrates higher U-values in comparison to other stations. The U-values for the given weather stations increases with an increase in irradiance and wind velocity.

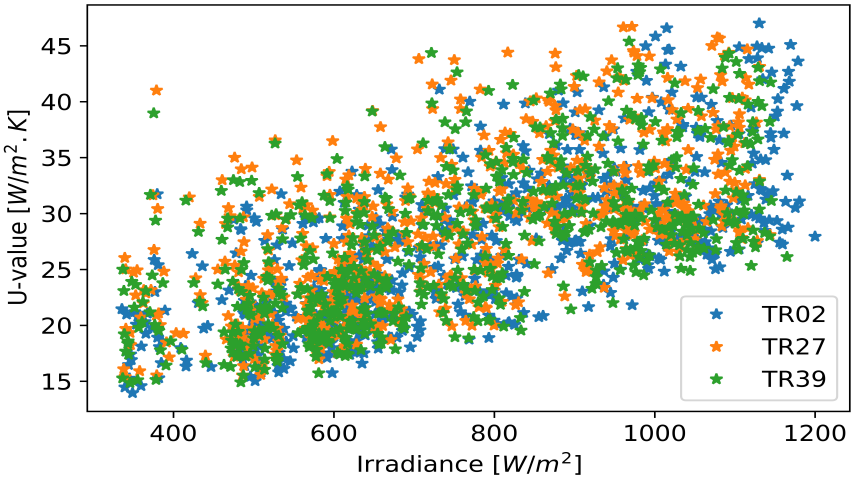

Figure 5.22: U-value distribution relative to irradiance.

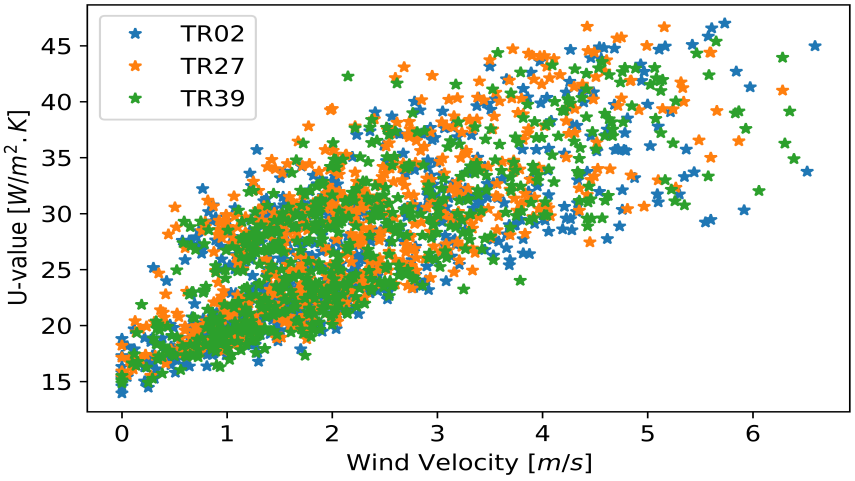

Figure 5.23: U-value distribution relative to wind velocity.

Figure 5.24 presents the box plot distribution of the U-values for the given weather stations for the identified clear-sky days and the operational time between 9:00 to 15:00, for irradiance greater than 200 W/m^2. Any observations outside the maximum and the minimum range are considered to be the outliers which are indicated by the red diamond shapes. The U-value distribution displays positive skewness. The notches in the boxplot indicate the 95 % confidence interval of the median. The median of observation of the given weather stations is within the 95 % confidence interval. The notches indicate how different the median value of each station is.

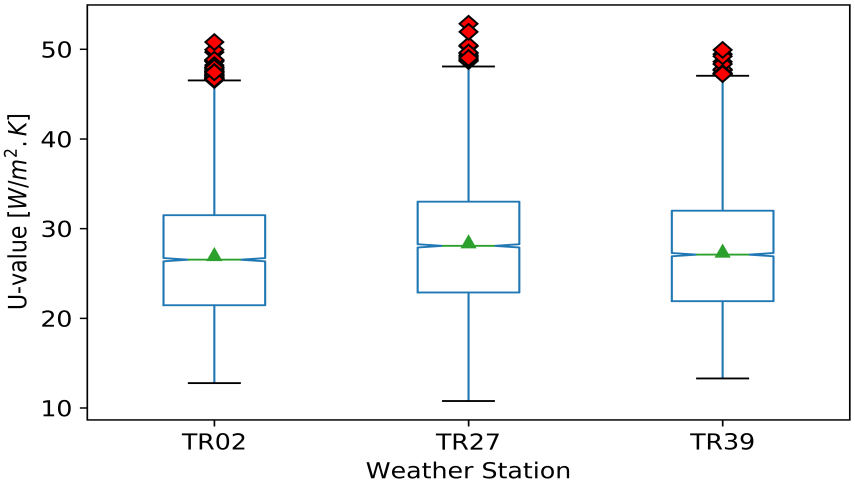

Figure 5.24: Box plot of the U-value for the Kalkbult PV system.

Table 5.2 shows the average mean and the median of the U-values for the given weather stations. The mean and the median values for the given weather stations are relatively close to each other, which indicates that the observation is more or less evenly distributed from the lowest to the highest values. The mean of all the weather stations is 27.70 $W/m^2.K$. The average U-values of the weather stations is close to the PVsyst standard value of 29 $W/m^2.K$ for a free-standing system which has an air circulation all around the collectors [46].

Table 5.2: Mean and median of the U-values for each weather station.

Weather station	**Mean** $[W/m^2.K]$	**Median** $[W/m^2.K]$
TR02	27.10	26.54
TR27	28.52	28.08
TR39	27.49	27.10

Figures 5.25 and 5.26 presents the U-value distribution for the clear-sky days with a resolution of 5 minutes. The corresponding measured module and air temperature are visualized with a colour bar. Lower U-values are observed at the lower module temperatures and ambient temperatures, respectively.

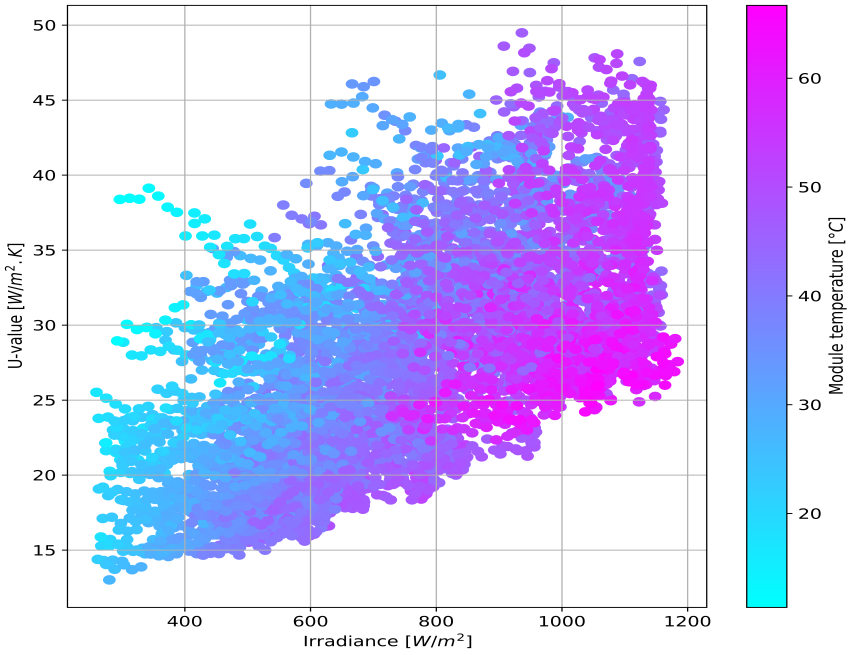

Figure 5.25: Variation in U-values at different module temperatures and irradiance.

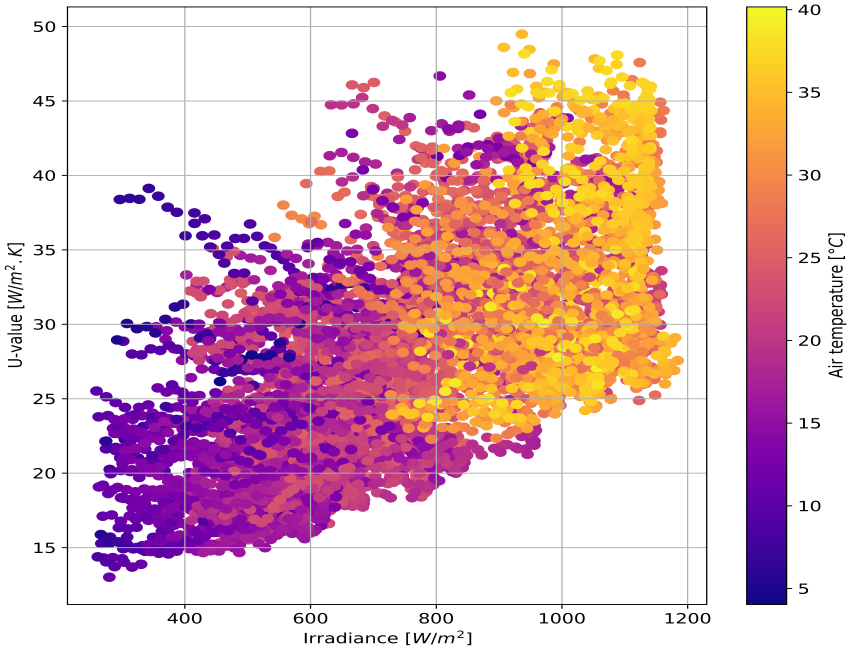

Figure 5.26: Variation in U-values at different air temperatures and irradiance.

5.6 Software simulation

To investigate the effect of the heat transfer coefficient, U-value, on the annual energy yield, a software PV simulation tool, PVsyst, is used. PVsyst is used to simulate the behaviour and the performance of an FPV system. The ability of the PV simulation software to correctly simulate an FPV system is identified. Specifically, the key parameters which need to be altered in order to successfully simulate an FPV system, are determined. This is done by modifying a terrestrial PV system simulation to depict an FPV system, as no software PV simulation tool can simulate floating PV installations (to the author's knowledge).

The two key parameters, albedo and U-value, which are investigated in this research are varied in PVsyst. The proposed default albedo value of 0.2 by PVsyst is initially used as an input to simulate the annual energy yield of an FPV system. The annual energy yield of the FPV system using the default albedo value of 0.2 is then compared to the annual energy yield of the FPV system at a modelled albedo value of 0.02, as previously determined by the water surface albedo model in Chapter 3. The tilt angle is varied from 0° to 60° to understand the influence of the tilted panels on the energy yield of the FPV system using the default albedo value of 0.2 vs. the modelled albedo value of 0.02. The U-value is also varied from 10 $W/m^2.K$ to 100 $W/m^2.K$ for the depicted FPV simulation to investigate the effect of the U-value on the annual energy yield.

5.6.1 PVsyst

PVsyst is a PV software simulation tool used to design, and analyse different configurations of PV technology [157]. PVsyst allows the importation of meteo data, and also allows input of personal data from various different sources [157]. It is a well-known software simulation tool in the PV industry. In this research, PVsyst version 7.1.0 is used. In order to successfully depict a floating PV in PVsyst, only the two key parameters can be altered, albedo and U-value. PVsyst does not have the ability to illustrate the installation of floating PV on the water surface. One project is created for an FPV system, and various variants are simulated for the U-values ranging from 10 $W/m^2.K$ to 100 $W/m^2.K$ with increments of 10 $W/m^2.K$. Each step of the simulation is carefully explained below together with the extraction of meteo data and input of the main parameters.

Site and meteorological file: PVsyst does not have a site available for Skaftå. Therefore, a site was manually created at latitude 60°27'14.4"N and longitude 5°37'19.2"E. This creates an interpolated meteorological data file from Meteonorm 7.3 (1991-2010) with 21 % of the data from satellite data due

to limited ground station data.

Orientation: To determine the annual energy yield of the FPV system using the default albedo value of 0.2 vs. the modelled albedo value of 0.02, the PV modules are mounted at a fixed tilt angles from 0° to 60°. The PV modules are tilted as a horizontally mounted PV module cannot make use of the reflected radiation component. Typically, the optimal tilt angle of PV modules should be equal to the latitude of the relevant location. Since the latitude of the FPV site is 60°27'14.4"N, a tilt angle of 60° is a very inclined surface for PV modules. NREL research has shown that the tilt angle of 11° is the typical mounting angle for floating solar systems [158]. However, the FPV system is simulated at varying tilt angles from 0° tilt to the optimal tilt angle of 60° with increments of 10°. The tilt angles are varied to understand the influence of the tilted panels on the energy yield of the FPV system using the default albedo value of 0.2 vs. the modelled albedo value of 0.02.

To ensure that the solar panels capture the greatest possible amount of solar radiation during the day, the PV modules are faced towards the terrestrial equator. Therefore, the standard convention for the PV module installation in the Southern and the Northern Hemisphere is true North and true South, respectively. Since the FPV installation site is in the Northern Hemisphere, the solar panels are faced directly true South and the collector azimuth angle should equal to 180°. However, in PVsyst the orientation conventions are contrary to the standard convention as follows [159]:

- For Northern Hemisphere, the azimuth is equal to 0° which corresponds to the South. The azimuth is positive towards the West (clockwise angles). Therefore: East = -90°, West = +90°, North = + or -180°.
- For Southern Hemisphere, the azimuth is equal to 0° which corresponds to the North. The azimuth is positive towards West (anti-clockwise angles). Therefore: East = -90°, West = +90°, South = + or -180°

Therefore, the azimuth angle is set to 0° for the FPV simulation in PVsyst to determine the energy yield of the FPV system using the default albedo value of 0.2 vs. the modelled albedo value of 0.02 .

Since Ocean Sun's FPV system consists of the PV modules with thermal contact with the floating canvas on the water surface, the PV modules are positioned with a fixed 0° tilt and 0° azimuth. The azimuth angle of a horizontally mounted PV panel is insignificant.

System: At Skaftå, the PV module used for the FPV system is the 270 W modules from Trina Solar. This particular model type is not available in

the current PVsyst version used for this research. Therefore, the 270 W Trina Solar's PV module had to be manually created in PVsyst. This is done by modifying the 270 W module type from TDSolar. Under the "Basic data" header, parametric input values under the "manufacturer specifications or other measurements" header is modified according to the 270 W Trina Solar's data sheet. The parameters changed were the short-circuit current I_{SC}, open-circuit voltage V_{OC}, maximum power current I_{mpp} and maximum power voltage V_{mpp}. The temperature coefficient of $I_{SC}f$ is also changed according to the 270 W Trina Solar's data sheet. The inverter chosen for the simulation is the same inverter as used at Skaftå, the 6.0 kWp from Fronius International with an operating voltage range between 80 to 800 V. 2 strings each with 12 modules in series is chosen as designed for the FPV system at Skatfå. Figure 5.27 presents the system configuration for the FPV system simulation in PVsyst.

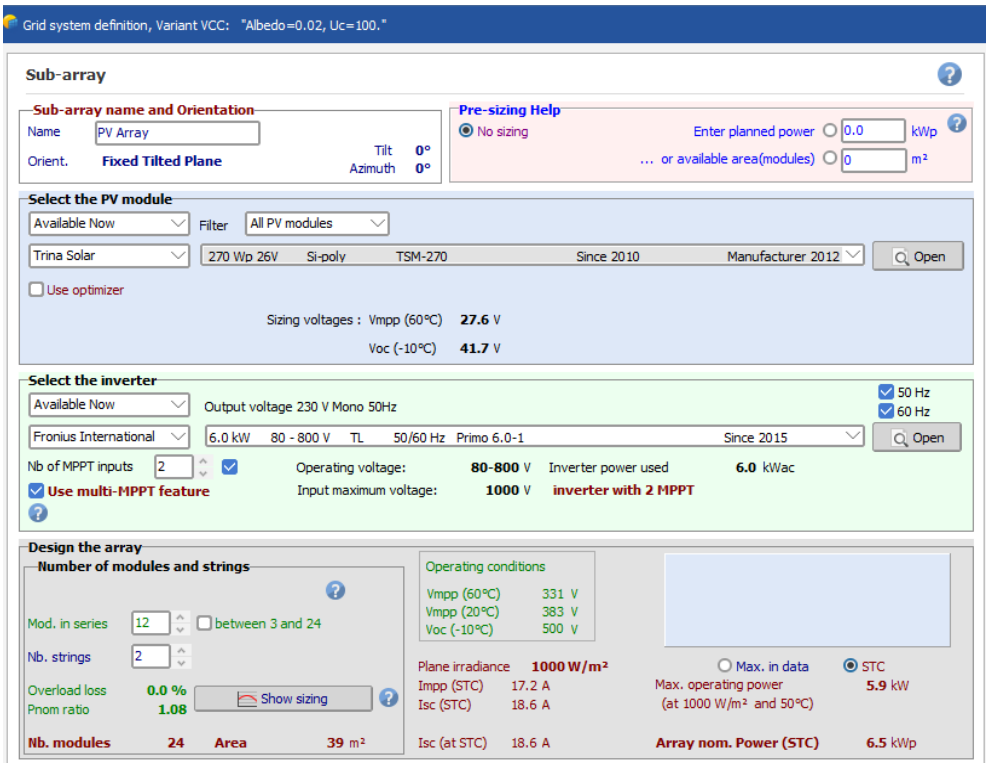

Figure 5.27: System configuration for the FPV system simulation in PVsyst.

Detailed losses: The "global wiring resistance" under the header "Ohmic loses" is set to the default value as proposed by PVsyst, i.e. DC ohmic losses by the array at STC as the 1.5 %. Under "Module quality - LID - Mismatch" header, all parameters were set to default well as shown in Figure 5.28.

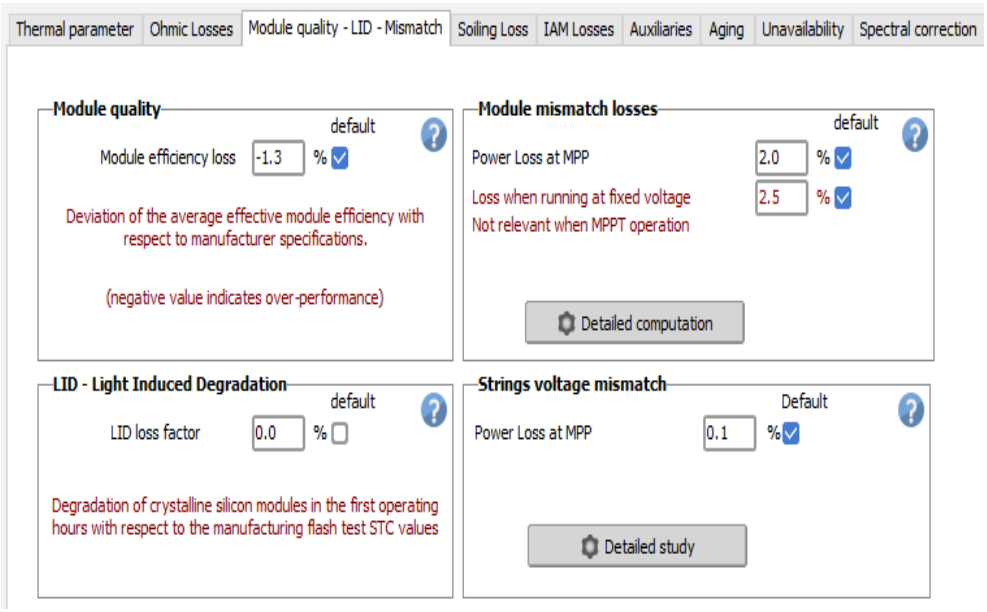

Figure 5.28: System losses for the FPV system simulation in PVsyst.

Under the "Thermal parameter" header, the thermal loss factor is changed for the simulations, to represent actual thermal losses for the FPV system. The thermal losses are varied between 10 $W/m^2.K$ to 100 $W/m^2.K$ with increments of 10 $W/m^2.K$. The constant thermal loss factor, U, initially had its default maximum value set to 50 $W/m^2.K$. This was changed in the "Settings" tab, under the "Edit advanced parameters" header, and setting the "heat loss factor maximal value" to a higher value of 100 $W/m^2.K$.

Albedo: Under "Project settings", the albedo value is changed between the default albedo value of 0.2 and the modelled albedo value of 0.02, as previously determined by the water surface albedo model in Chapter 3. PVsyst only allows the input of monthly average albedo values. The albedo value is varied between 0.2 and 0.02 to evaluate how the annual energy yield for an FPV system varies in the PVsyst simulation.

Shading: No shading diagram is included in the simulation. The surrounding mountains could have been included, but as the FPV analysis only considers the time interval for the unshaded operational time period as previously specified in Chapter 4, Subsection 4.2.1.1 that was argued to be insignificant.

Simulation and analysis: For each of the simulated variant for the ranging U-values, the simulation creates an output file with the project summary and results. From the analysis, only the produced annual energy in $kWh/year$ is of interest to evaluate the effect of the varying thermal loss factor on the annual energy yield.

5.6.1.1 Albedo Effect on Energy Yield

The FPV system in PVsyst is simulated with the detailed system design parameters and with the PV modules mounted at an azimuth of 0° and at fixed tilt angles varying from 0° to 60° as previously discussed in section 5.6.1. Initially, the system is simulated using the default albedo of 0.2 and the modelled albedo value of 0.02 as modelled in this research work, keeping the U-value constant at 20 $W/m^2.K$ for both simulations.

The percentage energy yield difference, E_{diff}, is calculated as follows:

$$E_{diff} = \frac{E_{def} - E_{mod}}{E_{def}} \times 100. \tag{5.6.1}$$

Whereby, E_{def} and E_{mod} is the annual energy yield simulated using the default albedo value of 0.2 and the modelled albedo value of 0.02, respectively.

Figure 5.29 shows the annual energy yield with the varying tilt angles for the default albedo of 0.2 and the modelled albedo value of 0.02. The energy yield is higher when simulated using the default albedo value of 0.2 in comparison to the usage of the modelled albedo value of 0.02. The fixed tilt angle at 40° produces the greatest energy for both the simulations when using the default albedo of 0.2 and the modelled albedo value of 0.02.

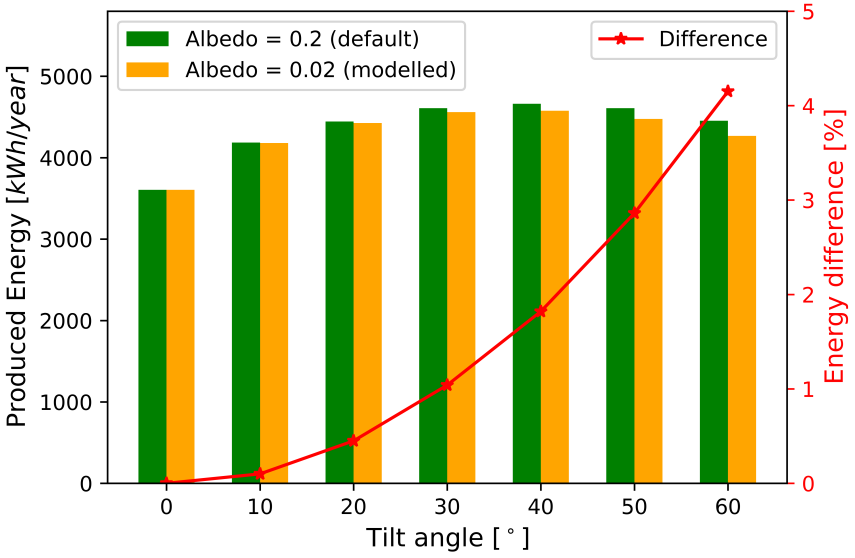

Figure 5.29: Energy yield and difference with the varying tilt angles.

The energy difference at the tilt angle of 0°, i.e. horizontally mounted PV modules, is 0 % as horizontally mounted PV modules cannot make use of the

reflected radiation component. For the tilt angle variation from 0° to 60°, the energy difference using the default albedo value of 0.2 is 0 % to 4.15 % higher in comparison to the modelled albedo value of 0.02. Whereby, the energy difference increases with an increase in the tilt angle.

The optimal tilt angle, $\sum_{optimal}$, of PV modules at solar noon is calculated as [48]:

$$\sum_{optimal} = 90 - \beta_N. \tag{5.6.2}$$

Whereby, β_N is the altitude angle of the Sun at solar noon. β_N is calculated as [48]:

$$\beta_N = 90 - L + \delta. \tag{5.6.3}$$

Whereby, L is the latitude of the relevant location and δ is the solar declination angle. The solar declination angle is calculated as previously discussed in Chapter 2, Section 2.7.

Figure 5.30 shows the heat map of the FPV site in Skafta, with respect to the monthly average optimal tilt angles. It is evident that the optimal tilt angles are higher for months with lower irradiance. The increasing energy difference with an increase in the tilt angle as previously shown in Figure 5.29 is due to the lower irradiance experienced at higher tilt angles as evident in Figure 5.30.

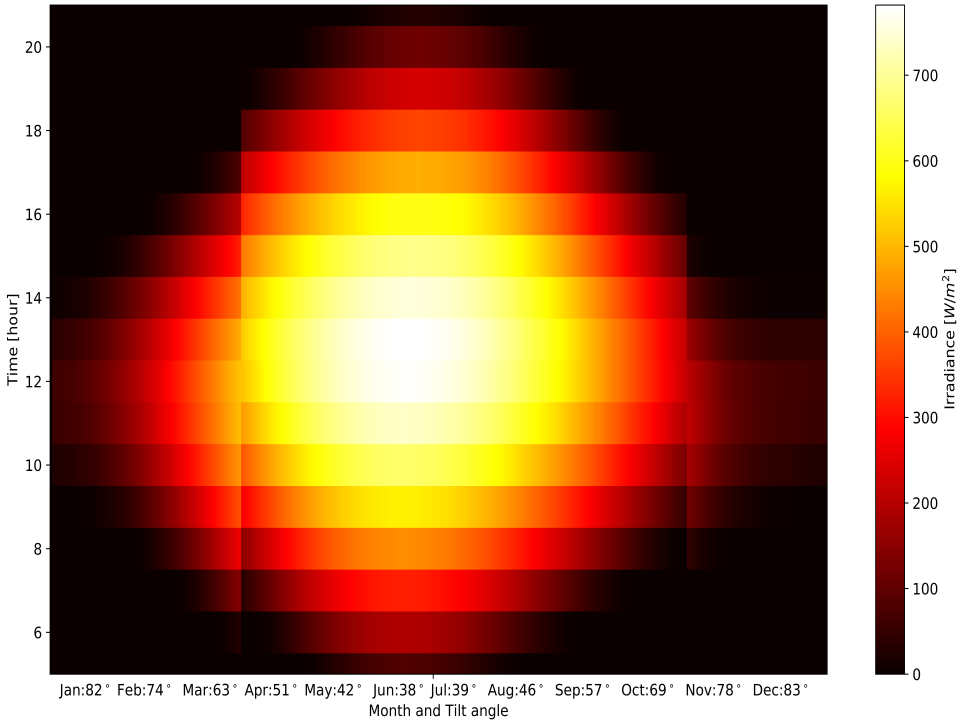

Figure 5.30: Heat map of Skaftå, with respect to the monthly average optimal tilt angles.

5.6.1.2 U-value Effect on Energy Yield

The FPV system in PVsyst is simulated with the detailed system design parameters and with the PV modules mounted at a 0° tilt and 0° azimuth as previously discussed in section 5.6.1. Multiple variants are simulated for the U-values ranging from 10 $W/m^2.K$ to 100 $W/m^2.K$ with increments of 10 $W/m^2.K$. Figure 5.31 shows the change in annual energy yield as the U-values are varied. Energy production increases with an increase in U-value. As a higher U-value shows that the heat transfer from the PV modules to the atmospheric environment is better, therefore the energy yield increases.

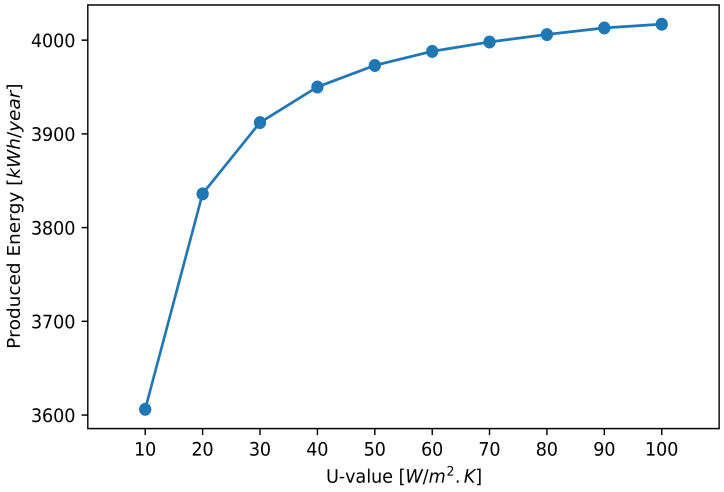

Figure 5.31: Change in energy yield with varying U-values.

The energy difference is calculated using the energy yield of the lowest U-value, 10 $W/m^2.K$. The percentage energy yield difference, E_{U_diff}, is calculated as follows:

$$E_{U_diff} = \frac{E_{tilt} - E_{base}}{E_{base}} \times 100. \tag{5.6.4}$$

Whereby, E_{tilt} is the annual energy yield simulated for the U-values ranging from 10 $W/m^2.K$ to 100 $W/m^2.K$. E_{base} is the annual energy yield simulated for the lowest U-value, 10 $W/m^2.K$. Figure 5.32 shows the difference in the annual energy yield as the U-values are varied. The energy difference increases with an increase in U-value. For U-values bigger than 50 $W/m^2.K$, the difference in energy yield is between 10 % and 12 %.

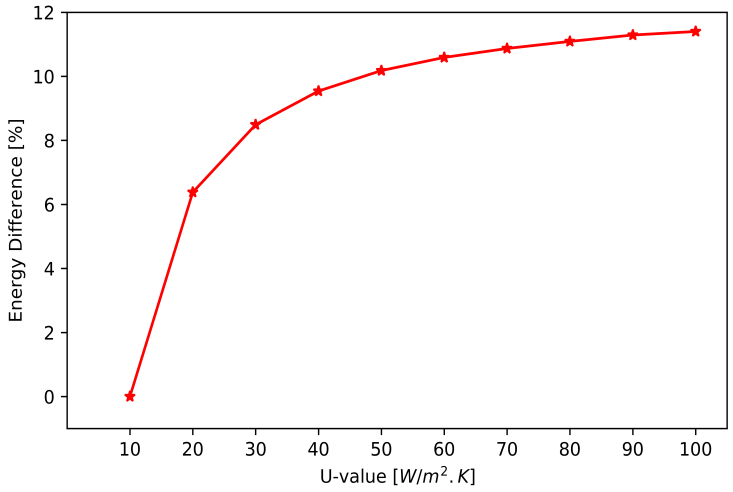

Figure 5.32: Difference in energy yield with varying U-values.

5.7 Summary

In this chapter, a detailed analysis of the U-values for the two different PV systems, FPV and ground-mounted PV system, is conducted. The back-surface module temperature data logging and retrieval from the floating PV site were explained. The application of the clear-sky filter and the data cleaning process was demonstrated. The measured module temperature was analysed and the cell temperature estimation was presented. And finally, the U-value approximations are analysed.

The cell temperature of the water-cooled string was estimated using the change in temperature difference, $\triangle T$ as 0 $^{\circ}C$ with insulated back. Therefore, the cell temperature is equivalent to the back-surface module temperature of the water-cooled string. And the cell temperature of the air-cooled string was estimated using $\triangle T$ as 1 $^{\circ}C$, which is the same as a close roof mounting type for a glass/cell/glass module type. The U-value of the water-cooled string was presented higher than the air-cooled string, as expected. An average U-value for the air-cooled string was found to be 30.14 $W/m^2.K$. This is close to the PVsyst standard value of 29 $W/m^2.K$ for a free-standing system which has an air circulation all around the collectors. The average U-value of 89.44 $W/m^2.K$ of the water-cooled string using water temperature as the base in approximating the U-value corresponds to a better cooling effect due to the direct thermal contact of the PV modules with the floating canvas on the water surface. Therefore, water is a better absorber than air with efficient heat transportation. The higher U-values are effective in maintaining lower PV module temperatures which effectively contributes to better electrical perfor-

mance and vice versa.

For the air-cooled string, abrupt changes in the U-value were also evident for some clear-sky days due to the temperature difference between the cell and the ambient temperature. As for the water-cooled string, abrupt changes in the U-value were evident for some clear-sky days due to the temperature difference between the cell and the water temperature. The water-cooled string's temperature is influenced more by the water temperature than the air temperature. Therefore, the water temperature would have to be accounted for when doing yield forecasting.

The cell temperature of the ground-mounted PV system was estimated using the change in temperature difference, $\triangle T$, between the cell and the back-surface module temperature of modules as 3 $^{\circ}C$. The average U-value was found to be 27.70 $W/m^2.K$ for the weather stations at the ground-mounted PV system. The average U-values of the weather stations is close to the PVsyst standard value of 29 $W/m^2.K$ for a free-standing system which has an air circulation all around the collectors [46]. Comparing the investigated U-values of the air-cooled and the water-cooled FPV strings to the ground-mounted PV system, the average U-value of the air-cooled and water-cooled FPV strings is found to be 8.10 % and 69.03 % higher, respectively, than the average U-value of the ground-mounted PV system.

PVsyst simulation is also conducted to understand the influence of the tilted panels at various tilt angles on the energy yield of the FPV system using the default albedo value of 0.2 vs. the modelled albedo value of 0.02. For the tilt angle variation from 0° to 60°, the energy difference using the default albedo value of 0.2 is 0 % to 4.15 % higher in comparison to the modelled albedo value of 0.02. Whereby, the energy difference increases with an increase in the tilt angles. The increasing energy difference with an increase in the tilt angle is due to the lower irradiance experienced at higher tilt angles.

To investigate the effect of the heat loss coefficient, U-value, on the annual energy yield, PVsyst simulation software is used. The thermal losses were varied between 10 $W/m^2.K$ to 100 $W/m^2.K$ with increments of 10 $W/m^2.K$. It is found that the energy production increases with an increase in U-value. The higher U-value shows that the heat transfer from the PV modules to the atmospheric environment is better, therefore the energy yield increases. The energy difference increases with an increase in U-value. For U-values bigger than 50 $W/m^2.K$, the difference in energy yield is between 10 % and 12 %.

Chapter 6

Conclusions and Recommendation

6.1 Introduction

This project investigated the cooling effect and the albedo effect on the yield of floating PV systems. The research objectives reported in this thesis are as follows:

- To develop a water surface albedo model for FPV systems.
- To investigate the impact of the water surface albedo on the annual energy yield of a floating PV system.
- To conduct a performance analysis of an air-cooled and a water-cooled floating PV string.
- Analyse and compare the difference in the production and the module temperature of an air-cooled vs. a water-cooled floating PV string.
- To investigate a thermal model to estimate the cooling effect of an air-cooled vs. a water-cooled floating PV string in comparison to a ground-mounted PV string.
- Evaluate and compare the heat loss coefficient for floating PV system vs. ground-mounted PV system.
- To evaluate the ability of a PV simulation software, PVsyst, to simulate an FPV system.

The research objectives have been successfully achieved in chapters 2-5. The summary of each chapter follows hereafter.

6.2 Chapter 2

Chapter 2 provides a brief introduction to the theoretical background of solar PV and the wave theory of light. The single diode model of a PV device is used to illustrate the effect of the solar irradiation and temperature on the I-V characteristics. It is observed that the variation of solar irradiance and cell temperature affects the short-circuit current and the open-circuit voltage, respectively.

Furthermore, a brief introduction to optics at an air-water interface is discussed together with the albedo effect of water and Fresnel's effect. The mathematical evaluation of the refractive index of air and water is formulated using Edlén's and Lorentz-Lorens equation, respectively. Finally, appropriate models of the direct beam radiation, sky diffuse radiation and reflected radiation is described.

6.3 Chapter 3

Chapter 3 covers the modelling of the water surface albedo. The albedo of a flat water surface is modelled as a function of time, temperature and wavelength. The Ineichen-Perez clear-sky model is used to predict the clear sky DNI component. A combination of Fresnel's and Snell's laws is applied to determine the reflection and refraction of water. The refractive index of air and water are theoretically estimated using the Edlén's and Lorentz-Lorens equation, respectively. It is found that the refractive index of standard air and liquid water is not largely dependent on the temperature differences but rather the wavelength of the radiation.

Furthermore, the results of the time-varying component of the water surface albedo illustrate that albedo is influenced by the spectral and angular dependencies of the irradiance. It is found that the albedo of a smooth water surface is not constant. The reflective properties show that at higher solar elevations, the albedo is observed to be very low. During early morning and late afternoon, when the solar elevation angle of the sun is lower and the radiation intensity is lower, higher albedo is observed. The water surface albedo model shows that lower albedo is observed than the default value of 0.2. Also, it is found that estimating the reflected radiation using the default albedo value of 0.2 overpredicts the annual energy by 1.15 % in comparison to using the varying water surface albedo.

6.4 Chapter 4

Chapter 4 covers the detailed analysis of two different PV systems, FPV and ground-mounted PV system. Performance analysis of the air-cooled and the

water-cooled floating PV strings shows that the water-cooled string performs between 3.17 % to 7.32 % better than the air-cooled string, for irradiance greater than 200 W/m^2. The average temperature corrected PR for the water-cooled and the air-cooled string was found to be 0.97 and 0.92, respectively, for irradiance greater than 200 W/m^2. The average performance values of the FPV strings were found to be very high, especially in the Nordic context. The higher PR values are due to the fact that the FPV system is a relatively small system, with shorter cables. Thus, indicative to presume that the net system losses are small and the cooling effect is favourable considering the climatic conditions in Norway.

The PR of both the FPV strings were also not the same, as there is a discrepancy present in some measurements. Therefore, it is recommended that further research should be conducted to correct the PR for temperature and also to ensure the calibration of measuring equipment. Furthermore, ground-mounted weather station's data analysis illustrates a slight difference in measured irradiance at each weather stations due to inactive or improper functioning of the data logger or instrumentation. The measured air temperature at the ground-mounted PV system showed more fluctuations as the irradiance levels increased. As the irradiance levels increased the air and module temperatures also increased.

6.5 Chapter 5

Chapter 5 provides a detailed analysis of the U-values for the two different PV systems, FPV and ground-mounted PV system. The U-value of the water-cooled string was presented higher than the air-cooled string. An average U-value for the air-cooled string was found to be 30 $W/m^2.K$. The average U-value of 89 $W/m^2.K$ of the water-cooled string using water temperature as the base in approximating how the U-value corresponds to a better cooling effect due to the direct thermal contact of the PV modules with the floating canvas on the water surface. Abrupt changes in the U-values for the air-cooled string is also observed for some clear-sky days due to the temperature difference between the cell and the ambient temperature. As for the water-cooled string, abrupt changes in the U-value were evident for some clear-sky days due to the temperature difference between the cell and the water temperature. The water-cooled string's temperature is influenced more by the water temperature than the air temperature. Therefore, the water temperature would have to be accounted for when doing yield forecasting.

The average U-value was found to be 27 $W/m^2.K$ for the ground-mounted PV system. Comparing the investigated U-values of the air-cooled and the water-cooled FPV strings to the ground-mounted PV system, the average U-value of

the air-cooled and water-cooled FPV strings is found to be 8.10 % and 69.03 % higher, respectively, than the average U-value of the ground-mounted PV system. Furthermore, PVsyst simulation is also conducted to understand the influence of the tilted panels at various tilt angles on the energy yield of the FPV system using the default albedo value of 0.2 vs. the modelled albedo value of 0.02. It is observed that the energy difference increases with an increase in the tilt angles and U-value.

6.6 Research Conclusions

In this research work, the cooling effect and the albedo effect on the yield of a floating PV system are successfully investigated. A water surface albedo model for FPV solar plants is successfully developed which illustrates very low albedo for water. A study on the performance of the Ocean Sun's floating PV technology shows lower module temperatures and thus, indicating a better cooling effect. Furthermore, a thermal model is successfully investigated to estimate the cooling effect of an air-cooled and a water-cooled floating PV string in comparison to a ground-mounted PV string. Higher U-values are found for the water-cooled FPV string in comparison to the air-cooled FPV string and the ground-mounted PV system. Therefore, indicative that Ocean Sun's FPV technology is favourable to better cooling effect due to the thermal contact of the PV modules on the water surface. Also, PVsyst simulation is conducted which demonstrates that the energy difference increases with an increase in the tilt angle and U-value. All the objectives as presented in this thesis was successfully achieved and completed.

6.7 Recommendations and Future Work

To improve on the current research work as documented in this thesis, the following recommendations could be implemented for future work:

- To determine the extent to which the water surface albedo model operates, as developed in this research, measured reflected radiation data from an FPV system is necessary which will allow for comparison of the measured albedo vs. the modelled albedo.
- To obtain more concrete results of the thermal coefficient, a longer period of data analysis is crucial. Especially, to analyse the FPV system under higher irradiance and temperatures, for both air and water.
- To obtain more accurate measured data, it is advised that the measuring equipment is calibrated.

- Compare the actual yield of an FPV system against a ground-mounted system and investigate the differences at various locations and different times of the year.
- As floating PV installations are globally increasing, the demand for modelling FPV systems is likely to increase. According to the author's knowledge, there are no FPV simulation software available and current PV simulation software has not integrated features for modelling FPV technology. Therefore, it is recommended that the simulation software are developed to upgrade features, such as making water surfaces available as sites for FPV installations.

List of References

[1] Iea: Global energy & co2 status report 2019 analysis. March 2019. [Accessed: 22-December-2020]. [Online].
Available at: https://www.iea.org/reports/global-energy-co2-status-report-2019

[2] Huber, M.T.: Energizing historical materialism: Fossil fuels, space and the capitalist mode of production. *Geoforum*, vol. 40, no. 1, pp. 105–115, Elsevier, 2009.

[3] Das, U.K., Tey, K.S., Seyedmahmoudian, M., Mekhilef, S., Idris, M.Y.I., Van Deventer, W., Horan, B. and Stojcevski, A.: Forecasting of photovoltaic power generation and model optimization: A review. *Renewable and Sustainable Energy Reviews*, vol. 81, pp. 912–928, Elsevier, 2018.

[4] Steckel, J.C., Edenhofer, O. and Jakob, M.: Drivers for the renaissance of coal. *Proceedings of the National Academy of Sciences*, vol. 112, no. 29, pp. E3775–E3781, National Acad Sciences, 2015.

[5] What is the paris agreement? [Accessed: 22-December-2020]. [Online].
Available at: https://unfccc.int/process-and-meetings/the-paris-agreement/what-is-the-paris-agreement

[6] Hertwich, E.G. and Peters, G.P.: Carbon footprint of nations: A global, trade-linked analysis. *Environmental science & technology*, vol. 43, no. 16, pp. 6414–6420, ACS Publications, 2009.

[7] Wang, W., Lin, J.-Y., Cui, S.-H. and Lin, T.: An overview of carbon footprint analysis. *Huanjing Kexue yu Jishu*, vol. 33, no. 7, pp. 71–78, Hubei-sheng Huanjing Baohu Ju, Wuchang Luojianshan 81 Lu 338 Hao Wuhan, 2010.

[8] Renewable energy statistics 2020. July 2020. [Accessed: 22-December-2020]. [Online].
Available at: https://www.irena.org/publications/2020/Jul/Renewable-energy-statistics-2020

[9] Kannan, N. and Vakeesan, D.: Solar energy for future world:-a review. *Renewable and Sustainable Energy Reviews*, vol. 62, pp. 1092–1105, Elsevier, 2016.

[10] Fahrenbruch, A. and Bube, R.: *Fundamentals of solar cells: photovoltaic solar energy conversion*. Academic Press, 1983.

[11] Kim, S.-M., Oh, M. and Park, H.-D.: Analysis and prioritization of the floating photovoltaic system potential for reservoirs in korea. *Applied Sciences*, vol. 9, no. 3, p. 395, Multidisciplinary Digital Publishing Institute, 2019.

[12] When it comes to water, you have to think global climate change: Vital signs of the planet. Apr 2020. [Accessed: 22-December-2020]. [Online]. Available at: `https://climate.nasa.gov/news/2977/when-it-comes-to-water-you-have-to-think-global/`

[13] Liu, H., Krishna, V., Lun Leung, J., Reindl, T. and Zhao, L.: Field experience and performance analysis of floating pv technologies in the tropics. *Progress in Photovoltaics: Research and Applications*, vol. 26, no. 12, pp. 957–967, Wiley Online Library, 2018.

[14] Patil, S., Wagh, M. and Shinde, N.: A review on floating solar photovoltaic power plants. *Int. J. Sci. Eng. Res*, vol. 8, pp. 789–794, 2017.

[15] Group, W.B., ESMAP and SERIS: Where sun meets water : Floating solar handbook for practitioners. Oct 2019. [Accessed: 21-December-2020]. [Online]. Available at: `http://documents.worldbank.org/curated/en/418961572293438109/Where-Sun-Meets-Water-Floating-Solar-Handbook-for-Practitioner`

[16] Ko, J.W., Cha, H.L., Kim, D.K.-S., Lim, J.R., Kim, G.G., Bhang, B.G., Won, C.S., Jung, H.S., Kang, D.H. and Ahn, H.K.: Safety analysis of grounding resistance with depth of water for floating pvs. *Energies*, vol. 10, no. 9, p. 1304, Multidisciplinary Digital Publishing Institute, 2017.

[17] Group, W.B., ESMAP and SERIS: Where sun meets water : Floating solar market report. Jun 2019. [Accessed: 22-December-2020]. [Online]. Available at: `https://openknowledge.worldbank.org/handle/10986/31880`

[18] Trapani, K. and Redón Santafé, M.: A review of floating photovoltaic installations: 2007–2013. *Progress in Photovoltaics: Research and Applications*, vol. 23, no. 4, pp. 524–532, Wiley Online Library, 2015.

[19] Solarplaza: 200 global floating solar plants. Jun 2019. [Accessed: 27-August-2019]. [Online]. Available at: `https://www.floatingsolarconference.com/news-source/2019/6/5/120-global-floating-solar-plants`

[20] Solarplaza: Top 200 - operational floating solar projects. Jun 2020. [Accessed: 22-December-2020]. [Online]. Available at: `https://www.floatingsolarconference.com/news-source/2020/6/30/top-200-operational-floating-solar-projects`

[21] Patel, S.S. and Rix, A.J.: Water surface albedo modelling for floating pv plants. *Europe*, vol. 19, pp. 915–31, 2019.

[22] African renewable energy company installs first commercial floating solar farm in africa at marlenique farm. Jul 2019. [Accessed: 21-December-2020]. [Online].
Available at: `https://www.ciel-et-terre.net/african-renewable-energy-company-installs-first-commercial-floating-solar-farm-in`

[23] Group, W.B., ESMAP and SERIS: Where sun meets water (vol. 2) : Floating solar market report (english). Jun 2019. [Accessed: 22-December-2020]. [Online].
Available at: `https://documents.worldbank.org/en/publication/documents-reports/documentdetail/670101560451219695/floating-solar-market-report`

[24] Guerrero-Lemus, R., Vega, R., Kim, T., Kimm, A. and Shephard, L.: Bifacial solar photovoltaics–a technology review. *Renewable and sustainable energy reviews*, vol. 60, pp. 1533–1549, Elsevier, 2016.

[25] Yusufoglu, U.A., Pletzer, T.M., Koduvelikulathu, L.J., Comparotto, C., Kopecek, R. and Kurz, H.: Analysis of the annual performance of bifacial modules and optimization methods. *IEEE Journal of Photovoltaics*, vol. 5, no. 1, pp. 320–328, IEEE, 2014.

[26] Keating, C.: Enerwhere anchors offshore bifacial pv project on uae seawater. Feb 2020. [Accessed: 22-December-2020]. [Online].
Available at: `https://www.pv-tech.org/news/everwhere-reveals-offshore-pv-project-on-persian-gulf`

[27] Sunprojects gaat te water. [Accessed: 22-December-2020]. [Online].
Available at: `https://sun-projects.nl/project/oostvoornse-meer`

[28] Solarisfloat installs its first protevs project in the netherlands. [Accessed: 22-December-2020]. [Online].
Available at: `https://www.solarisfloat.com/solarisfloat-installs-first-protevs-in-netherlands/`

[29] Cazzaniga, R., Rosa-Clot, M., Rosa-Clot, P. and Tina, G.M.: Integration of pv floating with hydroelectric power plants. *Heliyon*, vol. 5, no. 6, p. e01918, Elsevier, 2019.

[30] Patterson, B.D., Mo, F., Borgschulte, A., Hillestad, M., Joos, F., Kristiansen, T., Sunde, S. and Van Bokhoven, J.A.: Renewable co2 recycling and synthetic fuel production in a marine environment. *Proceedings of the National Academy of Sciences*, vol. 116, no. 25, pp. 12212–12219, National Acad Sciences, 2019.

[31] Sahu, A., Yadav, N. and Sudhakar, K.: Floating photovoltaic power plant: A review. *Renewable and sustainable energy reviews*, vol. 66, pp. 815–824, Elsevier, 2016.

[32] Galdino, M.A.E. and de Almeida Olivieri, M.M.: Some remarks about the deployment of floating pv systems in brazil. *J. Electr. Eng*, vol. 1, pp. 10–19, 2017.

[33] Choi, Y.-K.: A study on power generation analysis of floating pv system considering environmental impact. *International journal of software engineering and its applications*, vol. 8, no. 1, pp. 75–84, Science and Engineering Research Support Society, 2014.

[34] Choi, Y.K., Choi, W.S. and Lee, J.H.: Empirical research on the efficiency of floating pv systems. *Science of Advanced Materials*, vol. 8, no. 3, pp. 681–685, American Scientific Publishers, 2016.

[35] Yadav, N., Gupta, M. and Sudhakar, K.: Energy assessment of floating photovoltaic system. In: *2016 International Conference on Electrical Power and Energy Systems (ICEPES)*, pp. 264–269. IEEE, 2016.

[36] Liu, L., Wang, Q., Lin, H., Li, H., Sun, Q. *et al.*: Power generation efficiency and prospects of floating photovoltaic systems. *Energy Procedia*, vol. 105, pp. 1136–1142, Elsevier, 2017.

[37] Azmi, M.S.M., Othman, M.Y.H., Ruslan, M.H.H., Sopian, K. and Majid, Z.A.A.: Study on electrical power output of floating photovoltaic and conventional photovoltaic. In: *AIP Conference Proceedings*, vol. 1571, pp. 95–101. American Institute of Physics, 2013.

[38] Trapani, K. and Millar, D.L.: The thin film flexible floating pv (t3f-pv) array: The concept and development of the prototype. *Renewable energy*, vol. 71, pp. 43–50, Elsevier, 2014.

[39] Majid, Z., Ruslan, M., Sopian, K., Othman, M. and Azmi, M.: Study on performance of 80 watt floating photovoltaic panel. *Journal of Mechanical Engineering and Sciences*, vol. 7, no. 1, pp. 1150–1156, 2014.

[40] Bellini, E.: Japan's largest floating pv plant catches fire after typhoon faxai impact. Sep 2019. [Accessed: 22-December-2020]. [Online]. Available at: `https://www.pv-magazine.com/2019/09/09/japans-largest-floating-pv-plant-catches-fire-after-typhoon-faxai-impact/`

[41] Durković, V. and Đurišić, Ž.: Analysis of the potential for use of floating pv power plant on the skadar lake for electricity supply of aluminium plant in montenegro. *Energies*, vol. 10, no. 10, p. 1505, Multidisciplinary Digital Publishing Institute, 2017.

[42] Gotmare, J.A. and Prayagi, S.: Enhancing the performance of photovoltaic panels by stationary cooling. *International Journal of Science, Engineering and Technology*, vol. 2, no. 7, pp. 1465–1468, 2014.

[43] Applications to solar, on water. [Accessed: 22-December-2020]. [Online]. Available at: `https://www.ciel-et-terre.net/floating-pv-applications/`

[44] Floating. [Accessed: 22-December-2020]. [Online].
Available at: `https://www.sungrowpower.com/en/division/floating`

[45] A unique solution to floating solar. . [Accessed: 22-December-2020]. [Online].
Available at: `https://oceansun.no/`

[46] Array thermal losses. [Accessed: 21-December-2020]. [Online].
Available at: `https://www.pvsyst.com/help/thermal_loss.htm`

[47] Duffie, J.A. and Beckman, W.A.: *Solar engineering of thermal processes*. 3rd edn. Wiley, 2006.

[48] Masters, G.M.: *Renewable and efficient electric power systems*. John Wiley & Sons, 2013.

[49] Duffie, J.A. and Beckman, W.A.: *Solar engineering of thermal processes*. 4th edn. Wiley, 2013.

[50] Smets, A.H., Jäger, K., Isabella, O., Swaaij, R.A. and Zeman, M.: Solar energy: The physics and engineering of photovoltaic conversion, technologies and systems. UIT Cambridge, 2015.

[51] Boyd, M. and Hansen, C.: single diode equivalent circuit models. [Accessed: 22-December-2020]. [Online].
Available at: `https://pvpmc.sandia.gov/modeling-steps/2-dc-module-iv/diode-equivalent-circuit-models/`

[52] De Soto, W., Klein, S.A. and Beckman, W.A.: Improvement and validation of a model for photovoltaic array performance. *Solar energy*, vol. 80, no. 1, pp. 78–88, Elsevier, 2006.

[53] Luque, A. and Hegedus, S.: *Handbook of photovoltaic science and engineering*. John Wiley & Sons, 2011.

[54] Rodrigues, E.M., Melicio, R., Mendes, V. and Catalao, J.P.: Simulation of a solar cell considering single-diode equivalent circuit model. In: *International conference on renewable energies and power quality, Spain*, pp. 13–15. 2011.

[55] Walker, G. *et al.*: Evaluating mppt converter topologies using a matlab pv model. *Journal of Electrical & Electronics Engineering*, vol. 21, no. 1, pp. 49–56, 2001.

[56] Tian, H., Mancilla-David, F., Ellis, K., Muljadi, E. and Jenkins, P.: A cell-to-module-to-array detailed model for photovoltaic panels. *Solar energy*, vol. 86, no. 9, pp. 2695–2706, Elsevier, 2012.

[57] Walker, G.R.: Evaluating mppt converter topologies using a matlab pv model. *AUPEC 2000: Innovation for Secure Power*, vol. 1, pp. 138–143, Queensland University of Technology, 2000.

[58] Iv curve. . [Accessed: 22-December-2020]. [Online]. Available at: `https://www.pveducation.org/pvcdrom/solar-cell-operation/iv-curve`

[59] Open-circuit voltage. . [Accessed: 22-December-2020]. [Online]. Available at: `https://www.pveducation.org/pvcdrom/solar-cell-operation/open-circuit-voltage`

[60] Pv temperature coefficient of power. [Accessed: 22-December-2020]. [Online]. Available at: `https://www.homerenergy.com/products/pro/docs/latest/pv_temperature_coefficient_of_power.html`

[61] Buchwald, J.Z. *et al.*: *The rise of the wave theory of light: Optical theory and experiment in the early nineteenth century*. University of Chicago Press, 1989.

[62] Fresnel, A.: *Oeuvres complètes d'augustin Fresnel*. Imprimerie impériale, 1868.

[63] Bryant, F.: Snell's law of refraction. *Physics Bulletin*, vol. 9, no. 12, p. 317, IOP Publishing, 1958.

[64] Halpern, A. and Erlbach, E.: *Schaum's Outline of Beginning Physics II: Electricity and Magnetism, Optics, Modern Physics*, vol. 2. McGraw Hill Professional, 1998.

[65] Zwinkels, J.C.: Light, electromagnetic spectrum. Jan 2015. Available at: `https://www.researchgate.net/publication/304195368_Light_Electromagnetic_Spectrum`

[66] Goh, M.W.C.: Basic electromagnetic theory. In: *Analyzing the Physics of Radio Telescopes and Radio Astronomy*, pp. 68–77. IGI Global, 2020.

[67] Marion, J.B.: *Physics in the Modern World*. 2nd edn. Academic Press, 1981. [Accessed: 22-December-2020]. [Online]. Available at: `http://www.sciencedirect.com/science/article/pii/B9780124722804500162`

[68] Wang, G.Z.J., Xu, W., Zhang, K. and Ma, Z.: Polarization patterns of transmitted celestial light under wavy water surfaces. *Water Optics and Water Colour Remote Sensing*, p. 23, MDPI, 2018.

[69] Shashar, N., Sabbah, S. and Cronin, T.W.: Transmission of linearly polarized light in seawater: implications for polarization signaling. *Journal of Experimental Biology*, vol. 207, no. 20, pp. 3619–3628, The Company of Biologists Ltd, 2004.

[70] Azzam, R. and Adams, R.M.: Transmission of p-and s-polarized light through a prism and the condition of minimum deviation. *JOSA A*, vol. 27, no. 9, pp. 2085–2090, Optical Society of America, 2010.

[71] Shevchenko, A., Roussey, M., Friberg, A.T. and Setälä, T.: Polarization time of unpolarized light. *Optica*, vol. 4, no. 1, pp. 64–70, Optical Society of America, 2017.

[72] Ineichen, P., Guisan, O. and Perez, R.: Ground-reflected radiation and albedo. *Solar Energy*, vol. 44, no. 4, pp. 207–214, Elsevier, 1990.

[73] Coakley, J.: Reflectance and albedo, surface. *Encyclopedia of the Atmosphere*, pp. 1914–1923, Academic, 2003.

[74] Gul, M., Kotak, Y., Muneer, T. and Ivanova, S.: Enhancement of albedo for solar energy gain with particular emphasis on overcast skies. *Energies*, vol. 11, no. 11, p. 2881, Multidisciplinary Digital Publishing Institute, 2018.

[75] Howell, J.R., Menguc, M.P. and Siegel, R.: *Thermal radiation heat transfer*. CRC press, 2010.

[76] Lhermitte, S., Abermann, J. and Kinnard, C.: Albedo over rough snow and ice surfaces. *Cryosphere*, vol. 8, no. 3, pp. 1069–1086, Copernicus Publications, 2014.

[77] Wendisch, M., Pilewskie, P., Jäkel, E., Schmidt, S., Pommier, J., Howard, S., Jonsson, H.H., Guan, H., Schröder, M. and Mayer, B.: Airborne measurements of areal spectral surface albedo over different sea and land surfaces. *Journal of Geophysical Research: Atmospheres*, vol. 109, no. D8, Wiley Online Library, 2004.

[78] Vokrouhlicky, D. and Farinella, P.: Specular reflection of sunlight from wavy ocean surfaces and the albedo effect on satellite orbits. ii. lageos long-term albedo perturbations reassessed. *Astronomy and Astrophysics*, vol. 301, p. 282, 1995.

[79] Bender, F.A.-M., Engström, A. and Karlsson, J.: Factors controlling cloud albedo in marine subtropical stratocumulus regions in climate models and satellite observations. *Journal of Climate*, vol. 29, no. 10, pp. 3559–3587, 2016.

[80] Robock, A.: The seasonal cycle of snow cover, sea ice and surface albedo. *Monthly Weather Review*, vol. 108, no. 3, pp. 267–285, 1980.

[81] Berbet, M.L. and Costa, M.H.: Climate change after tropical deforestation: seasonal variability of surface albedo and its effects on precipitation change. *Journal of Climate*, vol. 16, no. 12, pp. 2099–2104, 2003.

[82] Albedo coefficient. [Accessed: 21-December-2020]. [Online]. Available at: `https://www.pvsyst.com/help/albedo.htm`

[83] Cogley, J.G.: The albedo of water as a function of latitude. *Monthly Weather Review*, vol. 107, no. 6, pp. 775–781, 1979.

[84] Meyer, R.: Theory of water-wave refraction. *Advances in applied mechanics.*, vol. 19, pp. 53–141, 1979.

[85] Biegański, W. and Kasiński, A.: Image acquisition in an underwater vision system with nir and vis illumination. *arXiv preprint arXiv:1402.1151*, 2014.

[86] Schwaiger, H.P. and Bird, D.N.: Integration of albedo effects caused by land use change into the climate balance: Should we still account in greenhouse gas units? *Forest Ecology and Management*, vol. 260, no. 3, pp. 278–286, Elsevier, 2010.

[87] Cazzaniga, R., Cicu, M., Rosa-Clot, M., Rosa-Clot, P., Tina, G. and Ventura, C.: Floating photovoltaic plants: Performance analysis and design solutions. *Renewable and Sustainable Energy Reviews*, vol. 81, pp. 1730–1741, Elsevier, 2018.

[88] Katsaros, K.B., McMurdie, L.A., Lind, R.J. and DeVault, J.E.: Albedo of a water surface, spectral variation, effects of atmospheric transmittance, sun angle and wind speed. *Journal of Geophysical Research: Oceans*, vol. 90, no. C4, pp. 7313–7321, Wiley Online Library, 1985.

[89] Winton, M.: Amplified arctic climate change: What does surface albedo feedback have to do with it? *Geophysical Research Letters*, vol. 33, no. 3, Wiley Online Library, 2006.

[90] Hall, A. and Qu, X.: Using the current seasonal cycle to constrain snow albedo feedback in future climate change. *Geophysical Research Letters*, vol. 33, no. 3, Wiley Online Library, 2006.

[91] Lavers, C.: *Physics Wave Concepts for Marine Engineering Applications*. Jun 2017.

[92] Pohl, R.W.: Discovery of interference by thomas young. *American Journal of Physics*, vol. 28, no. 6, pp. 530–532, American Association of Physics Teachers, 1960.

[93] Rheims, J., Köser, J. and Wriedt, T.: Refractive-index measurements in the near-ir using an abbe refractometer. *Measurement Science and Technology*, vol. 8, no. 6, p. 601, IOP Publishing, 1997.

[94] LI, D.-g. and ZHANG, G.-x.: Measurement and compensation for refractive index of air using a pre-evacuated airtight sealed cavity. *Optics and Precision Engineering*, vol. 1, 2001.

[95] Hou, W. and Thalmann, R.: Accurate measurement of the refractive index of air. *Measurement*, vol. 13, no. 4, pp. 307–314, Elsevier, 1994.

[96] Bönsch, G. and Potulski, E.: Measurement of the refractive index of air and comparison with modified edlén's formulae. *Metrologia*, vol. 35, no. 2, p. 133, IOP Publishing, 1998.

[97] Ren, G.-Y., Qu, X.-H. and Ding, S.: A real-time measurement method of air refractive index based on special material etalon. *Applied Sciences*, vol. 8, no. 11, p. 2325, Multidisciplinary Digital Publishing Institute, 2018.

[98] Kim, C.-B. and Su, C.B.: Measurement of the refractive index of liquids at 1.3 and 1.5 micron using a fibre optic fresnel ratio meter. *Measurement Science and Technology*, vol. 15, no. 9, p. 1683, IOP Publishing, 2004.

[99] Cataldo, E., Di Lieto, A., Maccarrone, F. and Paffuti, G.: Measuring the refractive index of water with a pulsed laser diode. *European Journal of Physics*, vol. 37, no. 6, p. 062002, IOP Publishing, 2016.

[100] Birch, K. and Downs, M.: An updated edlén equation for the refractive index of air. *Metrologia*, vol. 30, no. 3, p. 155, IOP Publishing, 1993.

[101] Ciddor, P.E. and Hill, R.J.: Refractive index of air. 2. group index. *Applied Optics*, vol. 38, no. 9, pp. 1663–1667, Optical Society of America, 1999.

[102] Schiebener, P., Straub, J., Levelt Sengers, J. and Gallagher, J.: Refractive index of water and steam as function of wavelength, temperature and density. *Journal of physical and chemical reference data*, vol. 19, no. 3, pp. 677–717, American Institute of Physics for the National Institute of Standards and Technology, 1990.

[103] Patel, S.S. and Rix, A.J.: The impact of water surface albedo on incident solar insolation of a collector surface. In: *2020 International SAUPEC/RobMech/PRASA Conference*, pp. 1–6. IEEE, 2020.

[104] Holmgren, W., Hansen, C. and Mikofski, M.: pvlib python: A python package for modeling solar energy systems. *Journal of Open Source Software*, vol. 3, no. 29, p. 884, 2018.

[105] Holmgren, W., Calama-Consulting, Lorenzo, T., Hansen, C., Mikofski, M., Krien, U., bmu, DaCoEx, Driesse, A., konstant_t and et al.: pvlib/pvlib-python: v0.7.1. Jan 2020.

[106] Loshin, D.S.: *The geometrical optics workbook*. Elsevier Health Sciences, 2015.

[107] Islam, M.S., Younis, M. and Ahmed, A.: Communication through air water interface using multiple light sources. In: *2018 IEEE International Conference on Communications (ICC)*, pp. 1–6. IEEE, 2018.

[108] Brooks, M.J., du Clou, S., van Niekerk, W.L., GauchÃ©, P., Leonard, C., Mouzouris, M.J., Meyer, R., van der Westhuizen, N., van Dyk, E.E. and Vorster, F.J.: SAURAN: A new resource for solar radiometric data in Southern Africa. *Journal of Energy in Southern Africa*, vol. 26, pp. 2 – 10, Feb scieloza, 2015. ISSN 1021-447X. [Accessed: 22-December-2020]. [Online]. Available at: `http://www.scielo.org.za/scielo.php?script=sci_arttext&pid=S1021-447X2015000100001&nrm=iso`

[109] Station. [Accessed: 22-December-2020]. [Online]. Available at: `https://sauran.ac.za/`

[110] Stellenbosch weather. [Accessed: 22-December-2020]. [Online]. Available at: `http://weather.sun.ac.za/`

[111] Graham, J.W.: Missing data analysis: Making it work in the real world. *Annual review of psychology*, vol. 60, pp. 549–576, Annual Reviews, 2009.

[112] Kang, H.: The prevention and handling of the missing data. *Korean journal of anesthesiology*, vol. 64, no. 5, p. 402, Korean Society of Anesthesiologists, 2013.

[113] Perez, R., Ineichen, P., Seals, R., Michalsky, J. and Stewart, R.: Modeling daylight availability and irradiance components from direct and global irradiance. *Solar energy*, vol. 44, no. 5, pp. 271–289, 1990.

[114] Ineichen, P.: A broadband simplified version of the solis clear sky model. *Solar Energy*, vol. 82, no. 8, pp. 758–762, Elsevier, 2008.

[115] Surfrad aerosol optical depth. [Accessed: 22-December-2020]. [Online]. Available at: `https://www.esrl.noaa.gov/gmd/grad/surfrad/aod/#:~:text=Aerosol%20optical%20depth%20is%20a,absorbing%20or%20by%20scattering%20light.&text=An%20average%20aerosol%20optical%20depth%20for%20the%20U.S.%20is%200.1%20to%200.15.`

[116] Source code for pvlib.clearsky. . [Accessed: 22-December-2020]. [Online]. Available at: `https://pvlib-python.readthedocs.io/en/latest/_modules/pvlib/clearsky.html#simplified_solis`

[117] Hersey, S., Garland, R., Crosbie, E., Shingler, T., Sorooshian, A., Piketh, S. and Burger, R.: An overview of regional and local characteristics of aerosols in south africa using satellite, ground, and modeling data. *ACPD*, vol. 14, no. 17, pp. 24701–24752, 2014.

[118] Ranjan, R.R., Ganguly, N.D., Joshi, H. and Iyer, K.: Study of aerosol optical depth and precipitable water vapour content at rajkot, a tropical semi-arid station. CSIR, 2007.

[119] Molineaux, B., Ineichen, P. and O' Neill, N.: Equivalence of pyrheliometric and monochromatic aerosol optical depths at a single key wavelength. *Applied optics*, vol. 37, no. 30, pp. 7008–7018, Optical Society of America, 1998.

[120] Linke turbidity factor. Apr 2020. [Accessed: 22-December-2020]. [Online]. Available at: `http://www.soda-pro.com/help/general-knowledge/linke-turbidity-factor`

[121] Ineichen, P. and Perez, R.: A new airmass independent formulation for the linke turbidity coefficient. *Solar Energy*, vol. 73, no. 3, pp. 151–157, Elsevier, 2002.

[122] Hoyer-Klick, C.: Introduction to solar resource assessments. 2010. [Accessed: 22-December-2020]. [Online].
Available at: http://academic.sun.ac.za/crses/UNEP/Introduction%20to%20Resource%20Assessments%20Workshop.pdf

[123] Badescu, V.: Verification of some very simple clear and cloudy sky models to evaluate global solar irradiance. *Solar Energy*, vol. 61, no. 4, pp. 251–264, Elsevier, 1997.

[124] Ineichen, P.: Comparison of eight clear sky broadband models against 16 independent data banks. *Solar Energy*, vol. 80, no. 4, pp. 468–478, Elsevier, 2006.

[125] Ocean sun - model cf 200 - circular solar photovoltaic floater. . [Accessed: 22-December-2020]. [Online].
Available at: https://www.environmental-expert.com/products/ocean-sun-model-cf-200-circular-floater-648129

[126] Google maps. [Accessed: 22-December-2020]. [Online].
Available at: https://www.google.com/maps/@60.4541338,5.6217976,92m/data=!3m1!1e3

[127] Floating solar technical design. [Accessed: 22-December-2020]. [Online].
Available at: https://www.multiconsultgroup.com/projects/floating-solar-technical-design/

[128] Duomax module. [Accessed: 08-January-2021]. [Online].
Available at: http://static.trinasolar.com/sites/default/files/EN_TSM_PEG5_datasheet_B_2017_web.pdf

[129] Fronius primo. . [Accessed: 22-December-2020]. [Online].
Available at: https://www.fronius.com/en/solar-energy/installers-partners/technical-data/all-products/inverters/fronius-primo/fronius-primo-6-0-1

[130] Fronius sensor card / box. . [Accessed: 22-December-2020]. [Online].
Available at: https://www.fronius.com/en/solar-energy/installers-partners/technical-data/all-products/system-monitoring/hardware/fronius-sensor-card-box/fronius-sensor-box

[131] Sensor. [Accessed: 22-December-2020]. [Online].
Available at: https://www.fronius.com/en/solar-energy/installers-partners/technical-data/all-products/system-monitoring/hardware/sensors/ambient-temperature-sensor

[132] Sensors. [Accessed: 22-December-2020]. [Online].
Available at: https://www.fronius.com/th-th/thailand/photovoltaics/products/commercial/system-monitoring/hardware/sensors/irradiation-sensor

[133] Sensors. [Accessed: 22-December-2020]. [Online].
Available at: https://www.fronius.com/en/solar-energy/installers-partners/technical-data/all-products/system-monitoring/hardware/sensors/wind-sensor

[134] Thermosense datasheet. [Accessed: 22-December-2020]. [Online].
Available at: https://www.thermosense.co.uk/pdfs/datasheets/thermosense_datasheet_041.pdf

[135] Rtdtempx series. [Accessed: 22-December-2020]. [Online].
Available at: https://www.madgetech.com/wp-content/uploads/2020/04/rtdtempx-series-ss-1.pdf

[136] Pv system monitoring with fronius solar.web. . [Accessed: 22-December-2020]. [Online].
Available at: https://www.fronius.com/en/solar-energy/installers-partners/products-solutions/monitoring-digital-tools/pv-system-monitoring-solarweb

[137] Dierauf, T., Growitz, A., Kurtz, S., Cruz, J.L.B., Riley, E. and Hansen, C.: Weather-corrected performance ratio. Tech. Rep., National Renewable Energy Lab.(NREL), Golden, CO (United States), 2013.

[138] Reich, N.H., Mueller, B., Armbruster, A., Van Sark, W.G., Kiefer, K. and Reise, C.: Performance ratio revisited: is pr> 90% realistic? *Progress in Photovoltaics: Research and Applications*, vol. 20, no. 6, pp. 717–726, Wiley Online Library, 2012.

[139] Byd p6-30 series. [Accessed: 22-December-2020]. [Online].
Available at: https://www.zonnepanelen.net/nl/pdf/panels/BYD_220-250P.pdf

[140] Sunny central 800cp xt / 850cp xt / 900cp xt. [Accessed: 22-December-2020]. [Online].
Available at: http://files.sma.de/dl/18859/SC800CP-900CP-DEN1751-V23web.pdf

[141] Google maps. [Accessed: 21-December-2020]. [Online].
Available at: https://www.google.com/maps/@-30.1581358,24.1283488,2711m/data=!3m1!1e3

[142] Protocol description. [Accessed: 22-December-2020]. [Online].
Available at: https://www.modbustools.com/modbus.html

[143] Dyamond, W.P.: Fault detection and performance visualisation for a grid-connected photovoltaic power plant using sensor data. Dec Stellenbosch University, 2019. [Accessed: 22-December-2020]. [Online].
Available at: https://scholar.sun.ac.za/handle/10019.1/107181

[144] AG, S.: Sunny string-monitor. [Accessed: 22-December-2020]. [Online]. Available at: `https://www.sma-mea.com/deleted/products/monitoring-control/sunny-string-monitor.html`

[145] Masuko, K., Shigematsu, M., Hashiguchi, T., Fujishima, D., Kai, M., Yoshimura, N., Yamaguchi, T., Ichihashi, Y., Mishima, T., Matsubara, N. *et al.*: Achievement of more than 25% conversion efficiency with crystalline silicon heterojunction solar cell. *IEEE Journal of Photovoltaics*, vol. 4, no. 6, pp. 1433–1435, IEEE, 2014.

[146] King, R., Bhusari, D., Larrabee, D., Liu, X.-Q., Rehder, E., Edmondson, K., Cotal, H., Jones, R., Ermer, J., Fetzer, C. *et al.*: Solar cell generations over 40% efficiency. *Progress in Photovoltaics: Research and Applications*, vol. 20, no. 6, pp. 801–815, Wiley Online Library, 2012.

[147] Radziemska, E.: The effect of temperature on the power drop in crystalline silicon solar cells. *Renewable energy*, vol. 28, no. 1, pp. 1–12, Elsevier, 2003.

[148] Ã-zisik, M.N., Özışık, M.N. and Özısık, M.N.: *Heat conduction*. John Wiley & Sons, 1993.

[149] Jiji, L.M. and Jiji, L.M.: *Heat convection*. Springer, 2006.

[150] Planck, M.: *The theory of heat radiation*. Courier Corporation, 2013.

[151] pvlib.clearsky.detect_clearsky. . [Accessed: 22-December-2020]. [Online]. Available at: `https://pvlib-python.readthedocs.io/en/stable/generated/pvlib.clearsky.detect_clearsky.html`

[152] Reno, M.J. and Hansen, C.W.: Identification of periods of clear sky irradiance in time series of ghi measurements. *Renewable Energy*, vol. 90, pp. 520–531, Elsevier, 2016.

[153] Koehl, M., Heck, M., Wiesmeier, S. and Wirth, J.: Modeling of the nominal operating cell temperature based on outdoor weathering. *Solar Energy Materials and Solar Cells*, vol. 95, no. 7, pp. 1638–1646, Elsevier, 2011.

[154] Dhouib, A. and Filali, S.: Operating temperatures of photovoltaic panels. In: *Energy and the Environment*, pp. 494–498. Elsevier, 1990.

[155] Li, B., Duell, M., Schuhmacher, T. and Doble, D.M.: Prediction of pv module nominal operating cell temperature using electromagnetic wave modeling. In: *2010 35th IEEE Photovoltaic Specialists Conference*, pp. 002773–002778. IEEE, 2010.

[156] Kratochvil, J.A., Boyson, W.E. and King, D.L.: Photovoltaic array performance model. Tech. Rep., Sandia National Laboratories, 2004.

[157] A full package for the study of your photovoltaic systems. [Accessed: 22-December-2020]. [Online].
Available at: `https://www.pvsyst.com/`

[158] Mow, B.: Stat faqs part 1: Floating solar. April 2018. [Accessed: 22-December-2020]. [Online].
Available at: `https://www.nrel.gov/state-local-tribal/blog/posts/stat-faqs-part1-floating-solar.html`

[159] How is defined the plane orientation ? Aug 2012. [Accessed: 22-December-2020]. [Online].
Available at: `https://forum.pvsyst.com/viewtopic.php?t=168`